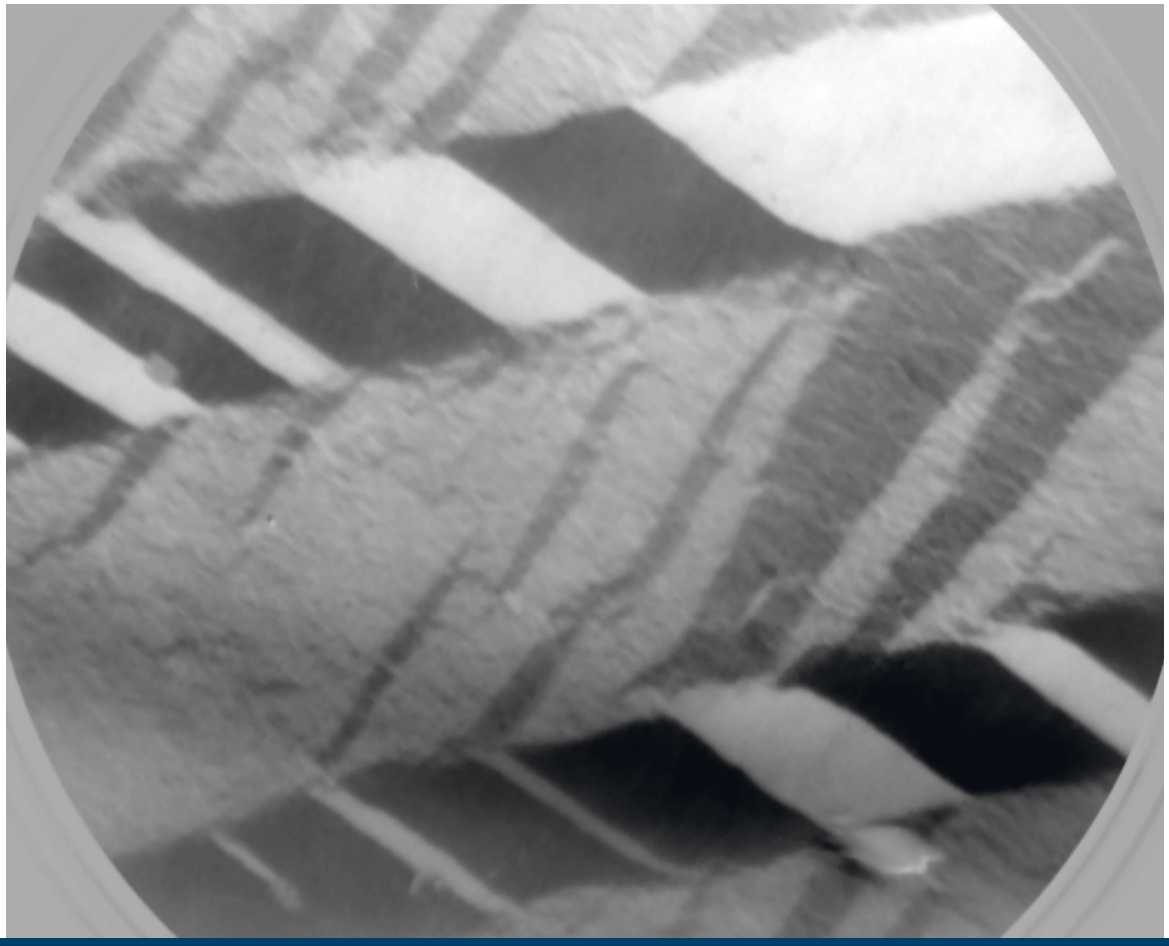

Magnetoelectric Interactions in Multiferroic Thin-film Heterosystems and Nanostructures

Hatice Gökdemir

Schlüsseltechnologien / Key Technologies
Band / Volume 256
ISBN 978-3-95806-635-9

Mitglied der Helmholtz-Gemeinschaft

JÜLICH
Forschungszentrum

Schriften des Forschungszentrums Jülich
Reihe Schlüsseltechnologien / Key Technologies Band / Volume 256

Forschungszentrum Jülich GmbH
Peter Grünberg Institut (PGI)
Elektronische Eigenschaften (PGI-6)

Magnetoelectric Interactions in Multiferroic Thin-film Heterosystems and Nanostructures

Hatice Gökdemir

Schriften des Forschungszentrums Jülich
Reihe Schlüsseltechnologien / Key Technologies Band / Volume 256

ISSN 1866-1807 ISBN 978-3-95806-635-9

Bibliografische Information der Deutschen Nationalbibliothek.
Die Deutsche Nationalbibliothek verzeichnet diese Publikation in der
Deutschen Nationalbibliografie; detaillierte Bibliografische Daten
sind im Internet über http://dnb.d-nb.de abrufbar.

Herausgeber und Vertrieb:	Forschungszentrum Jülich GmbH Zentralbibliothek, Verlag 52425 Jülich Tel.: +49 2461 61-5368 Fax: +49 2461 61-6103 zb-publikation@fz-juelich.de www.fz-juelich.de/zb
Umschlaggestaltung:	Grafische Medien, Forschungszentrum Jülich GmbH
Druck:	Grafische Medien, Forschungszentrum Jülich GmbH
Copyright:	Forschungszentrum Jülich 2022

Schriften des Forschungszentrums Jülich
Reihe Schlüsseltechnologien / Key Technologies, Band / Volume 256

D 464 (Diss. Duisburg, Univ., 2021)

ISSN 1866-1807
ISBN 978-3-95806-635-9

Vollständig frei verfügbar über das Publikationsportal des Forschungszentrums Jülich (JuSER)
unter www.fz-juelich.de/zb/openaccess.

Abstract

Electric-write magnetic-read memory-based devices replace conventional hard-disk drives, since they offer an advantage of reduced power consumption for writing. The next generation spintronic application building blocks are multiferroic materials, which combine and couple magnetic and electric properties. It was therefore of great importance to investigate the still unexplored phenomena, such as electronic structure changes at the interfaces of these heterosystems. Within the scope of this thesis, we have attempted to develop artificial multiferroic (AM) materials with desired ferroic properties. We studied two model systems:

- (i) $BaTiO_3/La_{0.7}Sr_{0.3}MnO_3/SrTiO_3$ (BTO/LSMO/STO) and
- (ii) $Fe/BaTiO_3$ (Fe/BTO).

Firstly, epitaxially grown BTO and LSMO films on STO grown by the pulsed laser deposition (PLD) technique were investigated. Magnetic properties, surface morphologies, and crystal phases of the as-received samples were characterized. To study charge anisotropy and coupling of two ferroic orders of the AM heterostructures element specifically we performed X-ray absorption spectroscopy (XAS) measurements with polarized X-rays at $UE56/1-SGM$ FZ Jülich Beamline at BESSY-II synchrotron facility. Secondly, the Fe/BTO system is investigated using a cutting-edge spectromicroscopic tool, namely the low energy electron microscope/X-ray photoelectron emission microscope (LEEM/XPEEM) located at the same endstation at BESSY-II. LEEM, Auger electron spectroscopy (AES) and low energy electron diffraction (LEED) were used to study the ferroelectric domains, cleanness and termination of the BTO(001) surface, respectively. Spatially resolved electronic structure of ferroelectric domains were demonstrated for the first time using X-ray linear dichroism (XLD)-PEEM contrast mechanism. $In-situ$ and $ex-situ$ Fe growth by e-beam evaporation on BTO(001) was established. To present the interplay between ferroelectricity and inverse magnetostrictive behavior in Fe/BTO, X-ray magnetic circular dichroism (XMCD)- and XLD-PEEM experiments were conducted.

Zusammenfassung

Geräte mit magnetischem Lesespeicher und elektrischem Schreibvorgang ersetzen herkömmliche Festplattenlaufwerke, da sie den Vorteil eines geringeren Stromverbrauchs beim Schreiben bieten. Die spintronischen Anwendungsbausteine der nächsten Generation sind multiferroische Materialien, die magnetische und elektrische Eigenschaften kombinieren und koppeln. Es war daher von großer Bedeutung, die noch unerforschten Phänomene wie elektronische Strukturänderungen an den Grenzflächen dieser Heterosysteme zu untersuchen. Im Rahmen dieser Arbeit wurde versucht, künstliche multiferroische (AM) Materialien mit gewünschten ferroischen Eigenschaften zu entwickeln. Wir haben zwei Modellsysteme untersucht:

- (*i*) $BaTiO_3/La_{0.7}Sr_{0.3}MnO_3/SrTiO_3$ (BTO/LSMO/STO) und
- (*ii*) $Fe/BaTiO_3$ (Fe/BTO).

Zunächst wurden mittels pulsed laser deposition (PLD)-Technik epitaktisch gewachsene BTO and LSMO Filme auf STO untersucht. Die magnetischen Eigenschaften, Oberflächenmorphologien und Kristallphasen der erhaltenen Proben wurden charakterisiert. Um die Ladungsanisotropie und die Kopplung zweier ferroischer Ordnungen des AM Heterostrukturelements speziell zu untersuchen, wurden Röntgenabsorptionsspektroskopiemessungen (XAS) durchgeführt mit polarisierten Röntgenstrahlen bei UE56/1− SGM FZ Jülich Beamline bei BESSY-II Synchrotronanlage.
Zweitens wird das Fe/BTO System unter Verwendung eines hochmodernen spektromikroskopischen Instruments untersucht, nämlich eines low energy electron microscope/X-ray photoelectron emission microscope (LEEM/X-PEEM)-Mikroskops, das an derselben Endstation bei BESSY-II durchgeführt wurde. Der LEEM, AES und LEED wurden verwendet, um die ferroelektrischen Domänen, die Reinheit und den Abschluss der BTO(001) Oberfläche zu untersuchen. Die räumlich aufgelöste elektronische Struktur ferroelektrischer Domänen wurde erstmals mithilfe des X-ray linear dichroism (XLD)-PEEM-Kontrastmechanismus demonstriert. Zuletzt wurde das Wachstum von Fe durch Elektronenstrahlverdampfung $in-situ$ und $ex-situ$ auf BTO(001) ermittelt. X-ray magnetic circular dichroism (XMCD)- und XLD-PEEM Experimenten wurden durchgeführt, um das Zusammenspiel zwischen der Ferroelektrizität und dem inversen magnetostriktiven Verhalten in Fe/BTO darzustellen.

Erklärung

Hiermit erkläre ich, dass ich die vorliegende Arbeit selbstständig und ohne Fremde Hilfe verfasst habe. Ferner habe ich außer den angegebenen Quellen keine anderen Quellen und Hilfsmittel benutzt. Die dem Sinn oder Wortlaut nach entnommenen Textpassagen oder Abbildungen habe ich in jedem Einzelfall kenntlich gemacht.
Dieser Dissertation geht weder ein erfolgloser Promotionsversuch voraus, noch wurde sie in einem weiteren Promotionsverfahren eingereicht. Abgesehen von den angegebenen Publikationen sind die Ergebnisse dieser Dissertation unveröffentlicht. Diese Dissertation, die den Doktorgrad "Dr.rer.nat." anstrebt, wurde von Prof. Dr. Claus M. Schneider betreut.

Istanbul, den 7. Mai 2021,

Hatice Gökdemir

Acknowledgements

An dieser Stelle möchte ich all jenen danken, die mich bei der Anfertigung dieser Dissertation unterstütz und inspiriert haben.
Mein erster Dank geht an Herrn **Prof. Dr. Claus M. Schneider**, der es mir ermöglicht hat meine Doktorarbeit in seiner hervorragend ausgestatteten Arbeitsgruppe anzufertigen. Ich bin Ihnen sehr dankbar dafür, dass Sie an mich geglaubt und mich unterstütz haben. Es war ein Privileg, unter Ihrer Aufsicht promovieren zu dürfen. Vielen herzlichen Dank für alles Herr Prof. Schneider.

Mein Dank gilt ebenso **Prof. Dr. Carolin Schmitz-Antoniak** für Ihr Zweitgutachten, die wissenschaftliche Gespräche und das Korrekturlesen einige Teile dieser Arbeit.

Auch danke ich die Kommissionsmitglieder **Prof. Dr. Rossitza Pentcheva** und **Prof. Dr. Heiko Wende**.

Ich möchte mich bei **Dr. Ingo Krug** für die interessante Themenstellung und Ihre Betreuung bedanken. Danke schön, dass ich von Dir vieles lernen durfte.

Dr. Stefan Cramm, es fällt mir schwer, Worte zu finden, um dir zu danken. Vielen Dank für die wissenschaftliche und nichtwissenschaftliche Diskussionen, Unterstützung und Anleitung bezüglich der Beamline. Du warst immer da, wann ich ein Problem hatte. Danke für die Gespräche über die griechische Mythologie und die Herkunft der Elementnamen. Ich habe die Tantalmünze immer noch in meiner Brieftasche :)

Bedanken möchte ich mich bei **Dr. Slavomir Nemsak** dafür, dass er einen Teil dieser Arbeit korrekturgelesen hat, seine Hilfe bei der Auswertung der XPS Daten und für die netten Gespräche. Slavo, ohne Deine Hilfe wäre es nicht möglich gewesen diese Arbeit anzufertigen.

Ich bedanke mich herzlich an Herrn **Dr. Jürgen Schubert** für unsere Zusammenarbeit und die beste Qualitat von BTO/LSMO Proben.

Für das tolle Arbeitsklima möchte ich mich bei **allen Kolleginnen und Kollegen des PGI-6** bedanken.

Insbesondere möchte ich mich bei **Dr. Florian Nickel**, **Dr. Daniel M. Gottlob**, **Dr. Johanna Hackl**, und **Dr. M. Imtiaz Khan** bedanken. Die tolle Messzeiten und unsere nette atmosphere bei BESSY werde ich nie vergessen.

Jürgen Lauer, **Heinz Pfeiffer**, **Thomas Jansen** und **Bernd Küpper** bin ich sehr dankbar für ihren technischen Support.

Dem ganzen BESSY Team möchte ich danken für permanenten Support.

Ein ganz besonderer Dank geht an **Prof. Dr. Fikret Yildiz** für Korrekturlesen dieser Arbeit und unsere Diskussionen generell über Magnetismus.

Ich bedanke mich bei **Dr. Ahmet Akin Ünal** und **Dr. Bünyamin Ümsür** für die XPS Messungen und die nette Gespräche bei unseren Kaffeepausen.

Besonderer Dank gebührt **Christina Pietsch** und **Meltem Özcan**. Ich werde mich immer an unsere Museumsbesuche, Berlin Touren und die Kochabenteuern erinnern.

Ich danke **Dr. Muhsin Mazman** und **Talip Yildiz** für die Ermutigung bezüglich des Promovierens.

Mein ganz besonderer Dank geht an meine Eltern, **Kadriye** und **Şahin Doğanay**, meinen Bruder **Serdar Doğanay** und **Hilal Teltik Doğanay** für ihre moralische Unterstützung und ihre unersetzbare Liebe.

Zu guter Letzt möchte ich mich herzlich bei meinem Mann **Salih Gökdemir** und unserer Tochter **Derya** bedanken. Meine liebe Derya, deine Mutter konnte endlich ihre Promotion erfolgreich abschließen :)

Contents

Chapter 1

Introduction

Nanotechnology is one of the rapidly growing subdivisions of materials science [1]. It aims at developing novel and improved technologies for information storage and processing through manipulation of spin, charge and strain states in solid state systems. The way to progress in new technologies depends not only on the production of new materials and the understanding of their physical properties, but also on the search for the undiscovered electronic, chemical and structural properties in the existing materials [2]. In the last years, technological devices constituting of layered material systems with enhanced functionalities drew a lot of attention. Materials combining at least two different ferroic degrees of freedom at the same time are called multiferroics [3]. Unique combinations of the large ferroic order parameters, high Curie temperatures and strong coupling between the two different orders make "$artificial$" multiferroics (AM) interesting materials for applications like, e. g. multiple-state memories in spintronics [4]. Advanced deposition techniques such as pulsed laser deposition (PLD) and molecular beam epitaxy (MBE) allow to engineer artificial materials based on complex oxides and metals. Surface and interface properties of such individual layers in multilayered systems and chemical, electronic and magnetic interactions occurring in between two adjacent layers rule the performance of the magnetoelectric device.
One popular approach providing an intrinsic control of magnetism is to elastically couple magnetic thin films to suitable ferroelectric single crystals. Strain transfer from the ferroelectric material influences the magnetic thin film properties via the magnetoelastic effect. There are various probes for nanoscale investigations which are good at studying either spatial or chemical properties [1]. Sophisticated techniques such as spatially-resolved spectroscopic measurements with "sub 50 nm" resolution are required to resolve typical ferroic domains [1]. High spatial resolution combined with element selectivity makes soft x-ray based spectroscopic microscopy increasingly the main tool for nanoscale studies [5]. One of the most popular instruments of such a type is a Photoelectron Emission Microscope (PEEM). In this work, the SPECS FE

LEEM P90 AC at the Forschungszentrum Jülich (FZJ) synchrotron radiation beamline at BESSY-II was utilized. This instrument combines the structural sensitivity of Low Energy Electron Microscopy (LEEM) with the flexible spectroscopy of energy-filtered PEEM. In combination with tunable soft x-rays, it provides elemental, chemical, structural and magnetic contrast.

The scope of the present work covers the investigation of interactions across ferroelectric-ferromagnetic interfaces of $BaTiO_3/La_{0.7}Sr_{0.3}MnO_3$ and of $Fe/BaTiO_3$ artificial multiferroics. As a model system for the magnetic material, $La_{0.7}Sr_{0.3}MnO_3$ (LSMO) provides a large area for promoting the coupling of several degrees of freedom in a single-phase oxide film. It possesses strongly correlated magnetic and electronic transport properties. At a certain temperature manganites undergo a metal-to-insulator transition (MIT) and a ferromagnetic (FM) to paramagnetic (PM) transition [6]. At the Curie temperature a sharp transition in the resistivity from the metallic ferromagnetic phase into the insulating paramagnetic phase is expected to occur for a homogenous sample. However, measurements show a rather broad transition, and the collosal magneto resistance (CMR) does not saturate at high magnetic fields. This is explained in terms of intrinsic inhomogeneities, which cause the formation of insulating and conducting domains within a single sample [6]. At low temperatures the control mechanism is the metallic double-exchange phase. With increasing temperature electrically insulating regions develop leading to an electronic phase separation in a chemically homogeneous sample. This intrinsic behavior can be modified by external parameters like pressure, external magnetic field or doping. Besides, mixed valence LSMO is sensitive to lattice distortions and orbital ordering usable for "strain engineering", which in turn affect its magnetic and electronic properties [7, 8, 9, 10].

LSMO films grown on $SrTiO_3$ show different magnetic properties due to the lattice mismatch between the film and the substrate and oxygen non-stoichiometry in the lattice arising from improper growth conditions [11]. The unit cell is mostly stressed, and these strained lattice structures deform the MnO_6 octahedra and so the ferromagnetic interaction and electric conductivity is suppressed [11] compared to bulk LSMO. Different film growth parameters, such as substrate temperature and oxygen pressure during growth, and the effect of capping also play an important role on the physical properties of LSMO films.

Equally important to LSMO, widely used materials in applications ranging from energy harvesting to high-power electronic transducers are ferroelectric materials [12]. Standard industry ferroelectric materials like $PbZr_xTi_{(1-x)}O_3$ contain lead. The major drawback of these materials is that they are toxic and enviromentally unfriendly [13]. One of the alternative ferroelectrics is $BaTiO_3$ (BTO), which is non-toxic and has excellent tunable ferroelectric properties, for instance, the phase transition temperature [13, 14]. Great effort has been devoted to the bulk BTO single crystal studies [15].

BTO has many advantages such as low leakage current, low dielectric loss and high dielectric constant [16]. Epitaxial thin BTO films of $3-30$ nm have been prepared on different single-crystal oxide substrates by PLD, demonstrating notable structural perfection comparable to that of BTO single crystals [15, 17, 18]. On the other hand, for micro- and nanoelectronics, much thinner films are more relevant. Thermodynamically stable ferroelectric ultra-thin film properties at $3-30$ nm thickness [18] may deviate from the bulk due to the strain and stress arising from the interfaces [15]. As we found, of outmost importance is the modification of the ferroelectric response due to the interface boundary conditions and the film thickness size effect.
In the last few years a growing interest has been given to the study of the combined functionality of ferroelectrics and ferromagnets. The interesting electronic properties of such AM interfaces are underlined, for example, by a publication of Burton *et al.* who predicted a magnetoelectric interaction at the interface between BTO and a contacting $La-A-MnO_3$ (LAMO) layer (where -A- is a divalent cation [19]). By the effect of the ferroelectric polarization accumulating or depleting charge at the BTO/LAMO interface, the interfacial magnetic state in the LAMO undergoes a strong change from a ferromagnet to an A-type antiferromagnet, though this change has not been observed directly, yet [20].
Studies showed a number of interesting phenomena occuring in Fe/BTO heterosystems. First principles calculations predicted a change in magnetic order in Fe films on TiO_2-terminated BTO(001) or $PbTiO_3$(001) surfaces as a function of Fe thickness [21]. Fe/BTO hybrids are very interesting to study, because:

- Bulk properties of BTO single crystals and Fe are very well-known.
- Strong magnetoelectric coupling between the ferroic order parameters for the (Fe/BTO) interface is predicted[22].
- Lattice mismatch between the BTO and the Fe is about 1.5 %.
- Fabricated devices can be operable at room temperature.

For the Fe/BTO heterosystems, sizable changes of the interfacial Fe magnetic moment upon reversal of the dielectric polarization of BTO due to interface cation displacements were predicted both for abrupt and oxidized Fe/BTO interfaces [22, 23] and immediately afterwards ferrolectric control of magnetism was demonstrated [24]. Given these points, the electric-field driven magnetization reversal would be desirable for spintronic applications due to reduced energy dissipation [25]. Recently, it has been shown that magnetic domain patterns with alternating uniaxial and biaxial anisotropy can be imprinted on Fe films grown on BTO(001) [25].
Another very important issue in the magnetic properties of thin films is the stability

of the interface. There are several studies with partly contradictory results about the Fe/X interface with X being MgO, NiO, Al_2O_3, BTO etc.:

- The presence of an oxidic layer up to 2 ML in an Fe/NiO system [26].
- A weak chemical interaction at the Fe/MgO interface [27].
- An Fe^{2+} state on Al_2O_3 [28].
- Presence of an oxidized Fe at the interface to the $BaTiO_3$ up to 2 nm verified by XPS measurements [29].
- Absence of Fe oxidation at the Fe/BTO interface proved by Hard X-ray Photoemission Spectroscopy (HAXPES)[21].

Thus, further studies are needed to resolve the origin of these findings.
This thesis aims at investigating the largely unexplored phenomena such as electronic structure changes at the interface between a ferroelectric and a ferromagnet. It is structured as follows: First, an introduction to ferromagnetic thin films of LSMO and of Fe is given with a focus on the magnetic domain and magnetic domain wall formation energies in transition metals. Later, basic ferroelectric properties and the interactions across ferroelectric-ferromagnetic interfaces are outlined. In Chapter 3 the experimental tools and techniques involved in fabricating samples and measuring their magnetic, surface and x-ray based electronic properties are described. At the end of Chapter 3 an overview of the LEEM/PEEM instrument at FZJ Beamline is introduced. Chapter 4 and Chapter 5 summarize the main results of this thesis: To gain a detailed picture of the electronic, structural, morphological and magnetic information of the all-oxide hybrids, a special emphasis is put on the investigation of such physical properties in BTO/LSMO/STO heterosystems depending on the preparation conditions. Results are presented in Chapter 4. In Chapter 5, a combined LEEM/PEEM study firstly on BTO single crystals and secondly on the Fe/BTO system is presented. In the last section of this chapter, studies on the growth of Fe ultrathin films on BTO and the investigations of the interface stability and the magnetic properties upon Fe deposition conditions are shown. Finally, in Chapter 6, a brief summary and an outlook of this thesis is given.

Chapter 2

Theoretical Background

This chapter presents the theoretical background for understanding and interpreting the results described in this thesis. Section 2. 1 introduces basic properties of ferromagnets. Sections 2. 2 and 2. 3 cover the magnetic properties of LSMO and Fe, respectively. In section 2. 4 the concept of ferroelectricity is presented. In this section, specifically ferroelectric properties of BTO single crystals are outlined. In section 2. 5 some important aspects of spintronics, which are relevant when combining ferroelectric materials with ferromagnets in all-oxide and in metal/oxide hybrids are presented. The last section of this chapter reviews X-ray Absorption Spectroscopy (XAS) and two other well established techniques, namely X-ray Magnetic Circular Dichroism (XMCD) and X-ray Linear Dichroism (XLD), for characterization of the magnetic and structural properties of surfaces and buried layers in an element specific way, respectively.

2.1 Basic Properties of Ferromagnets

The characteristic feature of a ferromagnetic material is the spontaneous magnetization caused by the alignment of atomic magnetic moments. In ferromagnetic materials, the magnetic moment of the atoms originates from the electron's spin, and their orbital angular momentum around the nucleus.
Exchange interaction lies at the center of ferromagnetism, which is responsible for the parallel alignment of neighboring spins [30]. The origin of this interaction is related to Pauli exclusion principle and Coulomb repulsion.
The exchange mechanism can be described by a Heisenberg-Spin-Hamiltonian:

$$H_{spin} = \sum_{i,j} J_{i,j} S_i . S_j, \tag{2.1}$$

with S_i and S_j being classical spin vectors. The pair interaction $J_{i,j}$ sets the strength of the interaction between two spins in the system. For $J_{i,j}<0$ ferromagnetic alignment

is favored and for $J_{i,j}$>0 antiferromagnetic order.
The ferromagnetism of 3d transition metals Fe, Co and Ni is based on the delocalized electrons, in which the magnetization is due to spontaneously spin-split bands. The model to describe the band ferromagnetism is the Stoner model and is described briefly in the following paragraphs.

The Stoner Model of 3d Ferromagnetism

As shown in Figure 2. 1, placing a small number of spin down electrons from the minority band at the Fermi level into the spin up band (majority band) is associated with an energy increase of δE [31]. The number of moved electrons is g(E_F)δE/2 and the total kinetic energy change ΔE_{kin}, is [31]:

$$\Delta E_{kin} = \frac{1}{2} g(E_F)(\delta E)^2, \tag{2.2}$$

with $g(E_F)$ being the density of states at the Fermi level. Considering the Eqn. 2. 2, the system is in an unfavored state, however, the interaction of the magnetization with the molecular field leads to an energy reduction that can compensate this cost [31].

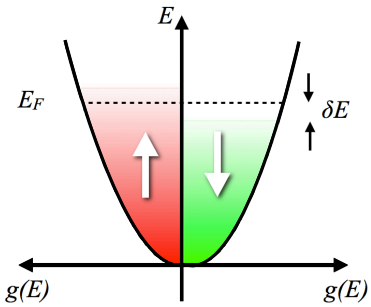

Figure 2.1: Schematic representation of density of states showing spontaneous splitting of energy bands (figure is reproduced from [31])

.

The change of potential energy is represented by the reduction of the wavefunction overlap between the ions. By increasing the mean distance between the electrons of parallel spin, the Coulomb energy is reduced.
A material is ferromagnetic, if the condition given by the Eqn. 2. 3 is fullfilled:

$$U_n(E_F) = I \cdot g(E_F) \geq 1, \tag{2.3}$$

with U_n being the Stoner factor [32]. Here I denotes the exchange integral. If a material possesses relatively strong Coulomb interactions and electrons in higher energy states, a large density of states develops at the Fermi level. Such systems are the best ferromagnetic candidates.
While these are valid for Transition-Metal Oxides (TMOs) as well, additional phenomena such as p-orbital magnetism, double-exchange, and superexchange mechanisms must be involved for TMOs, which are explained in Section 2. 2.

2.1.1 Energy Contributions in Ferromagnetic Systems

In micromagnetism, the magnetization, *i. e.* the density of magnetic moments, is expressed by a continuous vector field $M(x)$. Micromagnetism and domain wall theory are based on the principles, which state that the $M(x)$ direction is preferred to minimize the free energy of the system [30]. In this section, an overview of the influence of different energy contributions in ferromagnetic systems on magnetic domain formation will be provided.

Exchange Energy

The direct exchange interaction is responsible for the parallel alignment of neighboring spins, which results from the Pauli exclusion principle [30]. In micromagnetism, the exchange interaction is derived from the Heisenberg Hamiltonian, in which the spin operators are replaced by the classical vectors. Any deviation from the parallel alignment causes extra energy, which can be described as

$$E_{exc} = A \int_V (\nabla\ m_x)^2 + (\nabla\ m_y)^2 + (\nabla\ m_y)^2 dV, \tag{2.4}$$

where A is a material constant, the so-called exchange stiffness constant with the dimensions (J/m) and $m = M/M_S$ is the reduced magnetization, with M_S being the saturation magnetization. [30].

Anisotropy Energy

Depending on the magnetic material there are preferential directions of magnetizations, where different strength of magnetic fields are needed to saturate the magnetization [33]. These directions are called $easy-$ and $hard-axis$. The occurence of the axis relies upon the magnetic anisotropies. The energy required to change the magnetization of a material from the easy-axis to the hard-axis is defined as magnetic anisotropy energy [34]. During magnetization reversal the energy of the system must be conserved.

$$E_{ani} = K_1 sin^2\theta + K_2 sin^4\theta + ... \tag{2.5}$$

Here, K_1 and K_2 describe the specific anisotropy constants with the dimension J/m^3 and θ the angle between the magnetization and the easy-axis.
The anisotropy of $3d$ transition metals consists of two particular contributions, which have different microscopic origins:

- *Magnetocrystalline anisotropy*: related to spin-orbit coupling. The difference of the orbital angular moments along easy- and hard-axis is proportional to the magnetocrystalline energy.

- *Form anisotropy*: related to magnetostatic fields. It is defined as the tendency of the magnetization to align parallel in the plane of thin film to avoid the surface charge formation.

In case of thin films, magnetocystalline anisotropy favors an out-of-plane, and form (shape) anisotropy favors an in-plane magnetization.

Zeeman Energy

Zeeman energy contribution depends on the relative orientation of the external magnetic field

$$E_{Zeeman} = \int_V \mu_0 H_{ext} \cdot M dV. \tag{2.6}$$

Here, μ_0 is the magnetic constant, e. g. vacuum permeability, and is $\mu_0 = 4\pi$ x 10^{-7} $\frac{\mathrm{Vs}}{\mathrm{Am}}$.
If M and H_{ext} have same orientation, the E_{Zeeman} energy contribution can be neglected.

Magnetostatic Energy

The term "*stray field*" is ascribed to magnetostatic field outside the ferromagnet, while the "*demagnetizing field*" is referred to the field inside the sample, which opposes the direction of the magnetization [35]. Volume and surface charges are accepted as the sources of demagnetizing field. With this in mind, total magnetostatic energy can be written:

$$E_{dem} = \mu_0 \int_{all\ space} {H_{dem}}^2 dV, \tag{2.7}$$

where H_{dem} is the internal demagnetizing field and the factor $\frac{1}{2}$ excludes self-interactions. According to Eqn. 2. 7, magnetostatic energy E_{dem}, is always positive and can only be minimized by avoiding the formation of magnetic charges [35].

2.1.2 Formation of Magnetic Domains and Domain Walls

Domains in ferromagnetic materials are established in order to reduce the total magnetic energy E_{tot}, given by the Eqn. 2. 8:

$$E_{tot} = E_{exc} + E_{ani} + E_{Zeeman} + E_{dem}. \tag{2.8}$$

In Eqn. 2. 8, exchange E_{exc}, anisotropy E_{ani}, Zeeman E_Z energy terms are related to bulk material properties. However, demagnetization E_{dem} is associated with shape anisotropy. In addition to the intrinsic material properties it acts through the demagnetization of the shape (thin film) and changes the total energy of the system.
Areas of uniform magnetization divided by magnetic domain walls are called magnetic domains. The dimensions of magnetic domains are determined by the minimization of E_{tot}. An important definition in this regard is called exchange length, l_{ex}, which indicates the distance below which inter-atomic exchange interactions dominate and can be written as:

$$l_{ex} = \sqrt{\frac{A}{\mu_0 {M_S}^2}}. \tag{2.9}$$

It is an intrinsic and material specific length scale, which provides an estimate for the typical size of magnetic inhomogeneities. The magnetic domain formation in an isotropic magnetic system in remanence is depicted in Fig. 2. 2. The stray field of a homogenously magnetized sample is notably high. It can be minimized by domain formation, but in this case, the exchange energy will increase. However, in a ferromagnet an abrupt reversal of magnetization direction between two spins is unfavored: Spins rotate gradually over an interfacial area, i. e. a domain wall.
Magnetic domain formation is favorable when the size of a magnetic structure becomes larger than l_{ex}. Fig. 2. 2 (a) shows the magnetic domain configuration in an isotropic magnetic system in remanence. The magnetic moments align themselves parallel to the sample edges in order to minimize the magnetostatic energy. In the presence of a uniaxial anisotropy most of the magnetic moments will order themselves parallel to each other along the uniaxial easy-axis. As presented in Fig. 2. 2 (b) closure domains form with the magnetic moment perpendicular to the magnetic easy axis to avoid magnetostatic energy increase.
Closure domain formation is compensated by the stray field reduction. The competition between the exchange and the magnetic anisotropy energies sets the domain wall width.
If the exchange stiffness is large, it widens the domain walls via small angle rotation of neighboring spins. On the contrary, the domain wall width shrinks if the magnetic anisotropy becomes larger, because the additional energy due to the spins pointing away from the magnetic easy-axis inside the domain wall must be compensated [37].

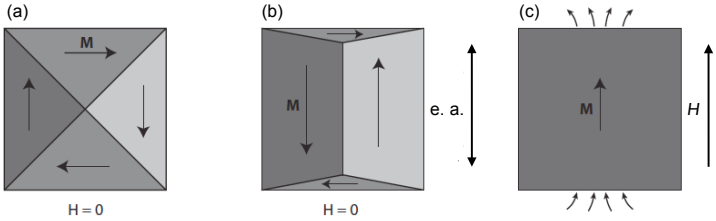

Figure 2.2: Illustrations of different magnetization states. Magnetization direction is indicated by the black arrows. Stray field energy is minimized in an isotropic system by the formation of domains as depicted in (a). Domain formation in an uniaxial anisotropy system is shown in (b) The easy-axis is denoted as e. a. A single-domain consisting of uniform magnetization along an external magnetic field H is shown in (c). Field lines indicate the stray fields generated at the surface [adapted from [36]].

Two types of domain walls can develop in magnetic films: Bloch and Néel walls, as shown simplified in Fig. 2. 3. Depending on the thickness of the sample, a Bloch or a Néel wall occurs. In bulk-like ferromagnetic films the required thickness to rotate the spins out-of-plane to the wall is supported, thus making Bloch walls more favorable. However, in case of thin films Néel walls are more favorable, in which the spins rotate in-plane with respect to the wall. As illustrated in Fig. 2. 3 (b), in the center of the wall the spins point perpendicular to the domain wall generating magnetostatic stray fields between the domains. The emerging magnetostatic energy increases linearly with the film thickness, therefore Néel walls are limited to thin magnetic films.
More details about the specific electronic properties, exchange mechanisms and evolution of ferromagnetism in the systems studied here as well as peculiarities of thin film magnetism are given in the following sections.

2.2 Electronic Structure and Magnetism of $La_{0.7}Sr_{0.3}MnO_3$ Films

In this section, a short review of the electronic properties of the half-metal-ferromagnet $La_{0.7}Sr_{0.3}MnO_3$ (LSMO) is presented.
The complex correlation of spin, charge, orbitals and lattice enables control of the electronic functionality that lies at the heart of the Transition-Metal Oxides (TMO) [39]. TMOs possess strongly correlated electron states and manganites have a complex electronic structure [40, 41, 42]. In TMO, the d-electrons determine the electronic properties. In order to outline the most important interactions in manganites a simple ionic

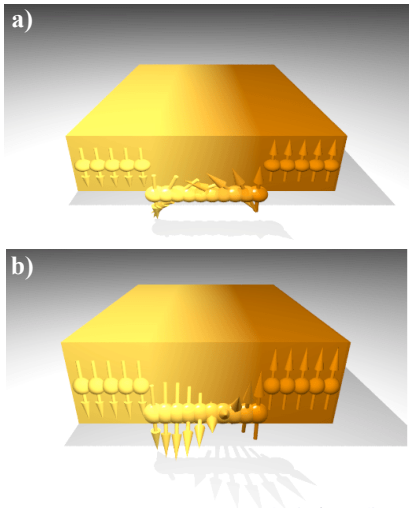

Figure 2.3: Schematic presentation of the magnetization vector rotation in the Néel wall (a) and in the Bloch wall (b) in thin magnetic films [adapted from [38]].

scheme is considered as shown in Fig. 2. 4. In the following the most important contributions to the electronic energy in manganites will be outlined. These are summarized as follows [40]:

- the crystal field splitting energy, Δ_{cf} in octahedral coordination
- kinetic energy of e_g electrons
- the Coulomb interaction among e_g electrons
- the Hund on-site magnetic coupling between e_g and t_{2g} electron spins
- the Heisenberg magnetic coupling between the nearest-neighbour localized electron spins
- coupling of e_g electrons and elastic distortions of MnO_6 octahedra (Jahn-Teller effect)

Depending on the influence of one or the other mechanism various electronic ground states occur. The ground states observed for manganites consist of mainly ferromagnetic metals and antiferromagnetic insulators. There are also some rare ground states

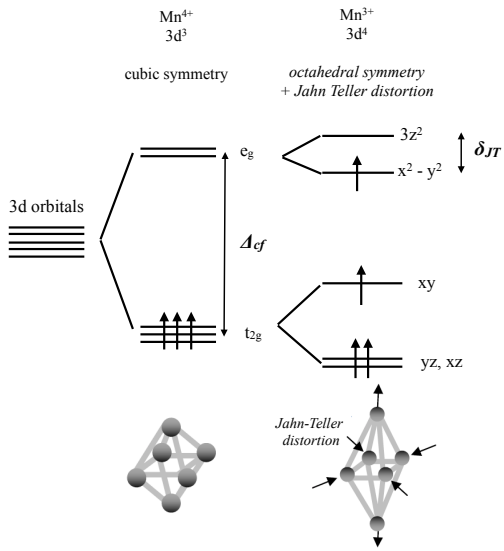

Figure 2.4: Schematics of 3d electronic states in Mn^{3+} and Mn^{4+} ions in perovskite manganites. Abbrevations denote Δ_{cf} octahedral crystal field splitting and δ_{JT} Jahn-Teller splitting energies resulting from the distortion of the oxygen octahedron (as sketched below). The 3d-orbitals in Mn split first into two levels (e_g and t_{2g}) due to the crystal field splitting, and then into four levels ($yz/xz, xy, x^2 - y^2$and $3z^2$) due to the Jahn-Teller distortion. The orbitals are only occupied by one type of spin leading to ferromagnetism [40]. Figure is reproduced from [40].

observed such as ferromagnetic insulators and antiferromagnetic metals. However, approximately all metallic manganites are ferromagnetic, because electron transfer enhances the double-exchange mechanism [40].

LSMO has a distorted perovskite structure, with a pseudo-cubic lattice parameter of a = 3.87 Å[43]. The electronic configuration of $Mn^{3+(4+)}$ is $1s^2 2s^2 2p^6 3s^2 3p^6 4s^2 3d^{4(3)}$. Partially filled 3d levels are not degenerate, but split into a low energy t_{2g} triplet and a high energy e_g doublet due to the crystal field. The t_{2g} orbitals are lower in energy than the e_g orbitals, because the e_g orbitals are pointing towards the oxygen ions, leading to a larger Coulomb repulsion energy than in the other directions [44]. Further splitting within the t_{2g} and e_g levels occurs due to Jahn-Teller effect resulting from the distortion of the oxygen octahedron. The resulting orbital occupancy is shown in Fig. 2. 4. The crystal field splitting is weaker than the Hund's rule coupling energy U_H, which is

about 2 eV for Mn [45]. Thus, three electrons in the 3d orbitals occupy the t_{2g} levels and are localized. The remaining one electron occupies the e_g level and is delocalized [40]. Furthermore, all electrons have parallel spins according to Hund's first rule [40]. The energy levels of the t_{2g} electrons are positioned far from the conduction band. The Fermi level of the material is set by the hybridization of the spin up e_g orbital in Mn and the p orbitals of oxygen. Since LSMO is a half-metal, it has localized spin up ($\uparrow$) carriers and delocalized spin-down ($\downarrow$) carriers or vice-versa. Spin-up electrons have a partially occupied band, while spin-down electrons have filled bands separated from the spin-up electrons by a gap. In an ordinary insulator the band-gap exists for both spin states. In the case of half-metals, however, it is so that one spin state has no gap. Thus, the half-metal LSMO is 100% spin-polarized (in the ideal case)[44, 46].

Magnetic Properties of Doped Manganites

LSMO is ferromagnetic at room temperature for Mn doping levels between 0.3 and 0.4. For other doping levels it is antiferromagnetic [42]. The double-exchange mechanism favors ferromagnetic order. Depending on the orbital filling and the directionality superexchange can lead to both ferro- and antiferromagnetic order [47].

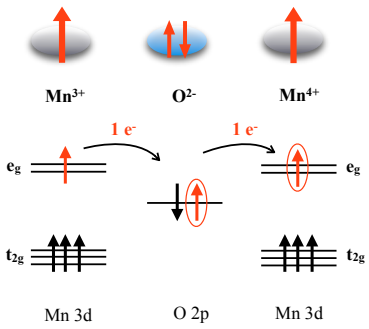

Figure 2.5: Schematic presentation of double exchange mechanism illustrating the hopping of e_g electrons between Mn 3d and O 2p orbitals. Arrows indicate spin-conservative electron transfer between Mn ions, which proceeds via intermediate O 2p orbitals (Figure is reproduced after [48]).

The concept of ferromagnetic double-exchange for manganites was introduced by Zener [49, 50]. LSMO has an average Mn charge between +3 and +4 [40] and the model is based on the coexistence of Mn^{3+} $t_{2g}(3)e_g(1)$ and Mn^{4+} $t_{2g}(3)e_g(0)$ ions. According

to this model two simultaneous electron transfers occur: one electron from Mn^{3+} to a neighboring O 2p orbital and a second electron from this O 2p orbital to an adjacent Mn^{4+} [40]. In Fig. 2. 5, a schematic presentation of double-exchange mechanism illustrating the hopping of e_g electrons between Mn 3d and O 2p orbitals is depicted.
The hopping process minimizes the kinetic and thus the total energy. Mainly, double–exchange means a magnetic interaction mediated by itinerant spin-polarized d electrons, which couple according to Hunds rule to the localized magnetic moments [40, 51, 52, 53].
In addition to the double–exchange mechanism, superexchange interactions between Mn t_{2g} electrons as well as between e_g electrons on neighboring sites might develop [54]. Detailed analyses on the superexchange interactions are given by Goodenough and Kanamori [55, 56]. Depending on the orientation of the Mn^{3+} e_g orbital in (Mn^{3+} e_g) –O–(Mn^{4+} e_g) configuration superexchange can be ferromagnetic or antiferromagnetic. For example, $LaMnO_3$ is an A-type antiferromagnet, which consists of ferromagnetically aligned magnetic moments within the cubic (001) planes and an alternating direction of the moments in adjacent planes [40]. Hence, the orbital degree of freedom is important for manganite physics [8, 57].

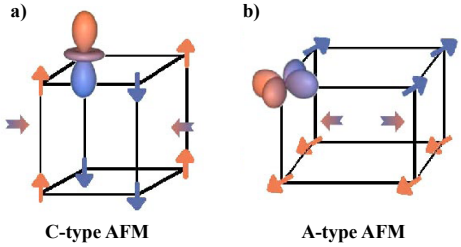

Figure 2.6: Schematic presentation of relation between strain and Mn orbital ordering: a) Compressive strain favors the $3z^2$ orbital and the C-type antiferromagnetic structure and b) tensile strain favors the $x^2 - y^2$ orbital and the A-type AF structure (Adapted from Ref. [8]).

Large electron-lattice interactions, in particular due to the Jahn-Teller effect on Mn^{3+} ions lift the degeneracy of the e_g levels and reduce the electronic energy for the single e_g occupation [58, 59]. Depending on the strain-induced elongation or compression of the MnO_6 octahedra the e_g levels will be split. As shown in Fig. 2. 6, an in-plane compressive strain favors the $3z^2$ orbital and the C-type antiferromagnetic structure and tensile strain favors the $x^2 - y^2$ orbital and the A-type AF structure [8].

2.3 Ferromagnetism of Thin Fe Films

Iron (Fe) has a rich phase diagram. Below T = 1044 K it is in $\alpha - Fe$ phase, which has the body centered cubic (bcc) lattice structure. With increasing temperature the phase first changes to $\gamma - Fe$ (face centered cubic (fcc) lattice structure) and then to $\delta - Fe$ (bcc lattice structure), and finally at T $>$ 1811 K it is melted. In this thesis, we focus on the $\alpha - Fe$ phase, which is the stable phase of Fe at room temperature. The easy-axis of this phase is along the <001> direction.
Fe has a broad, almost unpolarized *sp* band superposed on a spin-split 3*d* band. The unsplit density of states $g(E)$ shows a peak at the Fermi level, so that the Stoner criterion for the spontaneous ferromagnetism is fulfilled [60].

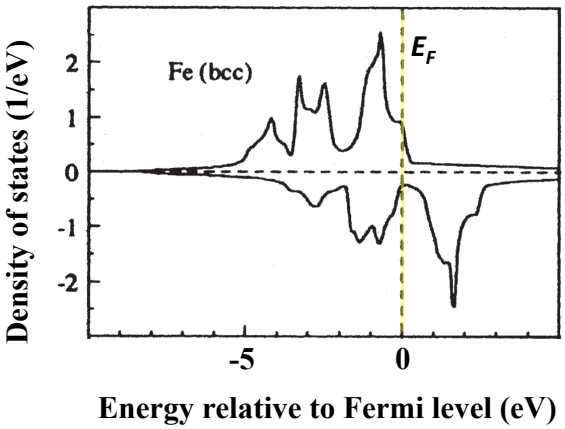

Figure 2.7: Spin-polarized density of states for Fe. The Fermi energy E_F is highlighed with yellow line (Reproduced after Ref. [60]).

The spin-split density of states for Fe is shown in Fig. 2. 7. One can see that the density of state of spin up and spin down electrons are shifted so that there is a finite magnetization. Iron is a weak ferromagnet, because there are both 3*d* spin up and 3*d* spin down electrons at the Fermi level.
The magnetic properties of a thin film are correlated with its dimensions. As mentioned in section 2. 1, the ferromagnetism of 3*d* transition metals is based on the delocalized electrons and the direct exchange interaction is responsible for the parallel alignment of spins [30]. When a thin film is grown on a substrate the lattice parameter of film might change due to the compressive/tensile strain created in the film, which can affect

magnetic properties of the thin films.
In general, magnetization in ferromagnetic materials is determined by the competition between exchange, magnetostatic and anisotropy energies. The exchange energy dominates at small length scales, whereas the magnetostatic and the anisotropy energies control the long-range magnetic ordering [61]. When considering the FM behavior of thin films, the key words are film thickness and symmetry breaking:

- With the breaking of the symmetry, surfaces and interfaces emerge, which will affect the magnetic behavior of the film.
- With increasing film thickness phenomena such as spin reorientation transition occur, which is attributed to the competition between the magnetostatic energy and the energy required for creating domain walls [62].

2.4 Basic Properties of Ferroelectrics

The term ferroelectrics arose by analogy with ferromagnetics, mainly due to the similar characteristics that both systems possess [63]. The first polarization versus applied electric field loop was measured in 1920 by J. Valasek in Rochelle Salt [64]. Ever since, this class of materials was called ferroelectric. Ferroelectrics show a spontaneous electric polarization below the Curie temperature, a hysteresis curve, and an associated mechanical strain, nevertheless they differ from ferromagnets in their fundamental mechanisms and also in some of their applications [63]. Ferroelectricity is linked to the structural properties of a material and is not an intrinsic property of an atom [37]. Ferroelectric materials are pyroelectric[1], piezoelectric[2] and in some occasions ferroelastic [3]. Piezoelectricity, together with electrostriction, refers to electromechanical properties of crystals. From a technological point of view oxides with perovskite structures are of particular importance [65]. There are two types of mechanisms introducing ferroelectricity in a material: Order-disorder and displacement of ions. Ferroelectric perovskite Barium Titanate - $BaTiO_3$ (BTO) provide an example of displacement type.

2.4.1 Structure and Ferroelectric Order of $BaTiO_3$

BTO is a wide band-gap insulator with $E_g = 3.2$ eV [66] and is a ferroelectric material with a typical tetragonal distortion of the cubic perovskite structure. The unit cell of a cubic perovskite structure of BTO is illustrated in Fig. 2. 8. The Ti^{4+} ion is located in the center of the unit cell, Ba^{2+} ions occupy the corners and O^{2-} ions are located

[1] Pyroelectricity is a change in the polarization due to a change in temperature.
[2] Piezoelectricity is the accumulation of charges due to an applied strain on the material.
[3] Ferroelasticity is the presence of a spontaneous strain.

at the centers of the unit cell faces. Ferroelectricity of BTO is due to hybridisation between the Ti $3d$ states and O $2p$ states and the hybridisation is strongly enhanced by the ferroelectric distortion [65].

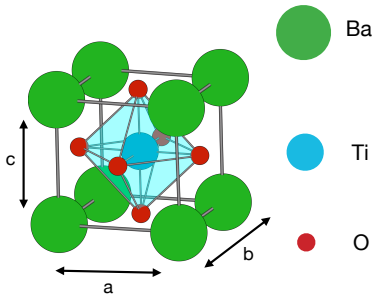

Figure 2.8: Perovskite structure of $BaTiO_3$. The Ti ion sits in an octahedron formed from six O atoms.

BTO is a room temperature ferroelectric with a spontaneous polarization of 26 μCcm^2. In the following sections the structural properties of BTO will be discussed. The structural phase changes associated with temperature and ferroelectric domain patterns will be emphasized.

The crystal structure of the different phases of BTO as a function of temperature is presented in Fig. 2. 9. The polarization direction is set by the relative atomic displacement. The central positive charge Ti^{4+} moves towards adjacent oxygen neighbours. The spontaneous polarization, P_S develops along six equivalent (100) directions. The critical transformation temperature from ferroelectric to paraelectric is called the Curie temperature (T_c). Above the Curie temperature (395 K for BTO), it has a centrosymmetric paraelectric cubic structure with five atoms per unit cell. At lower temperatures, the crystal has three successive ferroelectric (non-centrosymmetric) phases. In between the temperatures $395 - 275$ K the octahedral cages of oxygen distort and the Ti and Ba sublattices are shifted relative to the negatively charged oxygen lattice resulting in a spontaneous polarization. In the displacive model, the specific shift of atoms leads to a change of crystal structure from cubic to tetragonal, where the c-axis is elongated and $a = b$ axes are shortened [67]. Below 275 K, the preferred displacement direction of atoms changes (from <100> to <110>) and the structure converts to orthorhombic. Here $b = c$ and the non-rectangular angle only marginally diverges from 90°. The final phase transition occurs below 170 K, where the structure converts to rhombohedral (with <111> displacements).

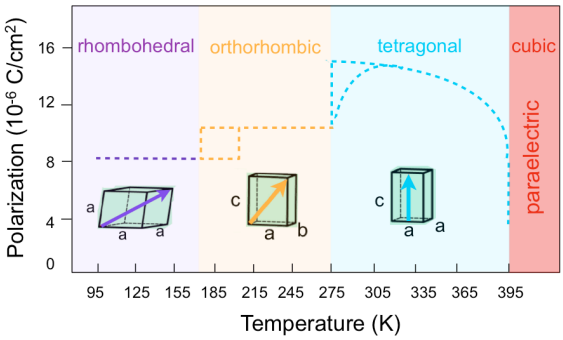

Figure 2.9: Schematic presentation of the structure of the different phases of $BaTiO_3$. Lattice changes along the b- and c- axes with respect to the tetragonal phase are indicated in the side-view of the rhombohedral, orthorhombic and cubic phases (Figure is adapted and modified from [68].)

2.4.2 Ferroelectric Domains and Domain Walls

Naturally, BTO single crystals are in multi domain state to reduce the strain field energy. Similar to ferromagnets, regions of same polarization directions are called ferroelectric domains. At room temperature BTO is in the tetragonal phase with the existence of two different ferroic domains: ferroelectric 180° and ferroelastic 90° domains. In ferroelectric 180° domains, the polarization is out-of-plane (Fig. 2. 10 (a)) and the domains are often referred to as c- domains [37]. Here, the unfavorable depolarizing electric field is provided by the abrupt polar discontinuity at the surface [69]. Due to the electrical charge accumulation at the surface, the presence of c-domains is unexpected in BTO thin films and in single crystals [70]. C-domains are driven by strain. The polar discontinuity charge builds up large dipolar-electric-fields, which are energetically unfavorable. However, if the elastic energy minimization by c-domains is bigger than the dipolar electric field energy, they tend to occur as well. Nevertheless, fast cooling through the phase transition temperature forbids for sufficient build-up of charges to compensate the dipolar fields caused by the spontaneous polarization [37]. As a result of 90° rotation of the polarization due to lattice mismatch a large ferroelastic strain occurs at the domain boundary. In the presence of an uniaxial or biaxial tensile strain in BTO films, 90° domains develop with almost equal areas of a1 and a2 domains [37]. Likewise, the establishment of a1-a2 domains in bulk BTO dominates, if the BTO is under pressure during preparation. As shown in Fig. 2. 10 (b), ferroelectric domain boundaries lie at an angle of 45° with respect to the polarization direction [37].

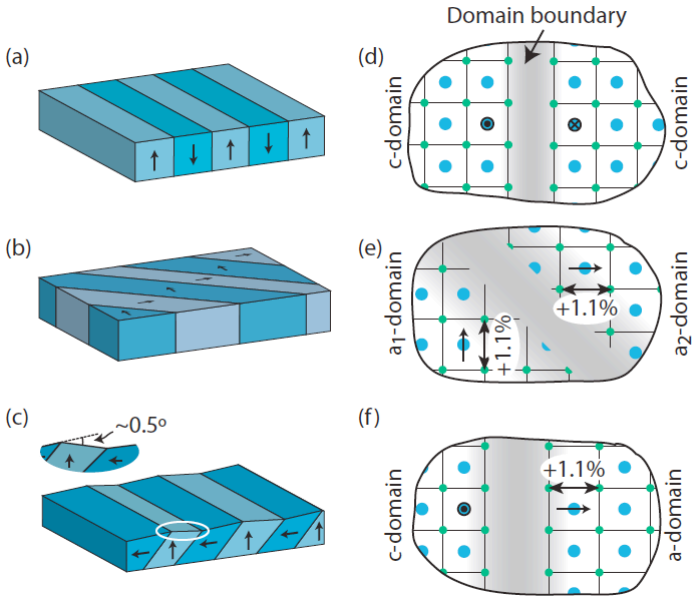

Figure 2.10: Ferroic domains in BTO(001) single crystals: c-domains are presented in (a), a1-a2 domains in (b) and a-c domains in (c) with an inset showing the angle between domains at the surface. The structural changes at the ferroelectric/ferroelastic domain boundaries are depicted in (d) to (f) [Taken from [37]].

To diminish the charging at the domain boundaries, the polarization in a1-a2 domains points head-to-tail in neighboring domains [37]. Furthermore, the change in the polarization direction is accompanied by the ferroelastic domain formation.
Alternative to a1-a2 domains, 90° ferroelastic a-c domains can also be present in BTO single crystals [37]. As shown in the inset of Fig. 2. 10 (c), there is a 0.5° bent at the a-c domain boundary due to unequal a- and c-domain out-of-plane lattice parameters [37]. Also here the polarization points head-to-tail to reduce charging.
In ferromagnets, domain wall formation is set predominantly by the exchange energy, which favors parallel alignment of spins. Therefore, as outlined earlier, magnetic domain walls display a gradual rotation of spins over lengths on the order of hundreds of nanometers to weaken the exchange energy [69]. In ferroelectrics, however, there is no exchange energy. The domain wall energy is dominated by the coupling between the polarization and the polarization reversal, thus ferroelectric domain walls develop on a

much shorter scale of a few unit cells [69].
Different ferroelectric domain wall widths (Fig. 2. 10 (d − f)) are observed for ferroelectric and ferroelastic domains in BTO. 180° ferroelectric domain walls occur between the out-of-plane domains (c-domains) with no in-plane component associated with polarization rotation, therefore the domain wall width is on the order of 0.5 nm [71]. In comparison to the ferroelectric domain walls, the ferroelastic domain walls are much wider due to a change in polarization direction and the lattice mismatch at the boundary. In Fig. 2. 10 ((d) and (f)) top-views of ferroelastic a1-a2 domains and a-c domains are illustrated. Expected ferroelastic domain wall width changes from 2 nm to 5 nm at the domain boundary [37].

2.5 Interactions across Ferroelectric/Ferromagnetic Interfaces

A material is multiferroic, if it has two or more primary ferroic orders which coexist in the same phase [72]. The properties of an ideal multiferroic material from the perspective of applications are: room temperature ferroelectricity and ferromagnetism, and strong MEC. However, there are only few single phase multiferroic materials with coupled ferroelectric (FE) and ferromagnetic (FM) order parameters and usually one of the order parameter is small. At this point, layered artificial multiferroics offer much more flexibility in the design of the desired ferroic properties [73]. When a ferroelectric (FE) and a ferromagnetic (FM) material are brought together, which originally have particular characteristics each, new phenomena emerge at the interface region and can combine to a magnetoelectric coupling (MEC). In magnetoelectric materials the magnetization is coupled to the ferroelectric polarization, so that a switching of the electrical polarization, for example by an external electric field, induces a change in the magnetic easy axis. For applications in electronic devices the magnetoelectric coupling is interesting, because the control of the magnetization state by an external electric field may significantly minimize the energy consumption of the device [74]. The magnetoelectric coupling is often caused by the magnetoelastic effect.
Magnetic anisotropy is originating from spin-orbit coupling. Any deviation from the initial orbital shape changes the magnetic anisotropy of the investigated system [75]. The change in mechanical strain of a system due to magnetization is assigned as magnetostriction. If a sample with randomly oriented magnetic domains is exposed to an external magnetic field, the magnetic domains align parallel to the applied magnetic field (only if the applied magnetic field is enough to overcome the domain wall energy.). During this alignment, the length of the sample slightly increases, which will induce mechanical strain.
In an Fe/BTO system the inverse magnetostriction effect, i. e. the magnetoelastic effect

is crucial. For example, if Fe is grown at elevated temperatures, such as T = 600 K, the BTO single crystal will be paraelectric. Upon cooling ferroelectric domains will develop at the first transition temperature at about T = 400 K. Associated with this process there will be strain states, which will be transferred to the ferromagnetic film deposited on top. Due to the phase transition from paraelectric to ferroelectric state, the lattice parameters of BTO will extend laterally, thus this lateral extension of BTO will be translated into the Fe film. Strained bonding at the Fe/BTO interface will affect the local magnetic properties of the Fe film.
To exploit the emergent phenomena at the interface between a ferromagnetic and ferroelectric material, control of the interaction at the interface is needed. The control of one degree of freedom will lead to a control of the coupling as well. Some of the fundamental control parameters which are important with respect to this work are:

- Control of the lattice using lattice mismatch or different crystal structures to induce strain in the material.
- Control of the spin and the orbital occupancy by the exchange mechanism between the different electronic phases.

Strain-control mechanisms to alter the magnetic properties of magnetic films depend on the competition between the magnetoelastic and the magnetocrystalline anisotropies as well as magnetostatic and exchange interactions [37]. For example, the magnetoelastic coupling between a magnetic thin film and a ferroelectric single crystal can be utilized to control the magnetic properties. By applying an electric field, an interfacial strain is created, upon which the lattice strain of the ferroelectric can be altered. If this is the case, a magnetoelastic anisotropy of the magnetic film is accomplished via the inverse magnetostriction effect.
The magnetoelastic anisotropy strength relies upon the efficiency of the strain transfer, which depends on the tetragonal lattice elongations of the ferroelectric and on the magnetoelastic properties of the magnetic film [37]. Additionally, depending on the ferroelectric crystal structure, its orientation, and the ferroelectric domain polarization direction, the magnetoelastic anisotropy-symmetry generated in the adjacent magnetic film can be varied. As presented by Lahtinen [37], the ferroelectric domain imprint into the magnetic films and a strong pinning of the magnetic domain walls on top of the ferroelectric domain boundaries can be set via local strain transfer.
Strain coupling between a BTO single crystal and a $La_{1-x}Sr_xMnO_3$ thin film was accomplished via structural phase transitions of BTO [76]. The authors showed that the lattice transitions modified the strain state and so the magnetoelastic anisotropy of the ferromagnetic film.
The overlap between the atomic orbitals rules the magnetic properties, which can be changed via atomic displacements at the FM/FE interface. Changes in the magnetic

moment have been demonstrated via ab initio calculations at an Fe/BTO interface [22]. The authors explained the effect in terms of hybridization between the Fe and the Ti 3d orbitals, which induce a charge redistribution of majority and minority spins depending on the Fe–Ti bond length.
The work presented in this thesis focuses on:

- Direct observation of the interaction between the electrical and the magnetic degrees of freedom in an all-oxide multiferroic system, that is BTO/LSMO/STO by means of x-ray absorption spectroscopy.
- Imaging and measuring of ferroelectric-ferromagnetic domain interactions in Fe/BTO metal/oxide hybrids using photoemission electron microscopy, in order to provide information on the strain-induced magnetostrictive effects in a magnetic film with spatial resolution and element sensitivity.

2.5.1 Sample Layouts

In order to understand the interactions across ferroelectric/ferromagnetic interfaces two different sample types have been prepared. Fig. 2. 11 (a) shows the two layer systems used in this thesis. For the investigation of electronic structure, magnetic and structural properties and surface morphologies of all-oxide ferromagnetic/ferroelectric heterosystems BTO/LSMO samples were prepared. The LSMO and BTO films were deposited onto Nb(0.5 %) doped $SrTiO_3$(001) single crystals with (001)-orientation. In order to obtain a single termination at the substrate surface, as-received STO substrates were prepared via a combination of wet chemical etching and a subsequent annealing procedure. The STO single crystal cleaning treatment will be given in detail in chapter 4.

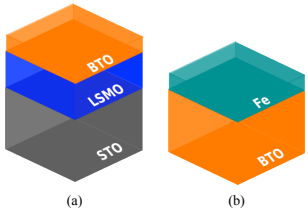

Figure 2.11: Schematic sample layouts used in this thesis.

We studied a second type of artificial multiferroic, namely a metal/oxide interface, i. e. Fe/BTO system (as schematically shown in Fig. 2. 11 (b)). For this, approx. 3 nm-thick Fe thin films were deposited on to a pre-cleaned $5 \times 5 \times 0.5$ mm^3 BTO(001) crystal (SurfaceNet GmbH) by molecular beam epitaxy (MBE) at room temperature in UHV. Details of the BTO surface treatment are given in Chapter 5.5.1.

2.6 Fundamentals of Absorption Spectroscopy

In this chapter some basic X-ray characteristics will be discussed in order to understand the features of the X-ray absorption data. Measuring the X-ray absorption coefficient as a function of photon energy near the absorption edge of the element of interest, $E = h\nu$, is called XAS. It is a widely used technique to obtain information on the chemical environment of the probed element, its valency and its spin state.
XAS was invented in 1913 by M. de Broglie. If the X-rays are absorbed by the sample, core electrons are excited to unoccupied electronic states. Free core level holes will then be filled again by the electrons coming from higher energy levels either by emitting a photon or an Auger electron. The attenuation of the radiation propagating in a continuous homogeneous material can be expresses by Lambert-Beer's law:

$$I(E, z) = I_0 \exp^{-\mu(E).z}, \tag{2.10}$$

where I_0 is the incident intensity of the radiation and I is the remaining intensity after the radiation has propagated the distance z inside the material [77]. The linear absorption coefficient $\mu = \mu(\hbar\omega)$ depends on the energy of the X-rays and is related to the absorption cross section $\sigma(\hbar\omega)$ $[\mathrm{cm}^2/atom]$ as

$$\mu = \frac{\rho N_A}{A}\sigma. \tag{2.11}$$

Here, ρ is the density of the sample, N_A is the Avagadro's number and A is the atomic weight of the sample. Usually, mass attenuation coefficient $\mu_m = \mu/\rho$ is given to avoid considerations of sample density. Basic parameters that contribute to the X-ray attenuation are [77]:

- Photoelectric absorption
- Elastic scattering (Rayleigh, Thompson)
- Inelastic scattering (Compton)
- The electron-positron pair production at energies above 1.022 MeV

The spectrum range of interest is soft X-ray regime, thus we will consider only photo-electron absorption coefficient. $\mu(E)$ contains an integration over all optical transitions into the empty density of states and the transition matrix element leads to the so-called dipole selection for the transitions between the states. Dipole selection rules for linearly polarized light are:

$$\Delta j = 0, \pm 1; \Delta l = \pm 1; \Delta m = 0; \Delta s = 0. \tag{2.12}$$

And for circularly polarized light:

$$\Delta j = 0, \pm 1; \Delta l = \pm 1; \Delta m = \pm 1; \Delta s = 0. \tag{2.13}$$

The dipole transitions are spin conservative and orbital moment selective as Δm is determined by the helicity of the photon $\Delta m = 1(-1)$ for left circular (right circular) polarization. Conservation of angular momentum stimulates spin-selective electron transitions, which in turn cause the magnetic dichroism. The number of transitions equal to the energy difference between the occupied initial states and the unoccupied final states. This is the case when a photon energy is high enough to excite a core electron into the continuum above the Fermi level, which is called an edge. As shown in the Fig. 2. 12 (b) the result is a sharp peak in the absorption coefficient.

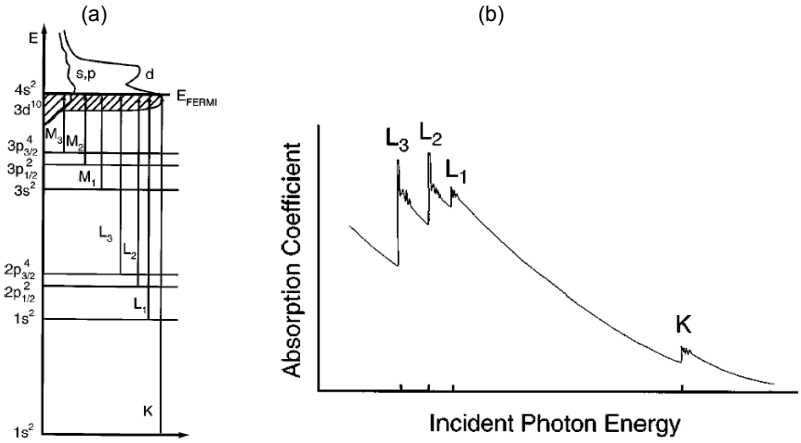

Figure 2.12: (a) The connection between the X-ray absorption edges and the excitations of core electrons corresponding to the K, L, M x-ray absorption edges. The threshold energy difference of each edge is shown by the arrows. (b) Scheme of the X-ray absorption coefficient as a function of incident photon energy. Four X-ray edges are shown: K, L_1, L_2 and L_3. The ionization energies are different for each element, therefore corresponding absorption edge measured at a certain energy is element specific [Figure is reproduced from Ref. [78] and references therein.].

The absorption spectra obtained by monitoring all electrons created during the absorption process is called total electron yield (TEY) mode. In the TEY mode the total number of electrons (photoelectrons, Auger electrons, secondary electrons) emitted from the sample are detected by measuring the sample drain current $I_{TEY}(E)$, which is proportional to the absorption cross section σ. Secondary electrons are the electrons ejected after the interaction of the primary Auger electrons and photoelectrons with the atoms of the sample. The number of emitted electrons is proportional

to the number of holes created in the sample, which in turn is proportional to the absorption coefficient. The mean free path of the secondary electrons, having an energy of 2 eV − 4 eV, is about 2 − 4 nm. Therefore, measurements in the TEY mode require atomically clean surfaces. One most note that the proportionality between the drain current I_{TEY} and the absorption cross section σ will most probably be demolished by self-absorption effects, if the probing depth of TEY is of the same order (or larger than) the attenuation length of the incident X-rays [79, 80].

2.6.1 X-ray Magnetic Circular Dichroism (XMCD)

Determining the magnetic moments element specifically and distinguishing their spin and orbital moments became possible by means of x-ray magnetic circular dichroism (XMCD) [81]. It was theoretically predicted for Ni $M_{2,3}$ edges by Erskine and Stern [82]. In the late 1980s circularly polarized light became first available in the hard x-ray regime in HASYLAB in Hamburg. Schütz et al.[83] experimentally proved the XMCD effect at Fe K-edge using hard x-rays. The XMCD effect was small, because the s-state has no spin-orbit coupling (L = 0). After the measurements performed by Chen *et al.* at the Fe L_3 and L_2 edges [84] [4] it became an often used method for the characterization of magnetic materials.

The XMCD effect is explained in the following for the example of $L_{3,2}$ absorption edges, which are also relevant absorption edges in this work. At the $L_{3,2}$ absorption edges, electron transition from $2p$ states into the $3d$ states takes place. Due to spin-orbit coupling the $2p$ level energetically splits into a $2p_{3/2}$ and $2p_{1/2}$ level. In a simple one-electron model, the XMCD effect can be considered as a two-step process: First, spin-polarized electrons are produced by absorption of circularly polarized light, then these spin-polarized electrons are transferred to an exchange split valence shell. Since spin flips are forbidden in electric dipole transitions, spin up (spin down) electrons can only make transitions into spin up (spin down) empty 3d-states. A schematic presentation of the process is given in Fig. 2. 13. The spin-split valence state serves as a spin detector for these spin-polarized electrons, and the transition probabilities are proportional to the empty d-states for a given spin direction.

Now we look more closely, how a net spin polarization of the exciting photoelectrons from the 2p core level is created [85, 86]: During the absorption process photons transfer their angular momenta to the photoelectrons. The electron spin could have an arbitrary orientation with respect to the orbital moment, and it is only through the spin-orbit interaction, that the spin orientation is related to this angular momentum.

In order to quantify the effects of the spin polarization, one should calculate the relative

[4] At the L_3 edge (L = 1), the spin-orbit coupling prevails in the initial state.

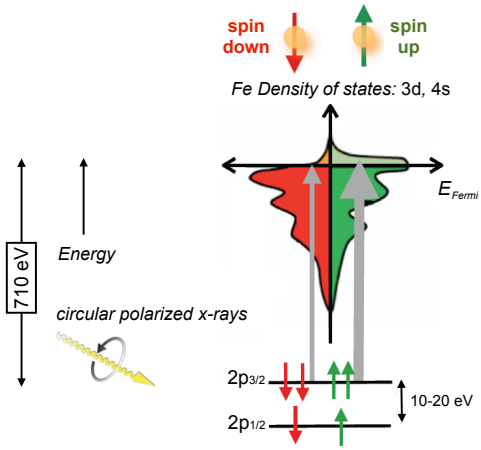

Figure 2.13: Schematic presentation of absorption process [Figure is reproduced from the Lecture Notes of Prof. Claus M. Schneider, Universität Duisburg-Essen.].

intensities of the transitions from $2p_{1/2,3/2}$ to 3d states. If we separate the transition matrix element, $M_{fi}^2 = |\langle f|\vec{e}.\vec{r}|i\rangle|^2$ into radial and angular parts, we obtain:

$$M_{f,i} = \delta(m_s', m_s)\langle n'l|r|nc\rangle\langle lm_l|e|cm_c\rangle, \tag{2.14}$$

where c, m_c are the angular momentum quantum numbers of the core levels and l, m_l are angular momentum quantum numbers of the final states, respectively. Since the angular part of the transition matrix element is connected to m_l, it is important for the dichroic effect. By using the spherical tensor notation for the angular parts of the transition matrix element one gets the matrix elements that involve only the spherical harmonics. This problem can be solved by using the Gaunt's Formula:

$$\langle Y_{lm_l}|Y_{\lambda q}|Y_{cm_c}\rangle = (-1)^{m_l}\sqrt{\frac{(2l+1)(2\lambda+1)(2c+1)}{4\pi}}\begin{pmatrix} l & \lambda & c \\ m_l & q & m_c \end{pmatrix}\begin{pmatrix} l & \lambda & c \\ 0 & 0 & 0 \end{pmatrix}. \tag{2.15}$$

The expression of the relative intensities can be written as:

$$I_{cm_cq} \propto |C_{jm_jcm_csm_s}\langle Y_{c+1m_{c+q}}|Y_{1q}|Y_{cm_c}\rangle|^2. \tag{2.16}$$

In order to determine the transition intensities for each transition, the transition matrix element has to be multiplied with the corresponding Clebsch-Gordan Coefficient.
From the measured XAS intensity and associated XMCD effect, spin and orbital magnetic moments of the final states can be calculated according to the so-called sum rules

[87]. Therefore, we calculate the integrals over the spin-orbit splitted edges. Sum rules are based on an atomic model (spherical symmetry) and a single electron picture, in which multiplet and solid state induced anisotropies are mainly neglected [87]. Sum rules are originally derived for systems with highly localized d electrons, thus the application of sum rules to the complex systems such as $La_{0.7}Sr_{0.3}MnO_3(001)$ is rather difficult. In strongly correlated systems the $2p-3d$ electrostatic interactions are relatively large compared to the 2p spin-orbit interaction. This stimulates a strong overlap in the $2p_{3/2}$ and $2p_{1/2}$ multiplets. As a result of this a significant mixing between these two j levels occurs. Since the spin-sum-rule is only valid in the limit of $j-j$ coupling, it should be corrected for $j-j$ mixing. The correction factor is obtained using the calculated Hartree-Fock values of the Slater integrals and the core spin-orbit interaction.

2.6.2 X-ray Linear Dichroism (XLD)

The X-ray Linear Dichroism (XLD) describes differences in the absorption behavior using linearly polarized X-rays caused by a charge anisotropy. In most cases, the anisotropy of the charges in the atomic volume is caused by the anisotropy of the bonds, for example, by an inhomogeneity of electrostatic potential. In the absence of a spin arrangement XAS can determine the charge ordering in the system, but only if the symmetry of the absorbing atoms is lower than cubic symmetry [88]. Since the electric field vector oscillates along an axis and the radiation may be absorbed at any time, the linearly polarized x-rays are sensitive only to properties with axial symmetry. In case of a soft x-ray absorption spectra taken at the $L_{2,3}$ absorption edges of Ti, electrons are excited from the $2p_{3/2}$ and $2p_{1/2}$ core levels into the 3d states. For linearly polarized light, the electric field vector of the x-rays acts like a search light for the number of valence holes in different directions of the atomic volume [89]. Consider the d_{z^2} orbital: If the electric field vector is parallel to the z axis, the absorption will be high, while the absorption will be lower for the electric field vector lying in the xy plane or including any non-vanishing angle with the z axis [89].
In the case of tetragonal symmetry with $c>a$, the relation between the x-ray absorption at the Ti $L_{2,3}$ edge and the 3d orbitals is presented in Fig. 2. 14. The two absorption lines arise as a result of electronic transitions towards the lower energy d_{xz}, d_{yz} and d_{xy} orbitals on the one hand and the higher energy d_{z^2} and $d_{x^2-y^2}$ on the other hand [89]. Owing to hybridization effects, orbitals pointing towards the oxygen ligands yield broader lines in the absorption spectrum [89]. The additional energy splitting due to the Ti displacement is too small to be directly visible in the absorption spectrum. However, it can be analysed by measuring the dichroism between two different directions of linear polarization [89, 73].
Filippetti and Hill calculated the density of states for Ti^{4+} in BTO for a cubic and

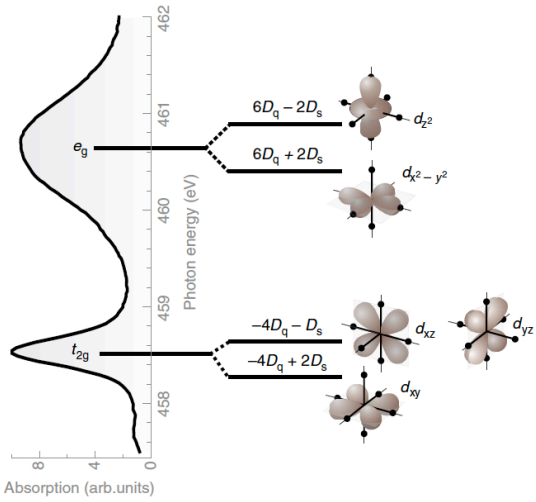

Figure 2.14: The Ti L_3 edge XAS (left) is related to the Ti ion energy levels in the crystal field for positive values of $10D_q$ and negative values of D_s (D_t is neglected.) [89]. The value of the crystal field parameter $10D_q$ denotes the energy splitting between the t_{2g} and e_g states in a cubic symmetry, whereas D_s takes into account the deviation from a cubic symmetry including the displacement of the Ti^{4+} ion [89]. In the tetragonal phase, the energy levels of the cubic e_g and t_{2g} states further split into sublevels [Taken from [89]].

tetragonal unit cell by a plane wave pseudopotential implementation of density functional theory within the local spin density approximation (LSDA) and linked it to the atomic orbitals [90]. In the tetragonal phase, the displacement of the Ti^{4+} from its centrosymmetric position along the z direction splits up the d_{xy} orbital and the d_{xz} and d_{yz} orbitals [89]. In terms of crystal field parameters, this splitting corresponds to the introduction of a negative value of D_s as depicted in Fig. 2. 14. However, from the parameter D_s, the geometric structure cannot be obtained directly [89]. Here the negative value of D_s is associated with an elongation of the BTO unit cell along the z direction. This is in agreement with XRD data in the literature revealing that the elongated axis of the tetragonal BTO is parallel to z [89].

Chapter 3

Experimental Methods

In this chapter, the experimental tools and techniques involved in fabricating samples and measuring their magnetic, surface and electrical transport properties are described. Thin oxide films of LSMO and BTO are grown by means of pulsed laser deposition (PLD), and thin metallic iron films are grown via molecular beam epitaxy (MBE), which are briefly introduced in section 3. 1. Magnetic, structural, and chemical pre-characterization methods are summarized in section 3. 2. Magnetic characterization of the samples was performed by superconducting quantum interference device (SQUID) magnetometry (see Section 3. 2. 1). In section 3. 2. 2, the working principle of atomic force microscopy (AFM) is reviewed, which was employed for the investigation of the topography and surface roughness of samples. A brief introduction to X-ray diffraction (XRD) is given in section 3. 2. 3, which was used in order to study the structural properties of all-oxide hybrids. Auger electron spectroscopy (AES) was utilized to check the cleanness and the chemical composition of the BTO single crystal surfaces and is shortly explained in section 3. 2. 4.
In section 3. 3, the basic properties of synchrotron radiation, the UE56/1-SGM beamline and a brief description of the interaction between x-rays and matter is given. Finally, in the last section of this chapter the low energy electron microscope/ x-ray photoelectron emission microscope (LEEM/XPEEM) instrument is introduced, which was used to perform synchrotron-based layer-resolved measurements.

3.1 Sample Growth Techniques

3.1.1 Pulsed Laser Deposition (PLD)

Pulsed Laser Deposition (PLD) is a well-established technique to grow ultrathin epitaxial[5] heterostructures made of oxides under controlled conditions. Deposition of materials takes place in a vacuum environment, with an oxygen background pressure of 10^{-4} mbar. The most important aspect of PLD is the precise control of oxygen stoichiometry of complex oxides. LSMO and BTO thin films used in this thesis were fabricated in a PLD chamber in PGI-9[6] by Dr. Jürgen Schubert. The PLD setup in PGI − 9 is depicted in Fig. 3. 1.

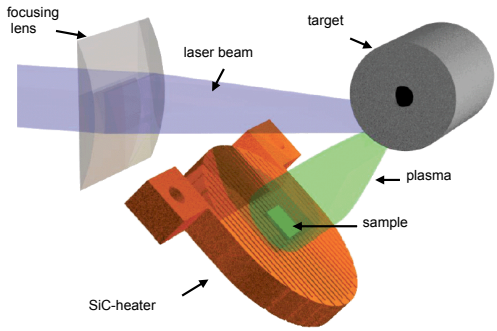

Figure 3.1: Schematic presentation of PLD setup at PGI-9. In a vacuum chamber, elementary or alloy targets are hit at an angle of 45° by a pulsed and focused laser beam. The atoms and ions ablated from the target are deposited on substrates. The substrates are placed on a SiC-heater with the surface parallel to the target surface. Figure is taken from [91]

In the PLD chamber the target material is ablated from a rotating cylindrical target by a short pulse of an excimer laser beam via a suitable optical sytem [92]. The laser beam is produced by a 248 nm wavelength KrF excimer laser. The pulse duration is varied from 5 ns to 250 ns, depending on the desired thickness of the ablated material. The typical laser energy density on the target is varied from 2 J/cm^2 to 4 J/cm^2 [92]. The cylindrical targets consist of single phase, pressed and sintered BTO and LSMO powders. A high energetic plasma beam of the target material is generated in the

[5]Epitaxial growth reproduces the crystallographic structure of the substrate in the deposited material.

[6]Peter Grünberg Institute-Semiconductor Nanoelectronics

direction of the substrate by the laser ablation. To achieve monocrystalline growth substrates are held at high temperatures varying from T = 550°C to 650°C. For this the $SrTiO_3$(001) single crystal substrates are placed on a resistive SiC heater inside the PLD chamber [92]. For proper oxidation of the films, materials are ablated under constant oxygen pressure. At the sample position standard oxygen pressures of $5x10^{-3}$ mbar up to 0.5 mbar can be reached [91]. One of the advantages of the PLD growth technique is a high deposition rate. The deposition rate is determined by the laser power and the pulse rate. It can reach $10^2 - 10^5$ nm/sec.

3.1.2 Electron Beam Evaporation

The deposition of iron films was carried out with an Omicron EFM-3T electron beam (e-beam) evaporator *in situ* in front of the objective lens of the LEEM/XPEEM microscope and in the preparation chamber. Iron films were deposited on clean $BaTiO_3$(001) single crystal substrate surfaces from a 99.99 % pure iron rod with a diameter of 2 mm purchased from Mateck GmbH. We employed room temperature deposition to avoid any thermal activation of interlayer diffusion during iron growth. At a given electron emission of the e-beam evaporator, filament current of $I_{Fil} = 2$ A, emission current of $I_{Emis} = 13$ mA, and accelerating voltage of U = 950 V, the ion flux was measured at the beam exit column with an ion collector. The ion flux is directly proportional to the flux of the evaporated atoms ($I_{Flux} = 80$ nA). To roughly calibrate the flux monitor of the evaporator, we studied the Ti (461.3 eV) from the substrate ($BaTiO_3$) and Fe (709 eV) from the growing film. We compared the XAS total electron yield (TEY) peaks. Increasing the Fe film thickness increased the Fe TEY intensity and decreased the Ti TEY intensity. We calibrated the TEY intensity changes of Fe and Ti peaks as a function of Fe coverage and calculated the Fe thin film thickness from the calibration.

3.2 Magnetic, Structural, and Chemical Pre-characterization Methods

3.2.1 SQUID (Superconducting Quantum Interference Device) Magnetometer

To measure global magnetic moments of thin LSMO films we used the most sensitive magnetometer, which is based on SQUID technology. The measuring principle of SQUIDs is based on Josephson junctions [93]. A SQUID device has a closed superconducting loop consisting of one or two Josephson junctions in the loop's current

path. The system used in PGI-4[7] is a SQUID magnetometer manufactured by Quantum Design (MPMS MultiVu)[94]. The principle of operation rests on RF-SQUID[8]. The superconducting loop, however, is not directly connected to the circuit, but is inductively coupled to a high frequency LC[9] resonator.
In more detail, the SQUID magnetometer measures the longitudinal magnetic moment of a sample, along the direction of an applied magnetic field. In the MPMS MultiVu system the magnetic field in the range of ±7 Tesla can be applied using a superconducting solenoid. We note that with increasing distance from the center of the coil the homogeneity of the field decreases. The temperature at the sample location can be set in the range from T = 2 K to 400 K. The sensitivity of the SQUID magnetometer is in the order of 10^{-9} emu (10^{-12} Am^2).

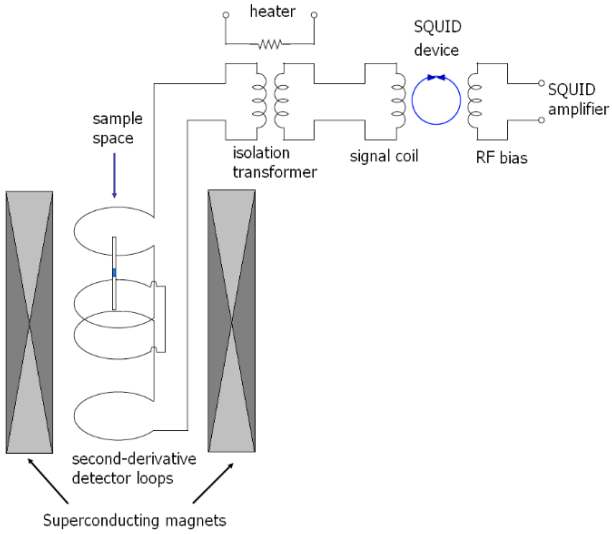

Figure 3.2: Schematics of an RF-SQUID device. The SQUID acts as a magnetic flux-to-voltage converter. This voltage is amplified and read out by the magnetometer's electronics [taken from[95]].

Schematics of a RF-SQUID device are shown in Fig. 3. 2, the sample space is positioned within a superconducting detection coil ("pick-up" coil). A single piece of superconducting wire is wound in a set of three coils. This configuration eliminates the contribu-

[7] Peter Grünberg Institute-Quantum Materials and Collective Phenomena
[8] i.e. radio frequency SQUID (also called as: alternating current AC SQUID).
[9] L:Inductor, C: Capacitor

tions from external fields and the pick-up coils become sensitive to the stray field of the sample only. Superconducting magnets produce a uniform constant magnetic field over the whole coil region and the pick-up coils are placed in between them (see Fig. 3. 2). The sample is suspended on a rod, which is installed at the top of the cryostat to a vertical transport mechanism [95]. The sample is slowly moved through the pick-up coils. The magnetization of the sample induces an electrical current in the pick-up coils and any change of magnetic flux in them produces a change of the steady current in the detection circuit, which is proportional to the change in magnetic flux [95]. The SQUID serves as a linear current-to-voltage converter, thus the variations in the current in the detection coil produce corresponding variations in the SQUID output voltage. The output signal, V, is recorded as a function of scan length, z. A curve-fitting algorithm of the MPMS software fits the measured $V(z)$ data points to the theoretical curve of an ideal dipole and so extracts the magnetization [95, 96, 97]. In this thesis, the magnetization measurements were done by using an RSO (Reciprocating Sample Option) sample holder. In an RSO measurement, the sample moves sinusoidally twelve times through the detection loops for one saved data point. Then, the average of these value series is taken, which guarantees a more precise result in comparison to the single DC[10] measurements [95].

3.2.2 Atomic Force Microscopy (AFM)

Scanning probe microscopy (SPM) techniques provide real space imaging of surface structures with atomic resolution [98]. There are variations in the nature of the interaction between the tip and sample, but the working principle and the basic components of SPMs are the same: A very sharp tip is positioned at a specific small distance from a sample. In this thesis, the information on the surface morphology of the samples is obtained by atomic force microscopy (AFM). In an AFM, the force between the tip and sample is employed to map the surface. Figure 3. 3 illustrates the AFM working principle. An extremely sharp tip ($2 - 15$ nm in radius of the tip end curvature) is mounted on a flexible cantilever. The bending of the cantilever is directly related to the force acting on the cantilever, and is monitored by a laser beam reflected by the cantilever. The deflection of the laser beam is measured by a position sensitive photodetector (PSPD). The PSPD has four segments, and it detects cantilever deflections caused by normal and lateral forces and converts these forces into a voltage. There is a feedback system, which keeps the tip exerting a constant force on the sample surface. During the constant force mode, the deflection of the cantilever is used as an input to a feedback circuit that moves the scanner up and down in z-direction [99]. The control voltage in a feedback loop is measured for each scanning point and this corresponds to

[10] direct current

the sample surface topography by keeping the cantilever deflection constant.

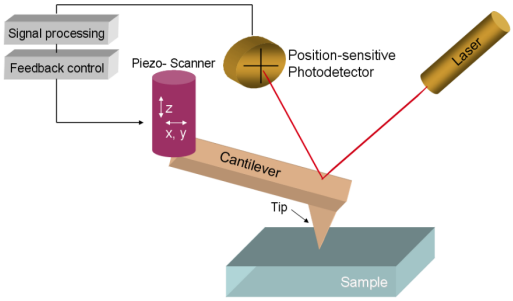

Figure 3.3: Schematic working principle of AFM. It consists of a cantilever with a sharp tip at its end. During scanning the tip taps the surface and is deflected due to van der Waals forces between the tip and the surface. The deflection is measured by a laser beam that is reflected from cantilever onto a position-sensitive photodetector (PSPD). Then the degree of the deflection of the cantilever is measured by the PSPD and converted in to a voltage. Subsequent to the measurement of the voltage for each scanning point and plotting, a map of the sample surface is obtained.

There are three main classes of scanning modes, i.e. the contact mode, tapping mode and non-contact mode. In this thesis the AFM data were obtained with an atomic force microscope from Digital Instruments in the tapping mode using a silicon tip. In the tapping mode the cantilever oscillates at its eigenfrequency in the z-direction, generally at hundreds of kHz. Upon approaching the sample, the tip starts to interact with the sample and this changes the frequency of the tip. In the tapping mode, this change is kept zero via a feedback loop, thus lateral forces are minimized and the risk of damaging sample is reduced in contrast to the contact mode [95]. In this mode, the repulsive part of the van der Waals forces [11] between tip and sample is measured indirectly by measuring the deflection of the cantilever. An extremely precise positioning device is made from piezo-electric ceramics for the movement of the tip (or the sample). This ceramic is able to perform sub-angstrom resolution in x-, y- and z-directions [95]. The surface morphology can be quantitatively analyzed with AFM. The definition of the RMS[12]-roughness is given as the vertical (standard) deviation $z(x)$ of a surface from ideal flatness, where $z(x)$ is the height profile[101].

[11] The van der Waals forces represents the electromagnetic interaction of fluctuating dipoles in the atoms of the tip and surface [100].

[12] RMS: Root Mean Square

The RMS-roughness is calculated using

$$R_{RMS} = \left[\frac{1}{N} \sum_{n=1}^{N} (z_n - z)^2 \right]^{1/2}, \tag{3.1}$$

where N is the number of data points within the box cursor, i.e. a defined area is selected from the AFM image, z_n is the height data of the n^{th} point, and z is the average height. Notably, the RMS roughness does not provide information about the local structure of the surface, i. e., even if the morphologies of the surfaces are not identical, both surfaces could yield same RMS roughness.

3.2.3 X-Ray Diffractometry (XRD)

X-ray diffraction (XRD) is an extensively used method for the characterization of the structural properties of crystals, polycrystalline and amorphous samples or layer systems [102]. Information on the crystal structure, crystal orientation and crystalline quality, lattice constants, purity of the phase, layer thickness and surface roughness can be provided via an XRD measurement. The room temperature XRD measurements included in this thesis were performed with a Philips X′pert MRD four-circle diffractometer with $\mathrm{Cu} - \mathrm{K}_\alpha$ radiation in the Bragg-Brentano configuration to probe the crystallinity of the films. In Fig. 3. 4 the schematics of the four-circle geometry is shown.

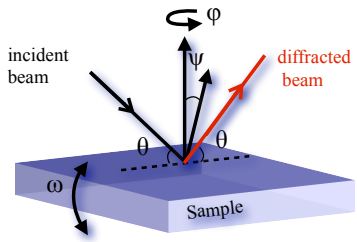

Figure 3.4: Sketch of the four-circle x-ray diffractometry (Reproduced from [103]).

The detector angle 2θ and the sample angle θ or ω can be rotated independently from each other in the plane defined by the incident and the diffracted beams [103]. In this configuration the interplanar distances for the planes parallel to the substrate surface can be measured. The ϕ and ψ rotations permit the determinations of interplanar distances of the planes that are not parallel. The incident x-ray beam is reflected from parallel planes of atoms in the crystal, with each plane reflecting only a very small fraction of the radiation. When the path difference is an integer number of wavelengths

diffracted beams interfere constructively. The spacing between diffracting planes, d_{hkl} with hkl being the Miller indices of this plane, can be determined by Bragg's law:

$$2d_{hkl}sin\theta = n\lambda, \tag{3.2}$$

here θ is the incident angle, n is an integer, and λ is the wavelength of the x-ray beam. Additional properties of the epitaxial films can be determined by measuring ω-scan of a Bragg reflection, i. e., rocking curve measurement. In this case, the direction of the scattering vector is being changed. The full width at the half maximum (FWHM) of the rocking curve provides a measure of mosaicity (variation in ω), lattice strain (variation in $\omega/2\theta$) and limited layer thickness [103].

3.2.4 Auger Electron Spectroscopy (AES)

One of the standard analysis techniques in surface science to study the surface chemical concentration is Auger Electron Spectroscopy (AES) [104]. Considering the limited escape depth of Auger electrons, AES is very surface sensitive. Typical probing depths in AES are in the range of $10 - 30$ Å. In this work, AES was employed to study the cleanliness of freshly prepared BTO single crystal surfaces under UHV conditions.
AES is based on the principle of Auger electron release and is a three-electron process: Firstly, an atom is bombarded by an electron beam, which ionizes the inner shell of that atom and a core hole is created. Secondly, the core-hole is filled by an electron from an outer shell. Simultaneously, the energy gained upon decay of an outer shell electron is given to another electron in the same outer shell, which is eventually emitted from the atom at a well-defined kinetic energy [105]. This emitted electron is called Auger electron. The emitted Auger electron carries a particular kinetic energy which is related to the difference in core-level energies. By measuring this kinetic energy chemical analysis becomes possible [104].
The AES setup used for this thesis (STAIB GmbH) consists of an electron gun, which produces a focussed electron beam [21]. In our setup, the electron gun is usually operated at 5 keV and the sample current is of the order of $I_{sample} = 5$ μA. The emitted Auger electrons from the sample are deflected back to a single-pass cylindrical mirror analyzer, where the electrons are energy filtered and detected by a channeltron. The spectrum of emitted Auger electrons is usually displayed as a function of the first derivative of the kinetic energy, dN/dE [21]. The differentiation is performed by modulating the voltage and detecting the signal from the electron multiplier with a lock-in amplifier. Presentation of AES in this mode suppresses the large background of secondary electrons [105].

3.3 Soft X-Ray Beamline UE56/1-SGM (FZ Jülich Beamline at BESSY-II)

3.3.1 Generation and Basic Properties of Synchrotron Radiation

The electromagnetic radiation emitted by an accelerated charged particle moving with a constant and relativistic velocity on a circle is called synchrotron radiation (SR). Although the theoretical work of principles were established at the end of the nineteenth century [106], first SR was observed at the General Electric 70 MeV synchrotron accelarator in Schenectady, New York, on April 24 1947 by Elder et al. [107]. The emitted light was identified to be polarized with an electric field vector parallel to the plane of the electron orbit [108].
The application of SR has an enormous contribution in modern physics, chemistry, biology, and material sciences. SR experiments provide basic understanding of the structure, the electronic properties and the collective phenomena of the system under study [109]. To be able to perform such an experiment highly monochromatized and intense radiation with tunable polarization and energy is needed. BESSY-II[13] is a 3rd generation source [110] of the Helmholtz-Zentrum Berlin (HZB). In this chapter the generation of SR and its properties are briefly described. Some of the important characteristics of the SR are:

- high intensity
- wide spectral range covering the IR[14], visible light, UV[15], soft[16] and hard x-ray[17]
- highly collimated[18]
- high degree of polarization
- pulsed time structure
- high brightness of the source due to small cross section of the electron beam

SR is generated when a relativistic particle of normalized energy γ is accelerated and γ is defined as:

$$\gamma = \frac{E}{m_0 c^2}, \tag{3.3}$$

[13] BESSY: Berliner Elektronenspeicherring-Gesellschaft für Synchrotronstrahlung m.b.H.
[14] Infrared
[15] Ultraviolet
[16] Soft x-rays, 80-2000 eV
[17] The distinction between hard and soft x-rays is not well defined. Hard x-rays are typically those with energies greater than 2 keV.
[18] This property of SR provides high flux on very small areas also at far distances from the storage ring.

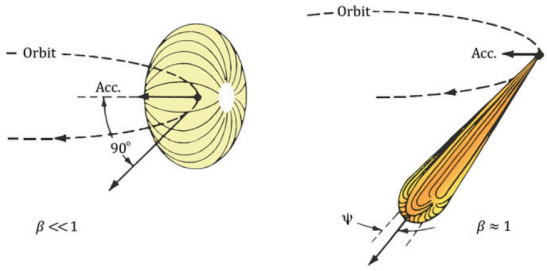

Figure 3.5: Qualitative radiation patterns related to charged particles moving in a circular orbit. The dipole pattern achieved for slow particles (left) is distorted into a narrow cone when $\beta = v/c \approx 1$ (right) [Image is adapted from [111]].

with E its energy, m_0 the particle mass, e the particle charge and c the speed of light. When the charged particle is subjected to a magnetic field B_d of a few Tesla, the particle is brought onto a curved path, i. e., there is an acceleration perpendicular to the main motion, which causes a radiation emission in the tangential direction [108]. The movement of the particle is given by the Lorentz equation.

$$\frac{dp}{dt} = e\left(E + \frac{v \times B}{c}\right), \tag{3.4}$$

here p, e, and v are particle momentum, charge and velocity, respectively. B and E are the electric and magnetic field.

For the compensation of the energy losses radio frequency (RF) cavities are used. The electrons are grouped in bunches with time lengths on the order of $5 - 10$ % of the RF period, thus the SR is pulsed with the same time duration and separation. This provides the opportunity to perform time-resolved experiments like studying the magnetization dynamics with soft x-rays [112, 113].

As sketched in Fig. 3. 5, for non-relativistic particles the electromagnetic radiation is emitted into all directions except the direction of the accelaration: The emission characteristics has a donut shape. In the synchrotron, the electron velocity is close to the speed of light c, therefore when these relativistic electrons travel through a bending magnet, the dipole distribution is rather narrow and light is emitted tangential to the electron orbit. The vertical half-opening angle, ψ (as shown in Fig. 3. 5) is given by:

$$\psi \approx \frac{mc^2}{E} \approx \gamma^{-1}. \tag{3.5}$$

For BESSY-II with $\gamma = 3320$ the vertical half-opening angle is $\psi \approx 0.3$ mrad, thus SR is highly collimated. The spectral distribution from the bending magnet emitted radiation is a continuous broad spectrum. The polarization of the SR emitted by a bending magnet is linearly horizontal with the electric field vector of the emitted electromagnetic wave parallel to the plane of the electron orbit. Furthermore, the electrons in a storage ring move along the circular orbit and emit SR along the tangent, thus in a bending magnet the horizontal collimation is lost [114]. Nevertheless, by using undulators as insertion devices the collimation can be preserved in both directions [114].
An insertion device (ID) consists of sequences of very strong magnets of constant period length installed in a straight section of a storage ring. The general layout of such magnets is shown in Fig. 3. 6 at different settings. IDs provide an increase in the intensity of the emitted radiation by a factor related to the number of wiggles induced by the magnets, and high brilliance.
There are two kinds of IDs: wigglers and undulators. Here we will focus on the undulator, since it is relevant in this work. The energy of the SR emitted from an undulator depends on the distance between the magnets in the x- and y- direction and the magnetic field strength $B(T)$. The resolution of the undulator radiation is set by the number of undulator periods N_u and for high resolution large numbers are demanded.
One of the key feature of SR emitted from an undulator is its polarized nature [116]. For the experiments presented in this thesis both variable photon energy and variable x-ray polarization is needed. Any polarization of the light, such as linear, elliptical or circular, can be generated by changing the relative alignment of the magnet-arrays along the x-axis, as shown in Fig. 3. 6. An undulator having such structure is called elliptical undulator (UE). The polarization is described by the relationship between the two orthogonal components of the electric field **E** of the x-rays as:

$$E_x = E_{xo} cos(\omega t) \tag{3.6}$$

$$E_y = E_{yo} cos(\omega t + \delta). \tag{3.7}$$

There are three independent parameters, the field amplitudes, E_{x0}, E_{y0} and the phase difference δ. When the phase difference is zero the light is linearly polarized, with the angle given by the relative field amplitudes. If the phase difference is $\pi/2$ and $E_{x0} = E_{y0}$ then the light will be circularly polarized.

3.3.2 Beamline Instrumentation and Operation Principle

In order to use SR in an experiment monochromatization is required. There are two classes of monochromators: diffraction gratings and crystal monochromators, which are preferred depending on the photon energy range. The double crystal monochromator is the most common type in the hard and intermediate x-ray range [117]. In the soft

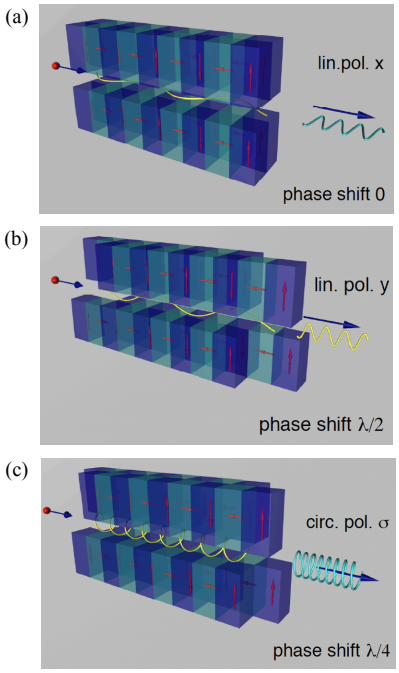

Figure 3.6: Schematic drawing of an APPLE insertion device at different settings. (a) Linear mode without shift (linearly horizontally polarized light). (b) Linear mode with shift set to half period ($\lambda/2$) (linearly vertically polarized light) of the magnetic structure. (c) Circular mode. The shift ($\lambda/4$) is set to the position with equal amplitudes of the horizontal and vertical magnetic fields (quarter period of the magnetic structure) (Figures adapted from [115]).

x-ray regime diffraction gratings are used. A diffraction grating is a surface with a periodic structure and it acts as a dispersive element. The condition for constructive interference is given by:

$$n\lambda = d(sin\theta_i + sin\theta_d), \tag{3.8}$$

with d being the distance between the lines of grating, θ_i and θ_d are the angles of the incident and diffracted beam, respectively λ is the wavelength and n is an integer.

In order to make the synchrotron radiation generated in the undulator accessible to the experiment, a setup of guiding mirrors, i. e., beamline is needed. Beamlines are photon delivery systems that start at the storage ring vacuum chamber and continue onto the experimental area to combine the experiment endstations [118]. The selection

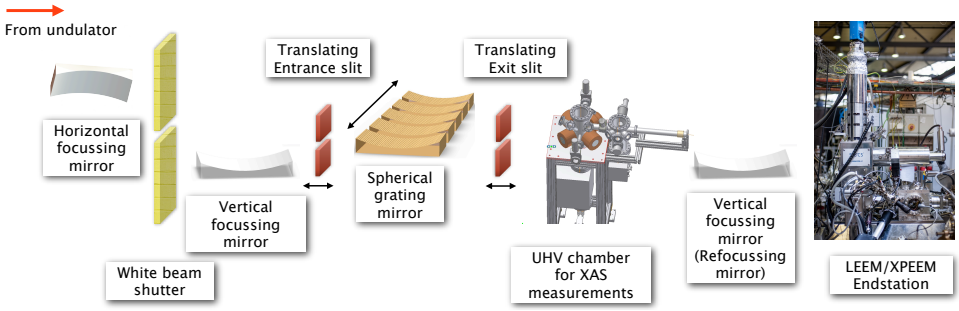

Figure 3.7: Schematic layout of UE56/1 – SGM FZ Jülich soft X-ray beamline with the optical elements, slits and UHV chamber for performing XAS measurements and LEEM/XPEEM endstation.

of a specific photon energy is accomplished by diffracting the incident (white) beam on an optical grating according to Bragg's law [62]:

$$n\lambda = d(cos\alpha - cos\beta), \tag{3.9}$$

with d being the line spacing of the grating and α and β are the entrance and exit angles, respectively. By tilting the grating to a desired combination of these angles a single photon energy can be selected [62]. If one combines a diffraction grating with an entrance and an exit slit, it can be used as a monochromator. The diffracting grating used in FZ Jülich soft X-ray beamline (UE56/1-SGM[19]) at BESSY-II is spherical grating mirror (SGM) type. The monochromator houses five different exchangable gratings with line densities of 200, 350, 800, 1200 and 1600 lines/mm. To achieve high resolution and high intensity a combination of slits and mirrors is needed. X-ray absorption spectroscopy (XAS) experiments presented in this thesis were carried out at the FZ Jülich soft x-ray undulator beamline of BESSY-II, Berlin. Fig. 3. 7 shows a schematic layout of the FZ Jülich beamline. This beamline is designed for performing XAS studies with high resolution in total electron yield mode. The typical path of the non-monochromized x-rays from the source to the sample starts with mirrors to image the source point onto the entrance slit of the monochromator to get all photons. As presented in Fig. 3. 7, the translating exit slit cuts a defined energy interval ΔE from the angularly dispersed energy distribution [62]. Behind the monochromator there is a refocusing mirror and a gold grid to make the divergent beam to converge on the sample [117] and to measure a photocurrent proportional to the photon flux of the beamline,

[19] UE56/1-SGM: Undulator-Elliptical, 56=period length in mm, SGM: Spherical-Grating Mirror

respectively. The beam spot size at the sample is 100 μm x 100 μm and before doing measurements beamline alignment is mandatory.

3.4 Combined Low Energy Electron and X-ray Photoelectron Emission Microscope (LEEM/XPEEM)

One of the important research areas which utilizes the bright and monochromatized X-rays obtained at a synchrotron is X-ray Photoelectron Emission Microscopy (XPEEM). In this process photoelectrons are stimulated at the X-ray absorbing material and leave the sample surface after undergoing series of inelastic scattering processes. Photoelectrons which suffer inelastic scattering turn into secondary electrons. Secondary electrons are accelerated by the objective lens and hit the MCP[20]. Here, the secondary electrons are multiplied and reaccelerated, and eventually detected by the phosphorous screen. The local photoemission on the phosphorous screen is detected by the CCD[21] camera.

The intensity variations on the phosphorous screen depending on the photon energy correspond to the electron yield [119]. Therefore, each XPEEM image can be interpreted as one single spatially resolved data point in XAS. When a set of several XPEEM images is recorded on the same sample position for several photon energies, the intensity in the CCD camera can be read out pixel by pixel and plotted versus photon energy [119]. Furthermore, the aperture allows only electrons with low kinetic energies to pass, which are the most important charge carriers for XAS [119]. Several groups showed that the resulting spectra are intimately related to the absorption of the sample [88, 119]

Combined with a Low Energy Electron Microscope (LEEM) the XPEEM is a unique tool to study structural, chemical, electronic and magnetic properties of micro- and/or nanometer sized materials. Utilizing soft X-rays, the core electrons of the material become accessable and enable one to perform element specific imaging. By using polarized X-rays and by taking the advantage of X-ray linear dichroism and X-ray magnetic circular dichroism effects, it is possible to investigate the ferro- and antiferromagnetic domain structures of surfaces and interfaces of thin films, micro- and nanostructures element selectively and with high lateral resolution as presented here. Nowadays, there are several companies manufacturing diverse LEEM/PEEM microscopes. Elmitec, Focus, Omicron and SPECS are to name some.

[20] Multi channel plate
[21] Charge Coupled Device

3.4.1 Working Principle

In this thesis all LEEM/XPEEM experiments have been performed with the SPECS FE-LEEM P90 AC (see Fig. 3. 8 (a)).

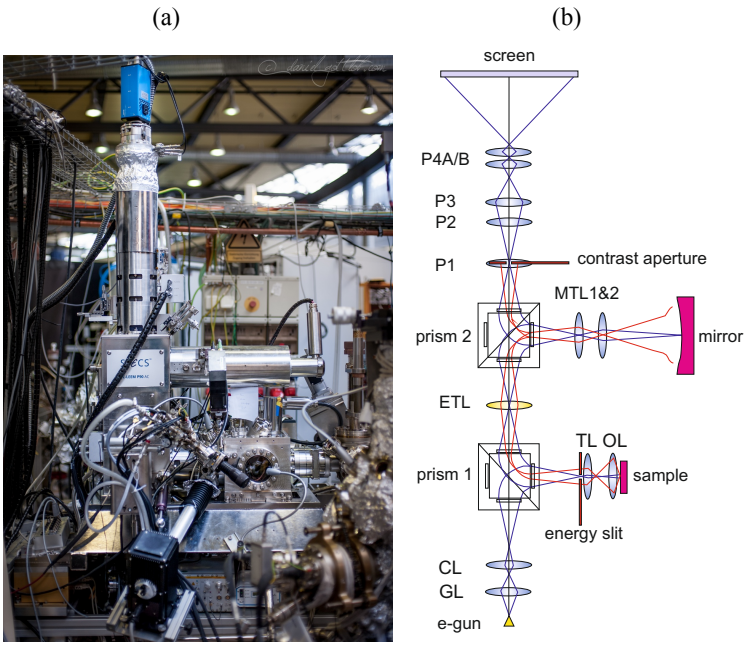

Figure 3.8: The FE-LEEM P90 installed as an endstation at the FZ Jülich beamline UE56/1-SGM in BESSY-II, Berlin, Germany. Image courtesy to D. M. Gottlob.

This microscope is a versatile tool to study complicated systems and processes. Imaging in low energy electron microscopy (LEEM) is facilitated by electrons either reflected from the surface of the material or emitted from the material. The scattered electrons from the surface of a material can be used not only for imaging in real space, but also imaging in k-space (diffraction pattern). The low energy diffraction (LEED) pattern plays an important role on selecting and controlling the contrast mechanism for imaging and is described in more detail in section 3. 4. 2. One of the substantial advantages of a combined LEEM/PEEM microscope is the opportunity to get structural information from the same sample using LEEM and LEED modes, thus enabling one to study structural, electronic and chemical properties of a material in parallel. Furthermore,

it is capable of monitoring the growth processes of magnetic or non-magnetic metallic films.

The fundamental property of FE-LEEM P90 AC is that the sample is part of a cathode objective lens system. The distance between the objective lens and sample is 1.5 mm [120]. The sample sits at a potential of about −15 kV.

In the LEEM mode, the sample is illuminated with a collimated beam of 15 keV high energy electrons, which are generated by a cold-field emission gun. These electrons are focused by a gun lens (GL) (see Fig. 3. 11 (b)) and a condenser lens (CL) into the entrance plane of the first magnetic prism array (prism 1) [120]. Then, the electron beam is deflected over a 90° angle into the objective lens system. The objective lens (OL) and magnetic transfer lens (TL) belong to this system [120]. Since the sample is held at negative voltage around −15 kV, the energy of the electrons that reach the surface is not −15 keV, but only a few eV. The electrons possessing a kinetic energy changing from 0 eV to 100 eV interact with the sample and are re-accelerated to 15 keV. In the backfocal plane of the OL a diffraction pattern is created, whereas the real space image is formed at 60 mm away from the sample [120].

The task of the TL is to transfer the diffraction pattern to the entrance plane of prism 2, and to place a virtual image in the center of prism 1 with a magnification of 38x [120]. Prism 1 disperses the electron with different energies with a dispersion of $\approx 6\mu$/eV in the plane of electron transfer lens (ETL). This dispersion is removed by prism 2. A magnetic transfer lens (MTL 2) transfers the diffraction pattern to the reflection plane of the electron mirror, which matches and cancels the chromatic and spherical aberrations C_c and C_3 of the objective lens, and transfers the real space image back to the center of MTL 2, still at a magnification of 8.5, but now aberration-corrected [120]. Chromatic dispersion is recovered in the ETL plane, which allows one to perform spectroscopic experiments without an additional energy filter in the projector column [120].

Mostly, elastically backscattered slow electrons are utilized for imaging. LEEM is a direct and a (virtually) non-destructive imaging method to study and to understand the static or dynamic physical properties of single crystal surfaces or thin films such as growth, decay, phase transitions, reactions, structure, and morphology. The advantages of LEEM over the other imaging techniques are:

- The ability to perform real-time imaging.
- There are diverse contrast mechanisms for imaging, such as: dark field LEEM and bright field LEEM.
- The ability to work under high temperature up to T=1200 K and high base pressure $P = 10^{-6}$ mbar.

3.4.2 Low-energy Electron Diffraction (LEED) and μ-LEED

As stated above, the microscope can also be used as a local LEED probe, which is a unique property for studying surface structures. The focus length of the some lenses makes the difference between the imaging and the diffraction mode. In order to examine the long range order of a surface we have performed LEED measurements in our microscope. The electron diffraction can be represented by the Ewald sphere construction in reciprocal space. In the LEED mode, the sample surface is illuminated with electrons of well-defined energies changing from a few to 1000 eV in normal incidence. The electrons are elastically diffracted and accelerated towards the phosphor screen and they appear on the screen as bright spots. The LEED pattern is interrelated to the image of the reciprocal space. The LEED spot intensity is proportional to the number of electrons in the corresponding electron beam. With an aperture placed in the electron gun beam path before the sample, the area can be restricted down to sub-micron scale. Hence, this working mode of the microscope is called micro-LEED (μ-LEED). This extra feature of our instrument offers the possibility to study the surface of the sample even beyond the micro-scale down to, for example, 200 nm.

3.4.3 Bright Field and Dark Field LEEM

The contrast aperture placed in the diffraction plane enables one to perform real-space LEEM imaging using electrons either diffracted in the zero or in the higher order diffraction spots. An example of dark field and bright field LEEM images of a submonolayer Au film grown on an oxidized Rh surface is presented in Fig. 3. 9 [121]. If one uses the zero order diffraction spot (00), i. e. the backscattered electrons that go through without momentum transfer parallel to the surface, for imaging, one works in the so-called bright field mode (see Fig. 3. 9. b). The contrast in this mode derives from structural changes. It depends on the diffraction amplitude's local variations of the backscattered electrons for the different surface regions. Using the first order diffracted electrons for imaging is called dark field mode (see Fig. 3. 9. a)). Dark field imaging is done by tilting the illumination beam away from the optical axis by the Bragg angle of the diffracted beam of interest. In this mode the areas which are contributing to the second order diffraction look bright. The contrast obtained in bright and dark field LEEM depends entirely on the structure of the material under investigation. The contrast is given by the local changes in the diffaction amplitude of the different surface phases. The regions which produce the corresponding LEED spots appear bright and the rest of the surface remains dark.

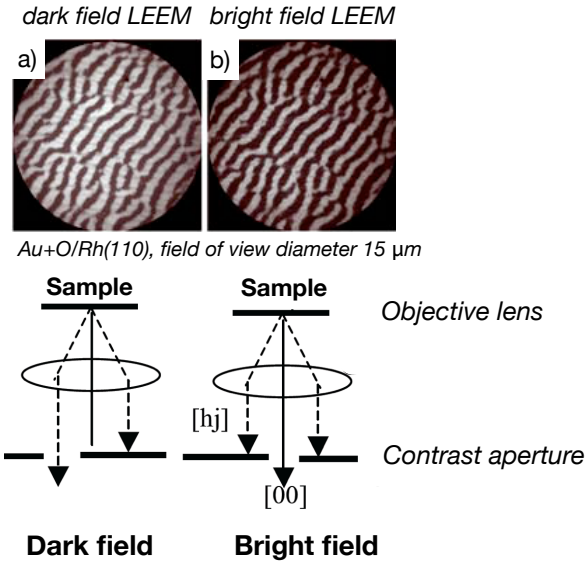

Figure 3.9: Dark field LEEM (a) and bright field LEEM images of a submonolayer Au film grown on an oxidized Rh surface [Figure is adapted from [121]].

3.4.4 Mirror Electron Mode (MEM-LEEM)

In the FE − LEEM P90 AC instrument, both the electron gun and the sample sit at a bias of −15 keV [120]. When a collimated electron beam impinges on the surface these electrons are decelerated by the sample to a few volts, called the start voltage (SV), thus electrons have an energy of 0 eV with respect to the sample [122]. At very low SV, electrons are reflected by the surface potential (MEM), whereas at higher values they penetrate the sample and are backscattered (LEEM) [122]. The MEM-LEEM transition, i. e. the transition from the reflection of the electrons to the back-scattering regime, measures the electrostatic potential above the surface [122].
MEM can be used to study the full surface electrical topography [122]. By scanning the start voltage a 3D image stack of the surface can be obtained. The intensity of each image at a particular start voltage V is defined as $I(x, y)$. Each pixel bar (x, y) of the 3D stack relates to a reflectivity curve $I(V)$ [123]. The MEM contrast corresponds to the differences in photoemission threshold at the surface and it is a perfect tool to probe surface charge differences in domains with a polarization component perpendicular to

the surface, pointing either inwards (P ↓) or outwards (P ↑)[122]. At the surface, an in-plane electric field will be created at the boundary between oppositely polarized domains due to the fixed charge [122].

3.4.5 XPEEM

In XPEEM, X-rays are used to excite photoelectrons. The photon energy is adjusted to an absorption edge specific to the material under study. Thus, a core electron makes a transition to the density of empty states of the same atom. If one uses soft X-rays as an external stimulus for the transition, the core levels will be most probably filled via Auger process. In this process, the high-energetic Auger electrons will experience a series of inelastic scattering processes in the solid. As a result of the scattering events an avalanche of secondary electrons will be formed. For imaging in XPEEM these secondary electrons are used. Since the allowed transitions are element specific, this feature of XPEEM allows one to map the local chemical contrast of the material. In other respects, if the photons are circularly polarized, one can greatly benefit from studying the spin-dependent allowed transitions. A local magnetic map of the material can thus be obtained by XMCD. One takes images using right- and left-circularly polarized X-rays. These images are normalized according to:

$$A = \frac{I(\sigma^+) - I(\sigma^-)}{I(\sigma^+) + I(\sigma^-)}, \tag{3.10}$$

where A is the asymmetry, $\mathrm{I}(\sigma^{+(-)})$ is the image intensity obtained by using circularly right (left) polarized X-rays.
Nearly all of the most exciting new discoveries in thin film magnetism are observed in multilayered structures in which two or more magnetic layers are contributing. Obtaining the magnetic structure of each layer is crucial. If the elemental composition of the multilayered structure is known, one can perform element specific XPEEM measurements. Figure 3.10 shows an example of how magnetic contrast is obtained using XMCD. It shows the layer-resolved magnetic domain structure. The raw image of a Co/Ni bilayer on Cu(001) obtained with circularly polarized X-rays of positive helicity tuned to the maximum of the Ni L_3 absorption edge is presented in Figure 3.10 (a). The stripe-like magnetic contrast represents the lateral distribution of XMCD [124]. Depending on the magnetization, i. e. either the magnetization direction is parallel or antiparallel to the helicity of the incoming X-rays, XMCD leads to a different X-ray absorption within a domain. This is depicted in Figure 3.10 (a) [124].
To prove the magnetic origin, the X-ray helicity must be reversed. Figure 3.10 (b) shows the same image, but for opposite X-ray helicity [124]. Since the topographic contrast in the image does not depend on the X-ray helicity, differences between images (a) and (b)

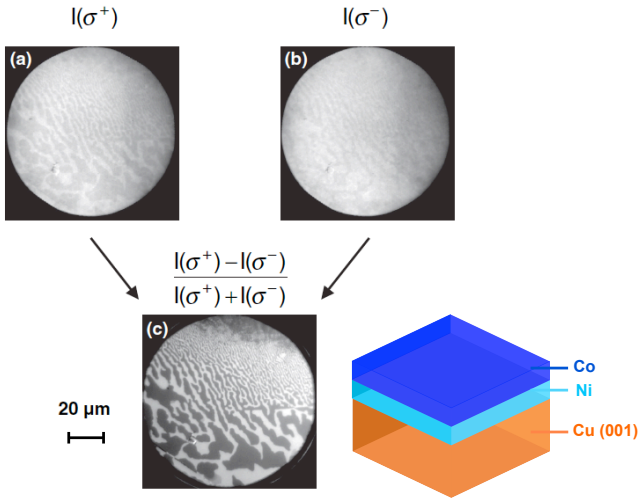

Figure 3.10: Demonstration of magnetic contrast in XMCD-PEEM. (a): X-PEEM image of Co/Ni/Cu(001) obtained with circularly polarized X-rays of positive helicity at the Ni L_3 edge, (b): same with negative helicity. (c): Asymmetry image calculated from the images (a) and (b) showing the magnetic contrast [124].

are of purely magnetic origin [124]. As expected for magnetic contrast, the stripe-like pattern indeed reverses its contrast, when the direction of the helicity vector is reversed. In order to eliminate all topographic contrast and obtain a magnetic domain image of the sample, the two images obtained for opposite helicity of the circularly polarized X-rays are subtracted [124]. The result, the intensity difference $\mathrm{I}(\sigma^+) - \mathrm{I}(\sigma^-)$ divided by the sum $\mathrm{I}(\sigma^+) + \mathrm{I}(\sigma^-)$, is called asymmetry [124]. The asymmetry image calculated by using Eqn. 3.10 is presented in Figure 3.10 (c) [124]. Dark and bright areas in that image correspond to domains of opposite magnetization directions [124].
Using XPEEM one can investigate ferroic properties of a multiferroic material such as $BiFeO_3$, which has gained much recent attention due to its room-temperature ferroelectric and antiferromagnetic properties. The magnetoelectric coupling in $BiFeO_3$-based nanostructured systems has been measured in a spatially resolved manner via both XMCD and X-ray magnetic linear dichroism (XMLD) imaging with the so-called natural linear dichroism due to structural sources of the electronic anisotropy such as ferroelectricity also present in such systems.

Chapter 4

Ferromagnetic/Ferroelectric All-Oxide Heterostructures: BTO/LSMO/STO(001)

In this chapter, we present and interpret the experimental data, which provide insights into magnetoelectric coupling phenomena in BTO/LSMO/STO(001) all-oxide hybrids. We describe the growth and physical properties of the LSMO half-metal ferromagnet combined with ferroelectric BTO epitaxially grown onto STO(001) substrates by the PLD technique. We study the morphological, structural, magnetic and electronic structure properties of BTO/LSMO heterosystems. In the first step, we optimize the growth conditions of LSMO and BTO thin films individually. In the second step, we provide an accurate information about differences in electronic and structural properties in LSMO thin films as a function of the oxygen pressure during BTO growth.

4.1 STO(001) Single Crystal Preparation

Nb(0.5%) doped $SrTiO_3$ (STO) single crystals with (001)-surface orientation were used as substrates for the BTO/LSMO bilayer growth. Commercially available STO single crystal (001) surfaces consist of alternating SrO and TiO_2 atomic layers [125]. As-received substrate surfaces have mixed terminations. *Ex-situ* annealing in air or in oxygen atmosphere improves the surface quality, but it does not provide a single termination of the surface. To prepare an atomically smooth, nearly perfect and uniquely terminated STO surface we took advantage of the difference in physical and chemical properties, e. g. solubility of the Sr- and Ti-cations in acids as described in [126] and further developed the recipe. STO substrates were cleaned in aceton and propanol for 10 min each in an ultra-sound cleaning system to remove the organic and ionic

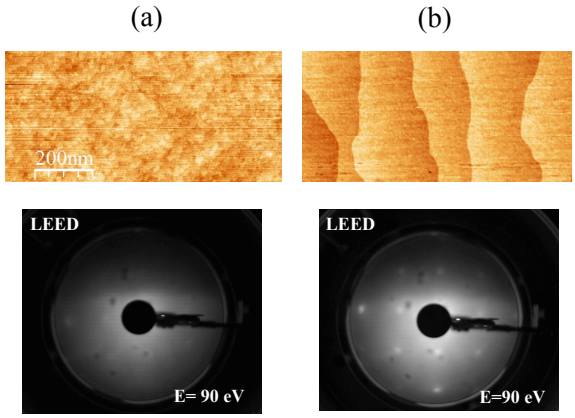

Figure 4.1: (a) AFM image of an as-received STO single crystal surface and the corresponding LEED image in the lower panel. (b) AFM image of a TiO_2 terminated STO substrate prepared using the method described in the main text and the corresponding LEED patterns in the lower panel of (b): (1x1) lattice and no surface reconstruction.

impurities. Substrates were afterwards ultrasonically rinsed in distilled water for 10 min, which was followed by a short (30 sec) dip in a standard commercially available NH_4F buffered hydrofluoric acid solution. Then, the substrates were rinsed (ca. 12 sec) with distilled water in order to stop the etching process. Subsequently the substrates were annealed in a glass tube furnace at 950°C under 0.5 mbar oxygen pressure for four hours to remove the organic residues and to smoothen the surface. Figure 4. 1 (b) reveals the successful terrace formation on the STO substrate by AFM measurements after cleaning treatment. AFM images showed that the substrate in the initial state had a mixed termination, but the cleaned substrate was atomically flat and had a single termination: TiO_2. (1x1) lattice LEED patterns improved after cleaning (presented in the lower panel of Figure 4. 1 (a) and(b)), proving the impact of the cleaning on surface termination.

4.2 LSMO/STO(001)

In order to understand the magnetoelectric coupling phenomena at the BTO/LSMO interface and to interpret the effect of the BTO ferroelectric electrode on the physical properties of LSMO, informations on the uncapped LSMO films are needed. Thus, we

initially studied the magnetism, the surface morphology and the electronic structure properties of thin LSMO films in detail.

Bulk LSMO exhibits an ordering temperature of $T_C = 370$ K with a magnetic saturation moment $M_S = 3.7\ \mu_B$ per unit cell, which is originating from the double-exchange mechanism. Double exchange in LSMO arises from the itinerant e_g electrons coupled to the localized t_{2g} electrons and, therefore, the Mn mixed valence is uniform [11].

The examined samples were fabricated by means of PLD, and the sample layout was LSMO/STO, with LSMO film thicknesses ranging from d = 100 to 120 nm. LSMO films were deposited on pre-treated STO substrates under same conditions. The stoichiometry of the LSMO films was analyzed by Rutherford Back Scattering (RBS) method and determined to be $La_{0.66}Sr_{0.33}MnO_{3-\delta}$ within the uncertainty of the method (about 5 %) [91]. We noted that the sensitivity of the RBS method was insufficient to determine the amount of oxygen in the films.

Fig. 4. 2 shows the temperature-dependent magnetization curves of a 100 nm thick LSMO film. The schematic layout of the sample is given in the inset of the figure. During the measurements an in-plane magnetic field of H = 50 Oe was applied along the [100] axis. In Zero-Field-Cooled (ZFC) measurements, the sample is cooled in (nominally) zero magnetic field down to 8 K and then the magnetic field was applied. In Field-Cooled (FC) measurements, the sample is cooled under applied magnetic field. Data are collected while warming up the sample under the magnetic field.

Performing ZFC and FC measurements on magnetic systems is a method to conclude, whether the system under investigation possesses exchange biasing, and if yes, how strong this interaction is. Also, it allows one to determine the ferromagnetic and antiferromagnetic ordering temperatures of the film.

The $M(T)$ data showed more than one magnetic transition due to the coexsitence of magnetic phase inhomogeneities. The splitting of the FC and ZFC $M(T)$ curves was linked to the presence of exchange bias [95].

The magnetic ordering temperature, i. e. the Curie temperature T_C, was determined by the intersection with the abcissa of the linear extrapolation of maximum absolute value of the slope [91]. The ferromagnetic order of the LSMO film sets in about 290 K, which was smaller than that of the bulk material.

Oxygen-deficient manganites generally possess lower T_C than stoichiometric samples [127, 128, 129]. This was elucidated by Ju and Sohn [128] as an establishment of magnetic inhomogeneities in the LSMO film [91]. According to their interpretation different ferromagnetic regimes exist in the film and these regions are not perfectly aligned and are even separated by nonmagnetic regions, where Mn^{3+} ions accumulate. The inhomogeneous structure causes a smaller magnetic coupling and a lower Curie temperature [91]. Furthermore, analogous to oxygen-deficient LCMO (C = Ca) films, LSMO films

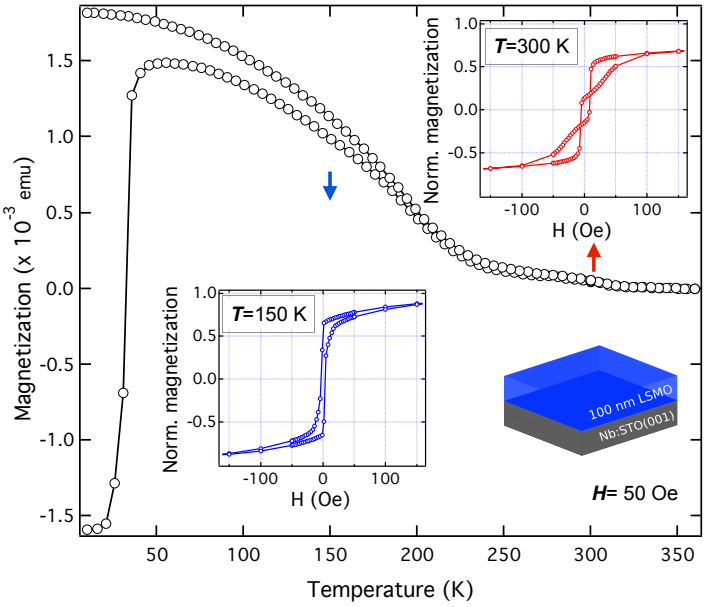

Figure 4.2: Temperature-dependent magnetization cuves of as-grown LSMO(100 nm)/STO(001) film taken in the zero-field-cooling (ZFC) and field-cooling (FC) conditions. Insets show the hysteresis loops taken at different temperatures.

deposited under low oxygen pressures (not shown here) displayed properties of spin-glass systems, which can be explained by the inhomogeneity model[128, 129].
We claimed that the difference in the magnetization between the ZFC and FC curves around the low temperature regime was caused by the presence of randomly oriented magnetic domains. The domains were difficult to align in the film under the applied magnetic field of 50 Oe. These disordered spins might cause a spin-glassy behavior.
The insets show the hysteresis loops of the same LSMO film performed at different temperatures. The hysteresis loops are characterized by four important parameters: the saturation field H_{sat}, the remanence magnetization M_R, the saturation magnetization M_S and the coercive field H_C. The coercive field is a property that is related to the magnetic anisotropy, grain boundaries and pinning defects of a ferromagnetic thin film. The hysteresis loop at room temperature showed rather a mixed hysteresis curve. We observed a change towards a common ferromagnetic behavior accompanied by an increase of the remanent magnetization M_R/M_S at low temperature (T = 150 K). At T = 300 K the remanent magnetization M_R became negative. As can be seen in the

Fig. 4. 2, when the magnetic field was reduced from positive saturation, the sign of the magnetization was reversed, due to the positive coercive field present in the system yielding a negative remanence for H = 0 Oe [130].
Unconventional magnetization reversal mechanisms in LSMO/$SrRuO_3$ superlattices with ultrathin layers have already been observed and were interpreted by the interplay of magnetocrystalline anisotropy energy, antiferromagnetic exchange coupling strength and interfacial Bloch wall width [131]. However, the question arises, how the exchange bias effect can be present in a system without an antiferromagnetic film. The observation of the exchange bias effect suggested the presence of antiferromagnetic regions in the film. The magnetic depth profile analysis using PNR[22] on a PLD-grown LSMO/STO bilayer measured at T = 5 K and under H = 1 T revealed a completely ferromagnetically ordered LSMO layer [91]. On the other hand, a region with reduced magnetization was detected for samples grown by HSD[23] at the interface with the STO substrate, however, whether this interface region was macroscopically non-magnetic or possessed a small net magnetization cannot be gained by PNR measurements [91]. The XRMS[24] experiment results presented by D. Schumacher [91] yielded a non-zero magnetization for the interface region of about 20 % to 30 % of the rest of the LSMO layer magnetization.
The presence of a spin glass behavior as a result of magnetic frustration could be linked to the competition between the AFM super-exchange and the FM double-exchange interactions at the interface of LSMO with the non-magnetic part of the LSMO film. We then conclude that the canted AFM moments associated with spin glass behavior were responsible for the EB effect.
In addition to microscopic quantities like magnetic moments, the magnetic properties of thin films are also affected by vacancies, incomplete layers and the substrate roughness. In order to understand how the magnetization depends on the roughness and whether the conductivity of the LSMO film correlate with the topography, we studied the morphology of the sample surfaces by local conductivity atomic force microscopy (LC-AFM) in contact mode.
Figure 4. 3 (a − d) and (e − h) display the surface morphology of an as-deposited 100 nm thick LSMO film and the corresponding LC-AFM images, respectively. The atomic-force micrographs presented the terrace structure of the underlying $SrTiO_3$ substrate on the LSMO film; no other features were detected [132]. Conducting areas were shown black, while white regions corresponded to the insulating behavior. AFM pictures clearly indicated that topography correlates very well with the conductivity measurements. In order to quantify the surface characteristics, we utilized the roughness anal-

[22] Polarized Neutron Reflectivity
[23] High Oxygen Pressure Sputter Deposition
[24] X-Ray Magnetic Resonant Scattering

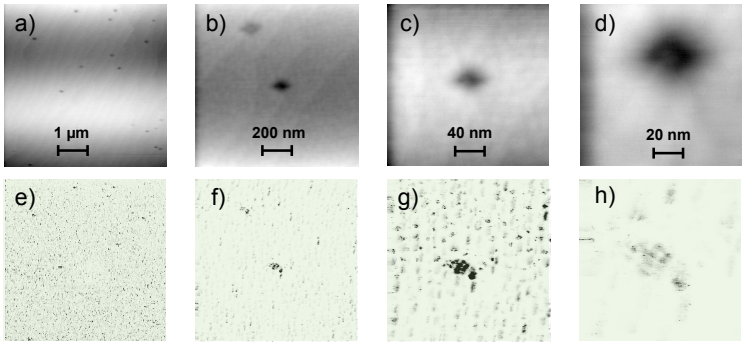

Figure 4.3: The relation between the topography and the local conductivity maps on LSMO(100 nm)/STO(001). a-d) show the topography and e-h) show the corresponding local conductivity maps. The black color in the conductivity images refers to high conductivity. The straight unit-cell high surface steps are visible in the topography image. The local conductivity is correlated with the topography of LSMO film, i. e. the conductivity is high on the etch-pits.

ysis [101] option for studying the evolution of surface morphology. The RMS roughness [101] is a parameter extracted from AFM data, which is quantified by the vertical deviations of a real surface from its ideal form [101]. If these deviations are large, the surface is rough, if they are small, the surface is smooth [95]. The RMS roughness was calculated from the AFM height profile at different scan sizes, in order to accurately determine the RMS roughness. We found that the film was very smooth with an RMS roughness of 0.2 nm. The film conductivity was inhomogenous: On the etch pits the conductivity is higher than the rest of the film surface. Spatial distribution of the different phases in the nanometer range affirmed the theoretically predicted percolation behavior [6]. The anticipated domain structure was not connected to the microstructure and was an intrinsic phenomenon of the films as described in [6].
To investigate the strain effect on the electronic structure of LSMO films, absorption measurements with polarized X-rays (XAS) were carried out in total electron yield (TEY) mode. XAS with polarized photons is sensitive to orbital ordering and in the TEY detection mode one can probe up to a few nm below the surface/interface [73]. In bulk LSMO, the octahedral coordination of cations at Mn-sites splits the Mn 3d-orbitals into a degenerated t_{2g} triplet and e_g doublet with (xy, yz, xz) and $(x^2 - y^2, z^2)$ symmetries, respectively. Further lowering of the crystal field symmetry breaks the orbital degeneracy of e_g doublets. This symmetry breaking is driven by the half-filling of the

e_g orbitals. The strong electron-phonon coupling induces a distortion of the MnO_6 octahedron yielding alternating long and short Mn-O-Mn bond lengths (Jahn-Teller (JT) distortion) that lift the $(x^2 - y^2, z^2)$ degeneracy, which in turn modifies their electron occupation and leads to the complex orbital ordering (OO)[133]. In $La_{1-x}Sr_xMnO_3$, the electron occupancy in the $(x^2 - y^2, z^2)$ orbitals strongly depends on the hole doping level (x) and the strength of the JT distortion. Additionally, epitaxial strain in LSMO thin films breaks the $(x^2 - y^2, z^2)$ orbital degeneracy. Depending on the type of the biaxial strain a preferential occupation of the orbitals develops [57]: tensile strain favoring the $x^2 - y^2$ occupancy, and compressive strain favoring the z^2 occupancy [8].
It is a particularly challenging task to investigate the orbital occupancy of the distinct orbitals, especially at buried interfaces [73]. One of the first studies on OO in $La_{1-x}Sr_{1+x}MnO_4$ was presented by Huang *et al.*[134]. In that paper, as well as in [135], authors performed XAS measurements to provide information on the OO in $La_{1-x}Sr_{1+x}MnO_4$.
Multiplet structures of complex oxides are fingerprints for valency and site symmetry [73]. If there are oxygen vacancies, the Mn valency can be used as a trace, since it changes from 2+ to 7+.[73]. In order to directly probe the orbital character of 3d states polarization-dependent XAS measurements were performed at the Mn (2p) edge. All spectra were normalized to the photon beam intensity I_0, measured by the TEY of a gold grid. A linear background was fitted to the pre-edge region of the spectrum and substracted from it. Afterwards, both spectra were normalized to the TEY signal at the post absorption edge region. LD was obtained by subtraction of the two XAS signals as in Ref.[73].
The result is presented in Fig. 4. 4. The general lineshape of the spectra was very similar and was broadly consistent with the XAS characteristics of manganites [43]. The spectra showed two pronounced edges due to transitions into the localized 3d states producing a $2p_{3/2}$ core hole at lower photon energy and a $2p_{1/2}$ core hole at higher photon energy. The distinguishing feature of the different XAS spectra was the main shoulder at 642 eV, which was associated to the Mn^{3+} high spin contribution [43, 73].
Using linearly-polarized X-rays, two spectra can be measured when the polariazation vector is set parallel to the c-crystallographic axis or perpendicular to it (I_c and I_{ab}, respectively) [134]. The difference ($I_c - I_{ab}$) yields the linear dichroism (LD) and sheds light on the empty Mn 3d states [134].
Mn^{4+}, unlike Mn^{3+}, does not tend to distort its octahedral environment by the JT effect, thus the observation of LD was in agreement with the presence of Mn^{3+}. The preferential orbital ordering was caused by the cooperative orientation of the distorted octahedral environment around the Mn^{3+} ions. Distorted octahedra were cooperatively oriented and generated a preferential orbital ordering [43]. Our results were further in agreement with the spatial variations of the local conductivity on a sub-micrometer

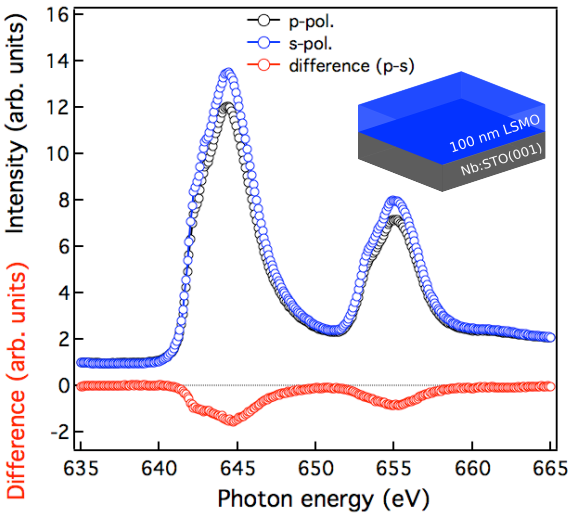

Figure 4.4: XAS and LD measurements of LSMO(100 nm)/STO(001) recorded in TEY at the Mn $L_{2,3}$-edge. The sample is kept at room temperature (non-magnetic). The spectrum displayed by black open circles is recorded with p-polarization, whereas the spectrum displayed by blue open circles is recorded with s-polarization. Lower panel: Measured linear dichroism, LD=$I_c - I_{ab}$.

scale observed with LC-AFM experiments (see Fig. 4. 3). It was a clear indication of the Mn^{3+} content enhancement in less conductive samples in order to preserve the charge neutrality [43]. According to the transport measurements performed by Aruta *et al.* [43] on similar LSMO films, a higher hopping energy corresponds to an increase of the Mn^{3+} content. JT distortions around the Mn^{3+} ion cause small polarons which localize the charge carriers, thus the conductivity decreases.

4.2.1 Optimization of LSMO thin films

The key to have coherently strained, at room temperature ferromagnetic and smooth LSMO films lies in the engineering of the interface between the film and the substrate. It involves growing very high quality single crystal films. Tuning the growth temperature and post-annealing in oxygen helps to relax strain between the film and the substrate and improves the surface morphology [136]. Therefore, it is important to understand the microscopic processes and the corresponding deposition parameters that define the film growth [137].

It was shown that the growth temperature has a great influence on the diffusion barrier [137]. With increasing growth temperature, an exponential increase of diffusivity was observed, which affected the growth mode [137, 138, 139, 140]. At low growth temperatures the single layer terraces inherited from the STO substrate were still visible on the LSMO film surface. The RHEED pattern showed weak intensity contrast without extra diffraction spots. The film surface was poorly crystallized with 2D layer-by-layer features preserved. Upon increasing the substrate temperature the AFM image of the LSMO film surface did not show regular terraces or steps from the substrate and the roughness was increased. The RHEED displayed a weak diffraction pattern with extra spots, indicating 3D island formation. Further increase in substrate temperature indicated chemical phase separation resulting in different stoichiometry on different regions of the film surface [137].
With this knowledge, we studied the influence of heat current through the substrate holder (i. e. the growth temperature) on the magnetic properties and on the crystallinity of the LSMO films, while fixing the background oxygen pressure and the laser fluence in order to find the optimum growth temperature. 100 nm thick LSMO films were prepared by PLD. We would like to point out that there is a correlation between the heat current and the substrate temperature, thus we have specified the property which was really measured, the heat current, emphasizing that a higher heat current results in higher substrate temperature. The ZFC/FC magnetization curves of LSMO(100 nm)/STO heterostructures for three different heat currents were presented as a function of temperature on Figure 4. 5 a). T_C changes depending on the deposition temperature. The onset of the paramagnetic to ferromagnetic transition was $T_C = 320$ K for the film grown at $I_{fil} = 4$ A and reduced with decreasing growth temperature. Furthermore, the nature of the transition was broad, which was associated with the influence of a magnetic domain distribution in the film. Some of the domains contained higher strain related defects and the distorted MnO_6 octahedra resulting in reduced T_C, while domains containing lesser defects had a T_C close to the target material. We observed two prominent features in the data: A peak in the ZFC magnetization curves, T_{peak} and a splitting between the ZFC and FC curves below the irreversibility temperature T_{irr}. The FC and ZFC magnetization curves separated at around T = 90 K with M_{FC} non-equal to M_{ZFC} at T_{irr}. The low temperature deviation of the $M(T)$ curves was attributed to extrinsic effects such as strain and oxygen vacancies in LSMO [141]. These extrinsic effects promoted spin glass behavior in the film. The difference between the M_{FC}-M_{ZFC} at the temperature T_{irr} increased upon cooling. This was attributed to the presence of AFM-coupled Mn-Mn clusters at the interface region and a stronger coupling at low temperatures. However, as in the case of many other manganites, the charge ordering co-existed with ferromagnetism in the low temperature phase. Two characteristic temperatures (T_{peak} and T_{irr}) were very

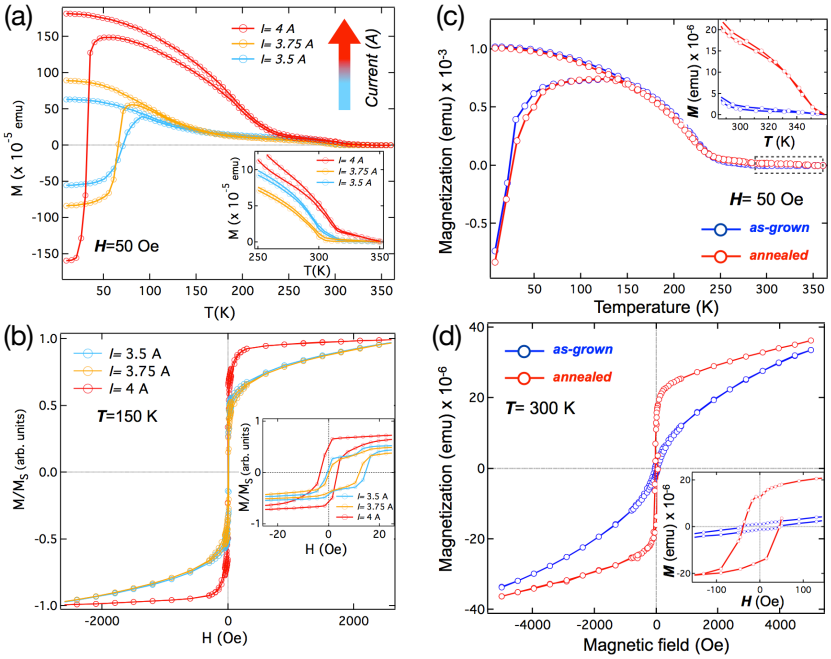

Figure 4.5: (a) and (b) Heat current dependent magnetic properties of LSMO/BTO hybrids. c) Effect of post-annealing on the $M(T)$ curves of 100 nm thick LSMO films. Measurements were performed under applied magnetic field of 50 Oe in [100] direction. Insets shows the enlarged $M(T)$ characteristics at high temperature regime for clarity. d) Effect of post-annealing on $M(H)$ of the same films. Inset shows the enlarged portion of the hysteresis loops around 0 Oe. Ferromagnetism sets in after *ex-situ* annealing.

close for samples grown at low substrate temperatures. T_{peak} differed from T_{irr} and reduced with increasing growth temperature, which was an indication of an AFM ordering or -more general- presence of a cluster spin glass system [136]. In Fig. 4. 5 b) the magnetization against magnetic field, $M(H)$ for the same samples was plotted. A characteristic shift of the $M(H)$ loops was evident for the LSMO grown at heater current of I = 3.5 A and I = 3.75 A. This shift was an indication of the well-known exchange bias (EB) effect in the LSMO film.

Focusing on the sample grown at I = 3.5 A, there was a complex M(H) curve: At H_{sat} = 3 kOe the magnetic moments of antiferromagnetic and ferromagnetic regions were oriented parallel. A sharp switching at low magnetic field of H = 12 Oe occured,

which was attributed to the switching of the ferromagnetic regions of the LSMO. The plateau in the $M(H)$ curve showed a gradual switching of the antiferromagnetic-LSMO magnetization due to the presence of spin clusters, which caused inhomogenous magnetic coupling. We also observed that the H_{EB} decreased with increasing growth temperature.

By tuning the growth temperature, varieties of surface morphology, surface crystallinity, and stoichiometry were observed [137]. The widely accepted equation of change in surface energy $\Delta\sigma$, is given as:

$$\Delta\sigma = \sigma_{substrate} + \sigma_{interface} - \sigma_{film}, \tag{4.1}$$

with $\sigma_{substrate}$ being the surface energy of the substrate, $\sigma_{interface}$ the film-substrate interface energy and σ_{film} the surface energy of the depositing layer. However, microscopic growth processes involve not only a balance of surface energy, but they consist of multiple steps. During PLD growth, a large atomic flux is generated. Incoming atoms become adatoms on the substrate surface and diffuse [137]. In reality, the growth is non-homogenous: Depending on the growth temperature various processes such as desorption, 2D island growth, 2D nucleation, 2D nucleation on 2D island growth and diffusion on 2D island growth can be observed, which might affect the crystallinty of the film. The maximum value of the nucleation rate $T_{nuc_{max}}$, is defined as:

$$T_{nuc_{max}} = H(\Delta\mu)/2k, \tag{4.2}$$

where k is the Boltzmann constant and $H(\Delta\mu)$ denotes the energy barrier of the nucleation[25] and is described as [137]:

$$H(\Delta\mu) = \frac{4\chi^2 s_c}{\Delta\mu - s_c\Delta\sigma} - (E_{des} - E_{sd}). \tag{4.3}$$

Here E_{des} and E_{sd} are the desorption and diffusion energy barriers, s_c is the area of the surface unit cell, χ is the step edge energy per unit length. $\Delta\mu$, defined as supersaturation, is the chemical potential difference of adatoms transitioning from their quasi-vapor phase near the substrate to their solid phase on the substrate [137]. At low substrate temperature, the nucleation rate decreases due to the high nucleation energy barrier. At the same time the deviation of the system from the equilibrium state, called as effective Zeldovich factor $f(\Delta\mu, T)$, which is given as the rate of atom exchange between the nuclei and its quasi-vapor parent phase, becomes high. Thus, the nucleation rate J_{nuc}, defined as in Eqn. 4. 4 is low and the film is not well-crystallized.

$$J_{nuc} = f(\Delta\mu, T)\exp\left(-\frac{H(\Delta\mu)}{kT}\right). \tag{4.4}$$

[25] At low laser repetition rate [142, 137].

An increase in the growth temperature drove the grains at the film surface to coalesce, improving the overall crystallinity of the film. We found that there was an indication of a decrease in roughness due to the diffusion of the grain boundaries. When the films were prepared at low substrate temperatures, the films exhibited a high non-uniform strain indicating a higher defect density. This can be attributed to the lower mobility of the adatoms on the growing film [143]. Additionally, at higher temperatures films could transport oxygen better through diffusion, enhancing the overall crystallographic order, but it did not reduce the overall strain. The literature on optimizing the magnetic and crystallographic properties of LSMO thin films shows a variety of approaches. As reported by Ref. [43], the amount of oxygen vacancies can be controlled by the oxygen pressure during LSMO growth. Furthermore, it has been shown by other groups that the oxygen content can be influenced by annealing. In Ref. [136] and in related references it has been observed that post-annealing in oxygen ambient pressure recovered the magnetic properties of LSMO/STO. This is a result of better oxygenation and minimized crystallographic defects. Thus, in order to improve the quality of the LSMO films, we annealed the samples *ex-situ* at T = 650°C in flowing oxygen under atmospheric pressure for an hour. Fig. 4. 5 c) depicts the effect of post-annealing on the temperature-dependent magnetization curves of (100 nm)LSMO/STO heterostructures and Fig. 4. 5 d) represents hysteresis loops of the same films. The inset shows the enlarged portion of the hysteresis loops around 0 Oe. As presented in Fig. 4. 5 c), the oxygen annealing significantly enhanced the ordering temperature, while there was hardly any change in the shape of the ZFC-FC magnetization curves. In agreement with the $M(T)$ curves, ferromagnetic ordering set in after *ex-situ* post-annealing. As shown in Fig. 4. 5 d) large hysteresis corresponding to ferromagnetism was observed. The coercive field of the film was 40 Oe, which was factor four larger than the reported value (10 Oe [144]) of LSMO thin films with similar thickness. We assumed that the crystal anisotropy became dominant upon annealing. Hence the coercive field of the LSMO films increased after annealing.

Furthermore, it is well known that the ferromagnetic order in the LSMO is dominated by the double exchange interaction between Mn^{4+} and Mn^{3+} ions. The improved magnetic properties after annealing could be attributed to the increment in the Mn^{4+}/Mn^{3+} ratio in the LSMO films due to oxygen absorption and incorporation during annealing. This was consistent with the result reported previously [145].

Worledge *et al.* [146] have demonstrated that annealing of $La_{0.67}Ca_{0.33}MnO_3$ films in oxygen changes structural ordering only slightly, if the oxygen content of the film is stoichiometric. That is, perovskite manganites have a stable structure with the O-stoichiometric phase [147]. In LSMO, the Mn ion has two different valences: Mn^{3+} and Mn^{4+}, with the ionic radius of Mn^{3+} (0.07 nm) being much greater than that

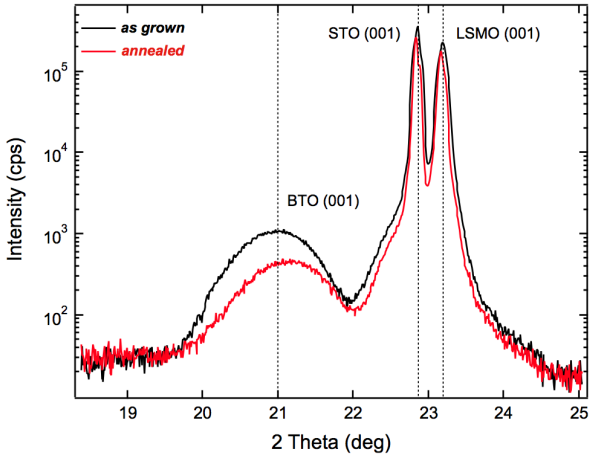

Figure 4.6: Comparison of XRD patterns between as-grown and annealed BTO/LSMO/STO hybrids. The presence of only (00l) peaks suggests that both the BTO and LSMO films are (00l) oriented in the growth direction in accordance with STO(001) substrate. XRD scans indicate no significant change in the out-of-plane lattice parameter between as-grown and annealed sample.

of Mn^{4+} (0.05 nm) [128]. If the film is non-stoichiometric, the Mn^{4+}/Mn^{3+} ratio diverges from the ideal value causing a reduced ferromagnetic order [148]. Fig. 4. 6 shows the comparison of XRD patterns between the as-grown and annealed LSMO films with BTO capping. Only (00l) peaks were found in accordance with the STO(001) substrate suggesting that both the BTO and LSMO films were (00l) oriented in the growth direction. XRD scans indicated no significant change in the out-of-plane lattice parameter of LSMO. The diffraction peak of the LSMO film was only slightly shifted from the bulk. This was attributed to the mismatch between the LSMO film and the substrate. The LSMO film had an out-of-plane lattice constant, $a_{LSMO} = 0.382$ Å.
The Full Width at Half Maximum (FWHM) LSMO peak was somewhat broadened compared to the substrate peak, which was an indication of slightly varying lattice parameters at different regions of the film or it could be also the variation of the lattice parameters along the depth axis [149]. After post-annealing the gravity center of the LSMO peak moved only slightly towards the left, which meant that the film only relaxed to a small extent. The peaks did not change drastically, thus there was no substantial relaxation. We concluded that the film was under tensile stress and the energy for straining was lower than the energy for forming dislocations. The FWHM

of the LSMO film slightly reduced after *ex-situ* annealing. The result was attributed to the improved crystal structure of the annealed LSMO films. More oxygen vacancies due to the oxygen deficiency were considered to result in more structural defects in the as-grown LSMO films. Structural distortions caused strong pinning centers for magnetic domain movement, hence increased the coercivity.
We also performed AFM measurements on as-grown and on post-annealed samples (not shown here). The surface roughness and the morphology were almost unaffected upon annealing, which was comprehensible with the results of LSMO films grown by RF-Sputtering [150].

4.3 BTO/LSMO/STO(001)

In order to directly disentangle the mutual interaction between the electrical and the magnetic degrees of freedom in BTO/LSMO hybrids, we prepared samples for Hard X-Ray Photoemission Spectroscopy (HAXPES) measurements. Prior to HAXPES measurements the quantitative ferroelectric film properties were obtained by Piezo-Response Force Microscopy (PFM) analysis[26]. Results from AFM and PFM measurements on an as-grown BTO(5 nm)/LSMO(30 nm)/STO(001) heterosystem are depicted in Figure 4. 7. The Figure 4. 7 a) presents the topography image of the BTO film. The as-grown BTO film had a huge amount of particles on the surface. The PFM phase image (4. 7 b)) showed a contrast originating from P+ polarization written with a DC bias of 7 V and 8 V, marked as blue and red rectangles, respectively. For reading out the piezoresponse, a tip bias of $V_{tip} = 2$ V at $f = 25$ kHz was applied. However, the written polarization pattern decayed very quickly, e. g. within two hours (4. 7 c)). Figures 4. 7 d) and 4. 7 e) show the piezoresponse amplitude and piezoresponse phase diagrams versus applied bias, respectively. The piezoelectric strength obtained from the measurement amounted to 5 pm/V. Due to retention losses no hysteresis was observed. In order to check if the backswitching after poling was prompted by the high AC voltage used for PFM (between $2 - 3$ V), the DART[27] mode was used. For reading out the piezoresponse a tip bias of $V_{tip} = 1$ V at $f = 293$ kHz was applied. Unfortunately, the DART mode is very sensitive to crosstalk by topography, therefore the phase image was not clear. We wrote the polarization on different areas, however, the phase image showed no changes. We claimed that the BTO film had a degraded retention characteristics, which hindered the patterning. The retention loss was most probably generated by the leakage currents, which were caused by ion drift and carrier conduction induced by the depolarization field [151].
After the pre-characterization of the ferroelectric quality, we have performed HAXPES

[26] Measurements were performed by Dr. Alessio Morelli at MPI-Halle.
[27] Dual-Amplitude-Resonance-Tracking

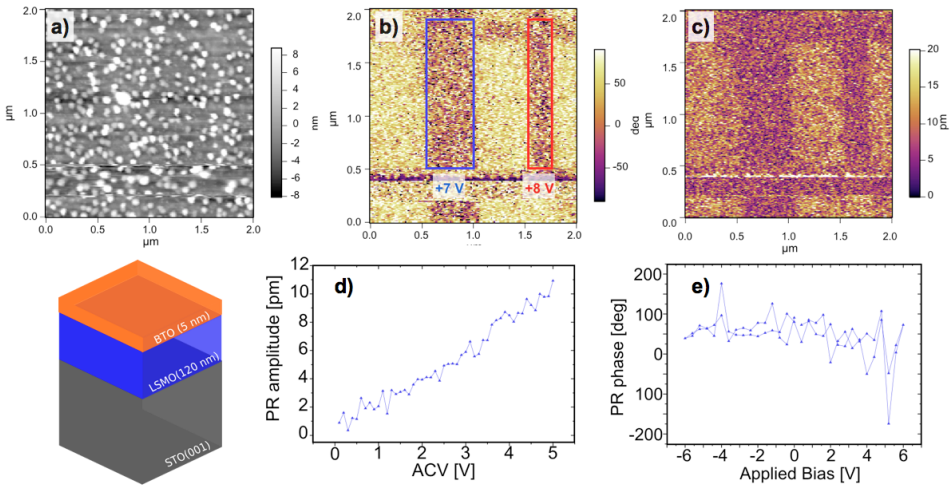

Figure 4.7: a) Topography image of the as-grown BTO(5 nm)/LSMO(30 nm)/STO(001) heterosystem. b) PFM phase image of the sample showing contrast originating from P+ polarizations written with 7 V and 8 V. Right after switching one can detect phase signal (see b)), but it is disappearing very fast, e. g. within two hours (c). d) and e) show the piezoresponse amplitude and piezoresponse phase diagrams vs. applied bias, respectively. The piezoelectricity strength obtained from the measurement amounts to 5 pm/V.

measurements. High photon excitation energy produces photoelectrons of high kinetic energy allowing one to measure buried layers and interfaces due to the high inelastic mean free path of those electrons. In addition, circular light polarization allows for magnetic circular dichroism in angular distribution (MCDAD), yielding information about the magnetic state of a layer.

The samples were grown by PLD on STO substrates as explained in the beginning of this chapter. For the HAXPES measurements, the samples consisting of a 3 nm Pd electrode, a ferroelectric BTO layer of 7 nm thickness followed by a 30 nm thick LSMO bottom layer were grown on a conductive $Nb:SrTiO_3(001)$ substrate. We increased the thickness of the BTO film from 5 nm to 7 nm in order to exclude the possible oxygen vacancies, which could destroy the ferroelectric polarization. The crystal phases and the surface topography of the samples were characterized by XRD and AFM, respectively. SQUID measurements ensured that the LSMO was ferromagnetic at RT. To achieve a higher magnetic signal an in-plane magnetic field was applied and the samples were cooled down to 75 K. The ferroelectric top layer was poled under electrode arrays

larger than the beam footprint on the sample. We wrote three different ferroelectric states: up- and down-polarized, and neutral depolarized. The sample geometry is presented in the Fig. 4. 8 b).

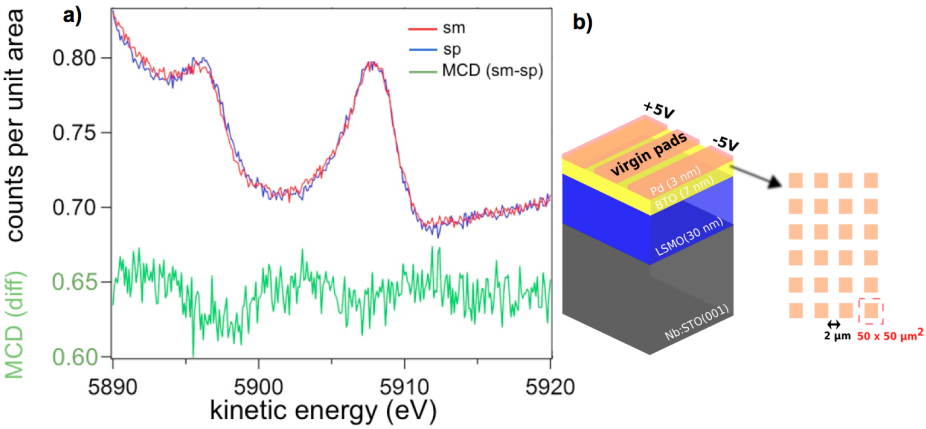

Figure 4.8: Mn 2p HAXPES-MCD of a Pd(3 nm)/BTO(7 nm)/LSMO(30 nm) microcapacitor array at T = 80 K in remanent magnetization. The buried layer shows a Mn 2p spectrum and MCD. Measurements are carried out using hard x-rays of 6500 eV at beamline P09 of the PETRA-III synchrotron (HASYLAB,Hamburg).

The electrical characterization and polarization measurement of the BTO microcapacitors was performed using an Agilent B 1500A semiconductor analyzer in a two probe measurement scheme, with the switching voltage applied to the Pd top electrode and the substrate grounded. These areas were investigated independently by HAXPES. Measurements were carried out using hard x-rays of 6500 eV at beamline P09 of the PETRA III synchrotron (DESY,Hamburg,Germany), using a Si (111) double crystal monochromator (DCM). The pass energy of the analyzer was set to $E_{pass} = 100$ eV. The resolution of the analyser was 322 meV and the beamline resolution was 700 meV. The angle between the photoelectron-analyzer and the beamline was 90°. We operated close to normal emission (ca. 7° off) to maximize the information depth and to reduce the surface layer contributions. The electrode size and separation in each array were 50 x 50 m^2 with 2 μm separation. We expected to see:

- a polarity-induced shift in the peak positions of the ferroelectric film.
- a change in the magnetic structure and hence the size of the magnetic dichroism in the ferromagnetic layer.

These results were of very high relevance for answering which electronic states participate in the magnetoelectric interaction, and if a change from ferromagnetic to antiferromagnetic structure happened at the BTO/LSMO interface. By this knowledge, it would become possible to optimize the magnetoelectric devices. Fig. 4. 8 shows the results from photoemission experiments on multiferroic Pd(3 nm)/BTO(7 nm)/LSMO(30 nm) microcapacitors using hard x-rays. We measured the Mn 2p peaks of the buried LSMO layer. The statistics were not very good. Though the layer exhibited a small MCD signal, which was strongest at the Mn $2p_{1/2}$ edge.
Next, we performed HAXPES measurements on a 7 nm thick LSMO reference layer grown on a BTO(001) single crystal. The measurements were carried out using hard x-rays of 6000 eV at beamline P09 of the PETRA III synchrotron (HASYLAB), using a Si (311) DCM. The pass energy of the analyzer was set to $E_{pass} = 40$ eV. The resolution of the analyser was 200 meV. The optical axis of the photoelectron analyzer was positioned close to the surface normal (ca. 7° to the x-rays). The result is presented in Fig. 4. 9. We observed a strong dichroism (25 %) at the Mn $2p_{3/2}$ peak in the MCD signal from the non-buried reference layer. We considered that the reversed signal in the microcapacitor sample could be due to a modified electronic structure near the BTO/LSMO interface. The reference sample yielded mainly information about the LSMO bulk.

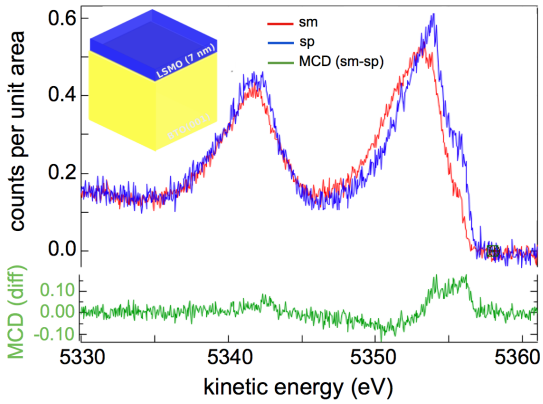

Figure 4.9: Mn 2p HAXPES MCD of a LSMO(7 nm)/BTO(001) reference sample. Measurements are carried out using hard x-rays of 6000 eV at beamline P09 of the PETRA III synchrotron (HASYLAB,Hamburg).

To overcome the leakage current problem occured in thin BTO films (< 10 nm), we prepared bulk-like BTO films to ensure a low defect density and a high polarization

normal to the sample plane [122]. A 150 nm thick BTO film was fabricated by PLD onto an LSMO/STO(001) film as a back electrode for PFM and for absorption measurements. A JSPM 4210 (Jeol) microscope located in the department of PGI − 7 at FZ Jülich was used for the AFM and PFM measurements [28]. The PFM measurements of the out-of-plane polarization were carried out with conductive Si cantilevers having a spring constant of 40 N/m, which are stiff enough to reduce the influence of non-local electrostatic effects causing cantilever buckling oscillations [151]. The local polarization reversal of the as-deposited BTO films was performed by applying a DC voltage of ±8 V on the tip. To read the piezoresponse an AC peak-to-peak voltage of 3 V was applied on the tip, with the lock-in frequency of 6 kHz. X-PEEM measurements were performed at the LEEM-PEEM, which is located as an endstation at UE56/1-SGM beamline of BESSY-II, Berlin.

Figure 4. 10 a)-c) depicts the topography, out-of-plane and in-plane piezoresponse images, respectively. In Fig. 4. 10 b), the outer square of 8 x 8 μm^2 was written by a negative bias of −8 V creating a positive image charge below the surface and thus a P^+ state (outward directed polarization). The polarity of an inner 4 x 4 μm^2 square was reversed by a 8 V bias (P^-). In general, after poling along the z-direction, one should not observe in-plane piezo-response, however, we detected an in-plane piezoresponse. We claimed that the as-grown BTO had a canted polarization. We determined the local conductivity of the BTO surface by using the LC-AFM option of the set-up. The local current at different points on the sample was on the order of 10^{-13} A, which was an expected result for a bulk-like BTO film.

Misfit dislocations occur due to a difference in the lattice parameters of the film and the substrate [152]. The stability of ferroelectric polarization increased with increasing film thickness. The results suggested that increasing the thickness up to 150 nm reduced the oxygen deficiencies, that hindered leakage currents.

In order to check the possible electronic structure changes in BTO upon pattern polarization, we performed X-PEEM measurements. During XPEEM experiments, spatially-resolved images of the sample surface were recorded for different photon energies. Room temperature ferroelectricity of BTO is due to a reduction of octahedral symmetry (O_h) around the Ti^{4+} ion to a C_4 symmetry [73]. This symmetry reduction is associated with a relative displacement of the Ti ions from their centrosymmetric position in the tetragonal unit cell along the *c*-axis, which is related to a considerable charge rearrangement. Lower than a cubic symmetry in the ferroelectric phase lifts the degeneracy within the t_{2g} and e_g orbitals. Yet, this additional energy splitting is modest and not directly visible in the x-ray absorption spectrum in the case of BTO. It can, however, be resolved by measuring the dichroism between two different directions of linear polarizations [89]. Figure 4. 10 d) presents the XAS data extracted from the regions of interest as marked

[28] Measurements are performed by Prof. Dr. K. Szot

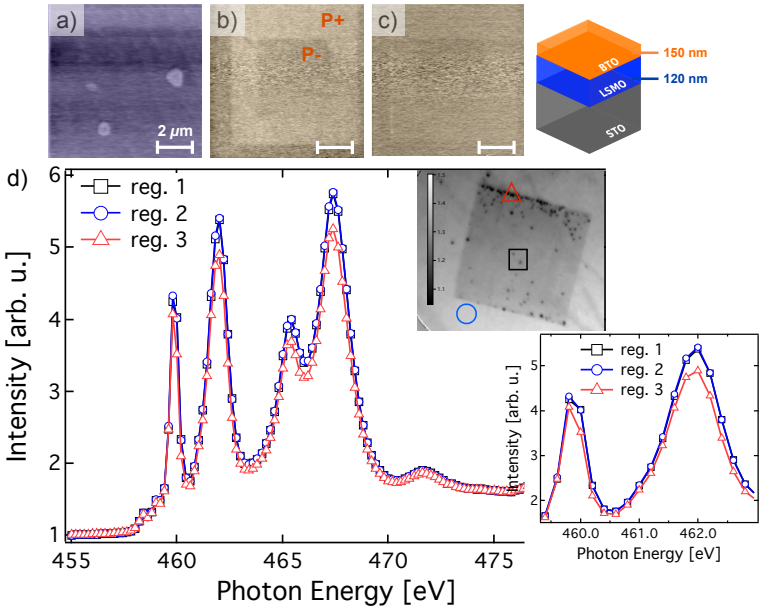

Figure 4.10: a)-c) depicts the topography, out-of-plane and in-plane piezoresponse images of a 150 nm thick BTO film, respectively. The outer square of 8 x 8 μm^2 was written by a bias of -8 V creating a positive image charge below the surface and thus a P^+ state (outward directed polarization). The polarity of the inner 4 x 4 μm^2 square was reversed by a 8 V bias (P^-). d) presents the XAS data at the Ti edge extracted from the regions of interest as marked in the inset, which was taken at a photon energy of 462 eV with a 20 μm field-of-view (FOV) using soft x-rays.

in the inset of Fig. 4. 10 d). The inset image was taken at a photon energy of 462 eV with a 20 μm of field-of-view (FOV). The three levels of intensity at a given energy were marked. As presented in the upper panel of Fig. 4. 10 d), the measured spectra closely resembled the spectra for a Ti ion in an octahedral coordination[153]. The four well-split peaks represented the characteristic structure of a Ti^{4+} $2p^63d^0$ to $2p^53d^1$ absorption process. Due to 2p spin-orbit splitting they were divided into two sets of peaks forming the L_3 and L_2 absorption edges. Each edge's main feature was the presence of two peaks directly related to t_{2g} and e_g orbital splittings in perfect O_h symmetry, and determined by the strength of the crystal field, *i. e.* the electrostatic potential, U due to oxygen ligands acting on 3d orbitals [154, 155].
Pattern polarization and subsequent ferrolectric signal detection proved that BTO was

ferroelectric. However, it was observed that the ferroelectric polarization disappeared in X-PEEM experiments performed one day after the PFM experiments. During depolarization of the PFM patterned regions, the BTO film homogeneity was disrupted and local Ti- and O-rich (on the corners of the pattern) regions in the film were formed. Although there was a slight difference in the intensity of the PEEM image, we did not see a clear difference in the Ti spectra between the written (open square) and the virgin regions (open circles) in X-PEEM. The following comments might be deduced for these results:

- This might be a pre-finished phenomenon and we might have taken a picture of it.
- The photon-generated carriers during XPEEM measurements destroyed the pattern polarization.

4.4 Effect of oxygen pressure of BTO growth on BTO/LSMO/STO(001)

Oxygen vacancies in complex oxides constitute one of the most important defects [73]. Oxygen vacancies are easily accessible to materials engineering due to the convenient possibility to control oxygen pressure and reactivity during and after growth [73]. Specifically for ferroelectrics, oxygen vacancies can have detrimental effects, such as increasing leakiness and destroying the ferroelectric retention [151, 73]. It is important to improve our knowledge of the interfacial phenomena in all-oxide hybrids and to elucidate the microscopic processes related to oxygen vacancies [73]. In a comprehensive study, Aruta *et al.* [43] showed that the orbital ordering in LSMO thin films can be manipulated via the oxygen partial pressure during LSMO growth. In an oxide heterostructure, to grow the top layer often involves different temperature and pressure conditions, which may subsequently alter the interfacial region in the bottom layer, even if the bulk part of the bottom layer remains unchanged [73].
We studied the interface between LSMO and BTO. The focus of the work was on the changes of the interfacial electronic structure and the orbital ordering in LSMO, which have been introduced by growing the BTO top layer under different oxygen partial pressures. In order to extract the desired information from such an interface region we have performed XAS measurements [73]. BTO/LSMO layered heterostructures were prepared via PLD. First, a 120 nm thick ferromagnetic LSMO film was grown on TiO_2-terminated STO, followed by the deposition of a 5nm thick ferroelectric BTO film as described in [92]. For the LSMO growth, an oxygen pressure of $1x10^{-2}$ mbar was found to be the optimal growth parameters and therefore kept constant for the LSMO deposition in all BTO/LSMO heterosystem presented here. The oxygen pressure during

BTO growth was varied from 3x10^{-3} mbar to 1x10^{-2} mbar. In sample A, BTO was grown at 3x10^{-3} mbar oxygen pressure (low oxygen pressure), whereas in sample D BTO is grown at 1x10^{-2} mbar oxygen pressure (high oxygen pressure) [73]. We note that all measurements were performed without any post-annealing procedure in the present work.

First, room temperature XRD measurements were performed in order to probe the crystallinity of the films. The crystal structure of bulk BTO in the ferroelectric phase is tetragonal with the in-plane and out-of-plane lattice constants, a = 3.994 Å and c = 4.0335 Å, respectively as measured experimentally in Ref.[156]. The crystal structure of bulk LSMO is rhombohedral with a pseudocubic lattice parameter of a = 3.87 Å[43]. XRD measurements confirmed the high crystalline quality. The analysis supported the (00l) orientation of the LSMO and BTO films [73]. The spacing between diffracting planes, d was determined by Bragg's law (see Equation 4. 5.).

$$2dsin\theta = n\lambda \tag{4.5}$$

here θ is the incident angle, n is an integer, and λ is the wavelength of the beam. It must be also noted that d is calculated based on the cubic symmetry, i. e. as if $a = c$ in the ferroelectric phase:

$$\frac{1}{d^2} = \frac{h^2 + k^2 + l^2}{a^2} \tag{4.6}$$

with h, k, l being the Miller indices. Figure 4. 11 shows the relation between the out-of-plane lattice constants, $d_\perp$ of BTO and LSMO films as a function of BTO-growth oxygen pressure. The out-of-plane lattice constant, $d_\perp$ of the BTO thin film grown under low oxygen pressure (Sample A) was calculated from the XRD data amounted to 4.25 Å, confirming that the BTO film grown on the LSMO/STO system was under in-plane compressive strain compared to bulk BTO. Moreover, the $d_\perp$ of the unit cell of BTO reduced from 4.25 Å to 4.18 Å as the oxygen pressure during BTO growth increased from 3x10^{-3} mbar to 1x10^{-2} mbar, which corresponded to a reduction in compressive strain by 2 % [73]. Besides, increasing the oxygen pressure has broadened the BTO(00l) reflections, which was attributed to a smaller crystallite size and to an increase of the non-uniform strain [73].

The $d_\perp$ of LSMO thin film grown under low oxygen pressure of BTO growth (Sample A) was calculated as 3.843 Å. This implied that the LSMO film grown on STO(001) was under tensile strain [73]. The Fig. 4. 11 showed that the $d_\perp$ of LSMO only marginally increased with increasing oxygen pressure of the BTO growth [73]. This small expansion of the c-axis lattice parameter was an unexpected result, since in an oxygen-rich film the number of Mn^{3+} ions should have reduced [43, 73]. Additionally, upon increasing the oxygen pressure the width of the LSMO(00l) reflections became narrower, which was a sign of better crystallographic quality, e .g. reduction of the non-uniform strain.

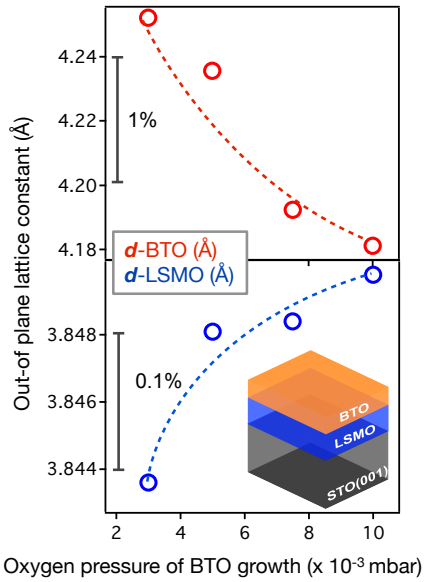

Figure 4.11: The relation between the measured out-of-plane lattice constants, $d_{\perp}$ of BTO and LSMO films in BTO(5 nm)/LSMO(120 nm)/STO(001) heterosystems as a function of oxygen pressure. Lattice constants are calculated by Bragg's law using respective (001) reflections. Dotted lines serve as guides to the eye.

Simultaneously, AFM investigations of the films (not shown here) exhibited clear terraces with a width of ca. 1 μm and a height of one unit cell (step-flow growth regime). All films were smooth with a root-mean-square (rms) roughness around 0.5 nm. The information gained by the RMS roughness analysis on STO substrates have suggested that the surface roughness of STO substrates was not significantly different from each other, which allowed us to relate the observed roughness of BTO/LSMO/STO contacts with different oxygen pressure of BTO growth directly to the changes in the oxygen pressure. The sample grown at high oxygen pressure (Sample D) still displayed indications of step-flow growth, however the sample surface was more grainy with the islands formation easily observable. We have expected to see a clearly less porous film due to higher oxygen pressure during growth (Sample D), as was seen in the reduction of the out-of-plane lattice parameter. The BTO film became denser due to better oxygenation, which resulted in better growth. We claimed that the film was more ferroelectric [157] (see Fig. 4.13)

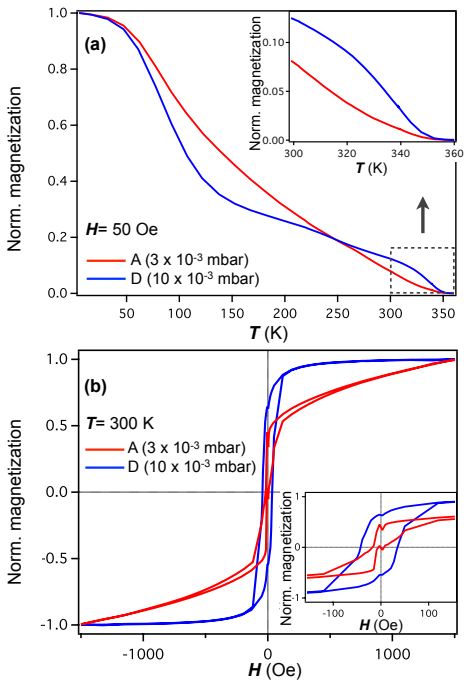

Figure 4.12: (a) Temperature dependence of normalized magnetization curves of BTO(5 nm)/LSMO(120 nm)/STO(001) taken in the field-cooling condition. The LSMO films A and D are shown. (b) Hysteresis loops of the LSMO films.

Next, the magnetic properties of the LSMO films were determined. Fig. 4. 12 a) shows the temperature dependent magnetization curves taken in the field-cooling condition. The inset shows the enlarged $M(T)$ characteristics at the high temperature regime for clarity. The magnetization M was normalized to its value M_0 at T = 8 K. The $M(T)$ data diverged from a standard magnetization curve of stoichiometric LSMO films [73]. Sample A showed a gradual increase in magnetization with decreasing temperature. Due to the coexistence of two magnetic phases sample D showed two transitions [73]. Sample D had a T_C around 350 K, whereas the T_C of sample A was slightly lower than 300 K. The reduced T_C of sample A was attributed to the magnetic inhomogeneties in the film.

Oxygen vacancies reduce the valency of the transition metal ion, here Mn ions. The overlayer BTO was grown under low oxygen pressure, thus there might be regions in

the LSMO film, which were separated by high Mn^{3+} containing non-magnetic clusters as found in references [40, 73]. The local Jahn-Teller distortion around the Mn^{3+} ion is followed by the localization of the electrons, which caused a reduced T_C. We tentatively assumed this model and discussed it in the context of the Mn $L_{3,2}$ absorption spectra [73].

Fig. 4. 12 b) presents the $M(H)$ loops of the same films taken at room temperature. The inset shows the enlarged $M(H)$ curves in a narrow range around zero applied field. The magnetization of the sample A increased linearly with increasing magnetic field. This could be attributed to an existence of an antiferromagnetically ordered phase in the film [158] or - more general - a field induced change of spin canting angle [159]. Upon increasing the oxygen pressure the remanent magnetization M_R/M_S increased, which was a common ferromagnetic behavior [73]. The observed room temperature ferromagnetic behavior in sample D was mimicking the ideal case, i. e. the presence of a double exchange mechanism [73].

Magnetic measurements showed that an overlayer of BTO shifted the magnetic transition temperature towards room temperature. However, the ferromagnetism diminished at room temperature indicating an existence of magnetic inhomogenities, if the LSMO films were not saturated by oxygen during the BTO growth [73].

To investigate whether regions with different magnetic phases were present within the XAS probing depth, we carried out XAS measurements at Ti (2p) and Mn (2p) $L_{3,2}$ edges with s- and p-polarized x-rays. Fig. 4. 13 shows the XAS of BTO/LSMO/STO heterosystems taken with s-polarized x-rays at the Ti $L_{3,2}$ absorption edge as a function of oxygen pressure during BTO growth. In the lower panel the XLD signals of the same samples were reproduced. The anisotropy of the orbitals provided the opportunity to study the charge anisotropy, and thus ferroelectricity [73]. We observed a considerable XLD in both samples. The difference spectrum was similar in shape independent of the oxygen pressure during BTO growth [73]. Both spectra nearly resembled the spectra for a Ti ion in an octahedral coordination[153]. The L_3 absorption edge zoom inset for BTO grown under high oxygen pressure (sample D) in Fig. 4. 13 illustrated the definition of the corresponding crystal field energy.

In order to estimate the crystal field energy, the L_3-t_{2g} and the L_3-e_g absorption edges were fitted by a combination of Lorentzian and Gaussian functions, respectively. We calculated $E_{t_{2g}} - E_{e_g} = 2.07 \pm 0.02$ eV. The crystal field energy was surprisingly independent from the oxygen pressure [73]. This supported the interpretation that the overlap between the Ti 3d and the O 2p orbitals was not related to the oxygen pressure of BTO growth and that low oxygen pressure rather introduced oxygen vacancies in the film leading to a broadening of the peaks [73]. The low energy side of the L_3 e_g peak of sample D appears slightly broader than sample A and higher in magnitude. This was

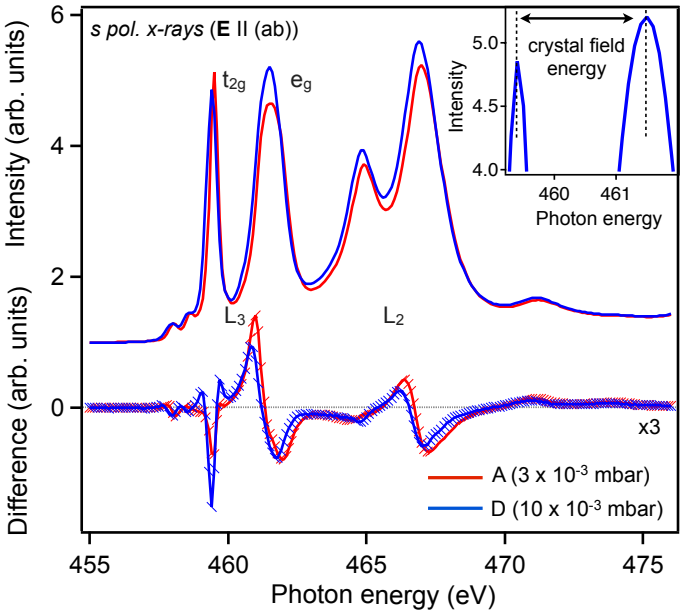

Figure 4.13: XAS of BTO(5 nm)/LSMO(120 nm)/STO(001) taken with s-polarized x-rays at Ti $L_{3,2}$ edge as a function of oxygen pressure during BTO growth. Lower panel: XLD of the same heterostructures. Inset: Magnification of the Ti L_3 edge of sample D showing the definition of the crystal field splitting.

an another prominent effect of oxygen pressure on the BTO growth on the Ti multiplets [73]. We fitted the e_g peaks to the Gaussian function and calculate the FWHM from the equation, because e_g states are more sensitive than t_{2g} states. The fit of the L_3 e_g peak for the BTO film grown under low oxygen pressure ($FWHM_A = 0.85$ eV) yielded a slightly larger value than the BTO film grown under high oxygen pressure ($FWHM_D = 0.78$ eV). This was designed such that the Ti ions in sample A sustained a more tetragonal symmetry than in sample D.

In a complementary study, we have performed XPS using hard x-rays of 4000 eV on the same samples. The Ti 2p core level electrons exhibited a shift towards higher electron binding energy with increasing oxygen pressure (see Fig. 4. 14). This indicated a lower oxidation state of the Ti atoms for the sample grown at low oxygen pressure. According to the XRD results the distortion along the z-axis reduced with increasing oxygen pressure. Therefore, both XAS and XPS data well supported the XRD findings

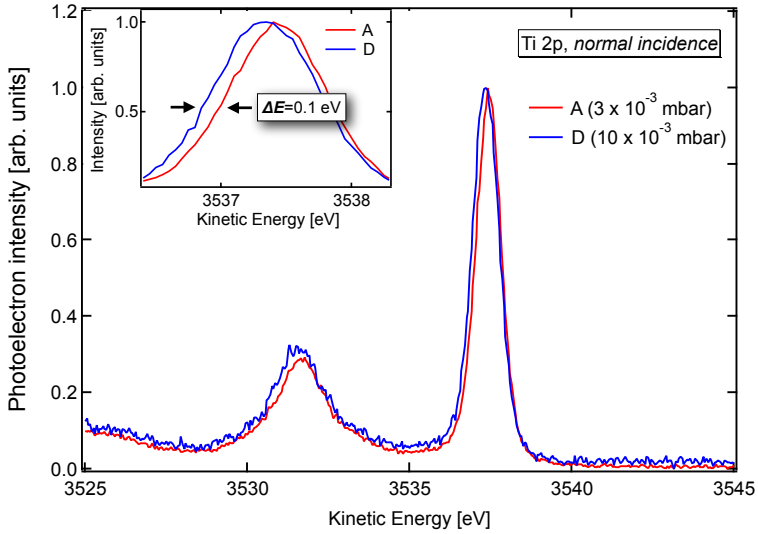

Figure 4.14: Hard x-ray photoemission of BTO(5 nm)/LSMO(120 nm)/STO(001) as a function of oxygen pressure during BTO growth. Inset shows the magnification of the shift towards lower kinetic energy of photoelectons with increasing oxygen pressure.

[73].

To emphasize the changes in the BTO/LSMO interface emerging with the BTO growth under different oxygen pressure, we have performed XAS experiments at the Mn $L_{3,2}$ edges. Fig. 4. 15 depicts the polarization dependent Mn $L_{3,2}$ XAS characteristics of BTO/-LSMO/STO at two different values of oxygen pressure during BTO growth. The lower panel of the Fig. 4. 15 shows the corresponding XLD spectrum. We assigned the peak at 641.6 eV as Mn^{3+} contribution in both films analogously with Ref.[43]. Usually most of the Mn^{4+} ions are substituted by Mn^{3+} ions only in oxygen deficient films [73]. Further analysis showed that the amount of Mn^{3+} ions was higher in sample A than in sample D.

In the last step, we have addressed the polarization dependent XAS of individual LSMO films. The intensity of the XAS of sample D taken with p-polarized x-rays was larger than the intensity of the XAS taken with s-polarized x-rays meaning more free states were present in the direction of the electric field vector parallel to the c-axis [73]. The electrons had an in-plane e_g orbital ordering in agreement with the previous observations[43, 73]. According to the Goodenough-Kanamori rules this statement also supported the observed higher ferromagnetic in-plane interaction in sample D[160]. On

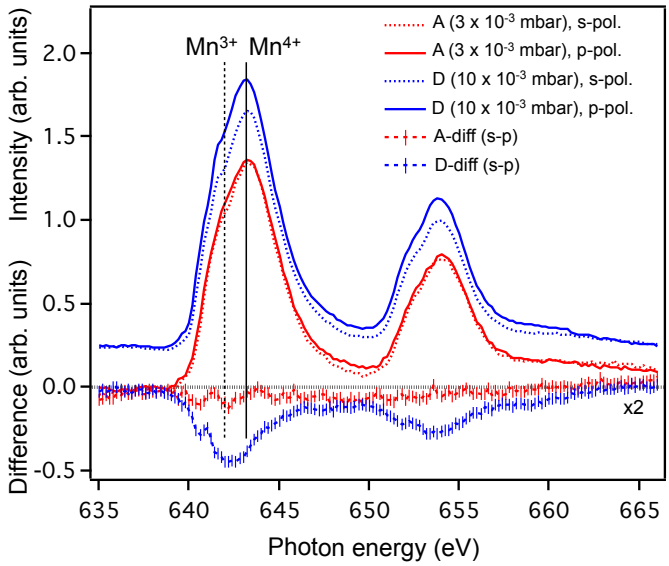

Figure 4.15: Upper panel: XAS characteristics of BTO(5 nm)/LSMO(120 nm)/STO(001) taken with **E**‖ab (s-pol.) and **E**‖c (p-pol.) x-ray polarizations at Mn $L_{3,2}$ edges as a function of oxygen pressure during BTO growth, offset for clarity. Energies of the most prominent peak of the 3+/4+ multiplets are marked. Lower panel: Measured linear dichroism, LD=I‖ab − I‖c, of the same heterostructures.

the basis of magnetic and structural data we claimed that increasing oxygen pressure during overlayer BTO growth maintained the bulk-like stoichiometry at the interface between LSMO and BTO. The prerequisite for ferromagnetic ordering in stoichiometric LSMO was the presence of Mn^{3+}/Mn^{4+} mixed valency. Sample D showed a ferromagnetic ordering at room temperature, which was a direct indication of the preserved stoichiometry [73]. Furthermore, considering the fact that the Mn^{3+} ion was a JT active ion and the film possessed an in-plane strain and was under uniform distortion, there would be a preferential orbital ordering[73].

The absence of a clear linear dichroism in sample A supported the magnetic measurements. Oxygen vacancies induced by low oxygen pressure during BTO growth increased the average of Mn ions with Mn^{3+} contribution. In the case of static JT distortion the $Mn^{3+} - O^{2-} - Mn^{3+}$ interaction favors antiferromagentic configuration. However, sample A did not show an XLD, suggesting that there were magnetic inhomogeneities and/or spin clusters at the BTO/LSMO interface [73]. The $M(H)$ data

verified the existence of a sizable exchange bias in sample A. Ferromagnetic properties of thin manganite films might have reduced at the (001)- interface or surface. LSMO is a polar and STO is non-polar oxide. STO has a cubic and bulk LSMO has a rhombohedral crystal structure. LSMO films grown on STO forms an orthorhombic phase to hold strain. Along with that there is a charge redistribution at the interface due to polar discontinuity and orbital ordering generated by the strain and/or broken symmetry [144]. Since sample A did not show any sizable XLD, we assumed that due to inhomogeneities during deposition, LSMO/STO of sample A formed different phases along with the orthorhombic phases.

In conclusion, first we prepared LSMO films by pulsed laser deposition on the lowest lattice mismatched STO single crystals. Varying different PLD parameters, we studied their surface morphology, structural, magnetic and electronic structure properties in detail.

From the XRD and AFM results, we claimed that an increase in the growth temperature caused the grains at the film surface to coalesce, improving the overall crystallinity of the film. There was an evidence of roughness reduction due to larger grain size. When the films were prepared at low substrate temperatures, the films exhibited a high non-uniform strain indicating a higher defect density. This was attributed to the lower mobility of the adatoms on the growing film [143]. Furthermore, at higher temperatures films transport oxygen better through diffusion, enhancing the overall crystallographic order (reduced crystallographic defects), but it does not reduced overall strain. Lower film growth rate and higher film thickness caused polycrystallinity and development of grain boundaries. With increasing defect and grain boundary concentration, the low field magnetoresistance and dielectric constant of the film increased significantly in agreement with [11].

Second, we prepared BTO/LSMO hybrids in order to manipulate the strain state of the magnetic film LSMO via BTO, because in such heterostructures physical properties are most commonly coupled via mechanical stress. PFM investigations on very thin BTO layers did not show any change in the phase image after poling the sample. We concluded that the thin BTO films had a degraded retention characteristics, which have hindered charge polarization. This result was in good agreement with other studies reporting that the retention loss is mainly generated by the leakage currents [151]. Increasing the thickness of the BTO film reduced the leakage currents and made patterning possible. On the contrary, it prohibited us to study the interface between LSMO and BTO, which laid at the heart of the research of this thesis.

Last, we demonstrated a way to modify orbital ordering in LSMO thin films. We showed that it was possible to influence the electronic and structural properties of LSMO films fabricated under same conditions only by tuning the oxygen pressure during the growth of an overlayer oxide BTO. Our systematic characterization confirmed

that with increasing oxygen pressure existing stoichiometry variations in LSMO films between the bulk and near interface could be minimized. Increasing oxygen pressure of BTO growth induced a reduction in the non-uniform strain in the LSMO and kept the film ferromagnetic at room temperature. We showed that high oxygen pressure led to in-plane ordering (Sample D), while low oxygen pressure resulted in an orbital non-ordered state (Sample A).

Chapter 5

Metal/Oxide Artificial Multiferroics:Fe/BTO(001)

This chapter focuses on:

- the brief introduction to the state-of-the-art research,
- characterization of BTO(001) single crystal surfaces mainly via LEEM and XPEEM methods,
- *in situ* growth properties of Fe films on $BaTiO_3$, and
- the effects of Fe deposition control parameters on the microscopic properties of ferromagnetic domain configuration.

5.1 BTO(001) Surfaces

5.1.1 BTO(001) Single Crystal Cleaning

$BaTiO_3$(001) (BTO) single crystals (SC) were supplied from the company SurfaceNet. SC were one-side polished, 6 x 6 mm^2 big and 0.5 mm thick. Prior to the experiments, the as-received BTO SC were cleaned *ex situ* via ultraviolet-ozone ($UV - O_3$) treatment to eliminate the surface carbon contamination. Organic compounds are transformed into unstable substances such as water, carbon dioxide and nitrogen by dissociation by ultraviolet rays and by strong oxidation during the formation and decomposition of O_3, and are removed from the contaminated surface. Immediately after the $UV - O_3$ treatment, the clean BTO SC were introduced into the load-lock. The SC were transferred to the prep-chamber, where they were annealed *in situ* at T = 600°C in oxygen

atmosphere of 4 x 10^{-6} mbar for an hour to obtain a clean reconstructed surface reconstruction. Subsequently, to remove residual contamination such as H_2O and CO_2 and to create sufficient oxygen vacancies for electrical conductivity, the crystals were annealed at T = 700°C with a base pressure of 8 x 10^{-10} mbar for two hours. Auger electron spectroscopy (AES) is a method to analyze the chemical composition of the surface layers of the sample, i. e. cleanliness of the surface [104]. Figure 5. 1 (a) presents the Auger spectrum of a clean BTO SC surface after subsequent *in situ* annealing cycles. AES revealed a negligible carbon contamination on the surface within the AES detection limit, which might have originated from the contaminants on the surface and/or in the vacuum chamber. In order to control the crystalline order of BTO surface the low-energy-electron-diffraction (LEED) mode of PEEM was utilized. The representative LEED pattern in Fig. 5. 1 (b) taken at E = 26 eV showed a well-ordered (2x2) reconstruction and a homogeneously BaO-terminated crystal surface at room temperature.

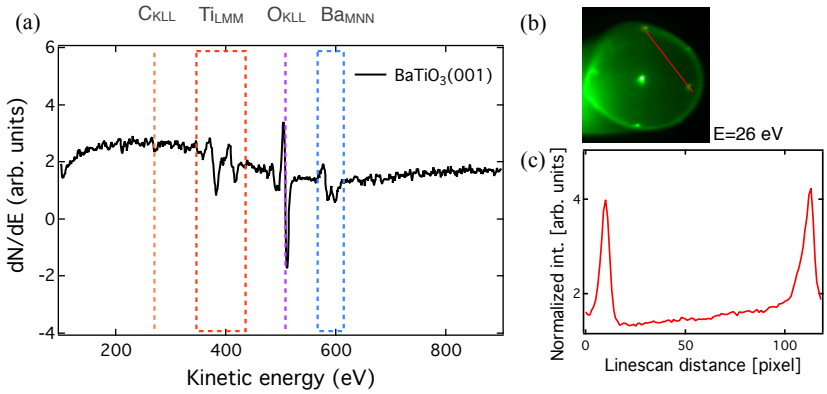

Figure 5.1: Auger spectra from a clean $BaTiO_3$ single crystal after *in-situ* annealing cycles. Negligible contamination on the surface within the AES detection limit. (b) LEED pattern of the BTO(001) taken with the LEEM with primary energy of 26 eV. (c) Linescan over the diffraction spots.

The sharp diffraction spots indicated a high quality long-range order of the BTO(001) surface structure. Due to surface preparation by high temperature UHV annealing we created oxygen vacancies, leaving the surface reduced, while some of them were compensated by the annealing in the oxygen atmosphere [21]. The (2x2) surface reconstruction referred either to a relaxation, to a rearrangement, or to oxygen vacancies

[21]. With the absence of oxygen atoms, the Ti atoms at the surface were rearranged. In case of oxygen vacancies, there must be a charge compensation on Ba and on Ti. For example, Ti would change to a 3+ state to compensate oxygen vacancies [21]. On these well-prepared single crystals, the deposition of thin iron films was performed as presented in the following sections. Furthermore, the reconstruction might also have a very limited influence on the deposited atom positions. According to the theoretical studies, upon Fe evaporation on BTO(001), the Fe atoms would occupy the on-top positions of oxygen atoms [22, 161]. With the missing oxygen lattice points, the first layer of Fe might form voids at those positions, which are compensated with the successive Fe layers [21].

5.1.2 *In-situ* LEEM and X-PEEM Characterizations of BTO(001) Surfaces

5.1.2.1 LEEM Studies on BTO(001) Surfaces

Near-field techniques such as piezoresponse force microscopy (PFM) or scanning surface potential microscopy (SSPM) are successfully applied to resolve changes in the surface potential [162, 163, 164]. Contrary to these techniques, in mirror electron microscopy (MEM) using a low energy electron microscope (LEEM), variations in the MEM-LEEM transition can be detected. The intensity variations are related to changes in the screening of the surface polarization charge. The MEM-LEEM technique avoids tip-surface interactions, which might otherwise influence the domain polarization [162, 165]. Utilizing LEEM in the MEM mode provides non-contact, full-field imaging of the surface topography and potential with $12 - 15$ nm spatial resolution [122].
We started by investigating the surface polarization of a clean BTO(001) single crystal surface by LEEM measurements. To determine the electrostatic potential difference above the surface between two domains, we took LEEM images at different start voltages (SV). The front image of the image stack in Figure 5. 2 a) presents a typical MEM-LEEM image from a clean BTO(001) surface taken at a SV of +3.2 V without UV illumination. Two clear intensity levels were detected corresponding to the different electrostatic potentials above the surface [162].
The reflectivity curves extracted from the two domains were plotted in Fig. 5. 2 b) as a function of start voltage. The inflection point of the decrease in the reflectivity curve marked the position of the MEM-LEEM transition. The shift in the MEM-LEEM transition between the two domains was 0.1 eV. This shift in electrostatic potential was a measure of the difference in the effective charge and here it was attributed to polarizations perpendicular to the surface inwards (P) and in-plane polarization. There was a good agreement between our experimental data and theoretical calculations presented in [68].

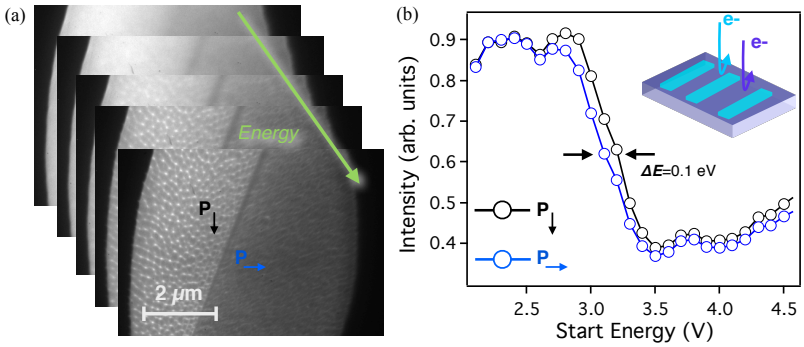

Figure 5.2: a) 3D LEEM image stack. Each individual image is taken at a different start voltage. b) Local reflectivity curves extracted from in-plane polarized (a) and out-of-plane polarized (c) domains as a function of start voltage without UV illumination.

Wang *et al.*[166] showed that the surface polarization charge in ferroelectric materials can be screened by a variety of mechanisms: intrinsic (charge carriers or defects in the bulk), extrinsic (chemical environment or adsorbates), domain ordering, or even a combination of the above [166]. Photo-generated charge carriers can efficiently screen the surface and interface polarization charge and hence the depolarizing field [166]. In order to verify the experimental proof of the ferroelectric domain screening on the BTO(001) surface by ultraviolet photo-induced charge, we carried out LEEM measurements. The MEM-LEEM transition was measured as a function of the ferroelectric polarization with and without UV illumination. The UV illumination was carried out by a Mercury discharge lamp with a primary line at 254 nm. Figures 5. 3 (a) and (b) show MEM-LEEM images from the clean sample with and without UV illumination, respectively. The potential contrast in the MEM-LEEM transition reflected the screening of the polarization charge of the a- and the c- domain surfaces. Three distinct intensity levels were observed corresponding to different electrostatic potentials above the surface, which was supported by the inversion in the intensity contrast as the SV was increased [162]. Bright, dark, and intermediate regions correspond to the c−, c+, and a domains, respectively. The 180° c+ and c− domains were separated by irregular curved domain walls (see Fig. 5. 3 (a)), suggesting that our data was consistent with Ref.[167]. The polarization vector of the a-domain laid in the (001) plane: It had no surface charge, thus, it was at zero potential and its contrast level was between the c+ and c− domains [167]. The reflectivity curves extracted from the two domains were plotted in the top panel of Figure 5. 3 as a function of SV with (filled circles) and without UV illumination (open circles). The shift in the MEM-LEEM transition between the two domains was

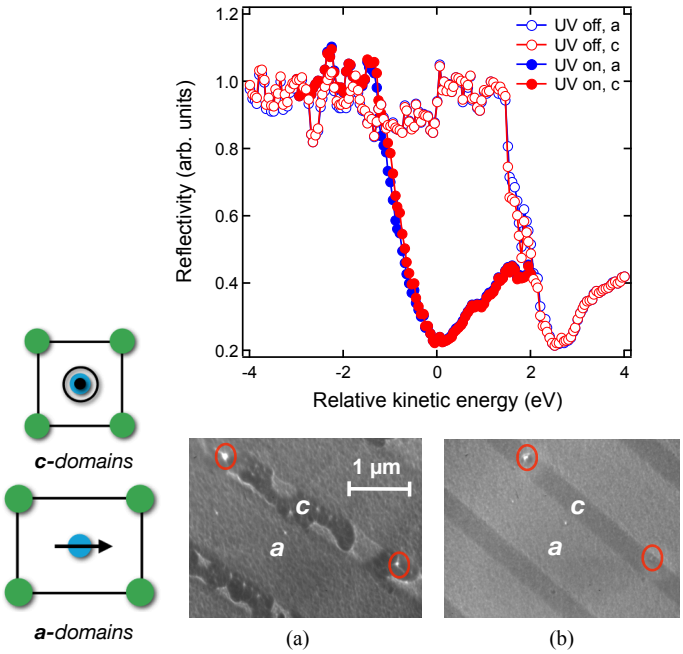

Figure 5.3: Local reflectivity curves extracted from a- and c- domains as a function of start voltage with (full symbols) and without (open symbols) UV illumination. a) MEM image at a start voltage of 1.5 V showing the contrast in the electrostatic potential above the clean surface of in-plane (a) and out-of-plane (c+,c-) polarized domains. b) MEM image at a start voltage of 1.5 V with UV illumination.

300 mV. This shift in electrostatic potential was a feature of opposite polarizations perpendicular to the surface, pointing either outwards (P+) or inwards (P). Shao *et al.* [165] reported a $150 - 200$ mV shift between c+ and c− domains using PFM, but their data were acquired in air, thus there was a high probability that the potential contrast was weakened by adsorbates [165]. In contrast to this, we had an adsorbate-free surface as shown by AES, since we prepared the single crystals in UHV and the measurements were performed *in situ*. Additionally, upon illuminating the surface with the UV light, the shift in the MEM-LEEM transition between the two domains was significantly reduced. As presented in Figure 5. 3 (b), the domain structure was changed by the UV illumination, and the contrast was reduced. When the UV light was switched off, the contrast gradually increased back to the original value (not shown here). The average value of the MEM-LEEM transition shifted by $\Delta V_{on} = 2$ V to lower SV when the illumination was switched on. This huge shift is attributed to the UV-induced pho-

toemission, charging the surface positively. The differences between the experimental report by Wang *et al.*[166] and our experimental findings is attributed to longer UHV annealing of the BTO single crystal. Upon longer UHV annealing we create more holes in the band gap, which causes the crystal to charge more positively.
The MEM-LEEM transition measures only a potential change perpendicular to the surface, therefore, in the case of an in-plane polarization only a photoemission induced shift to lower SV was expected with no screening by electron hole pairs. As shown in Figure 5. 3 (b), there was a 180° domain wall motion, when the UV light was switched on. Our results were in good agreement with the results reported in Ref.[165], where the authors showed that during imaging in contact mode, rapid 180° domain wall motion is visible in consecutive PFM images [165].

5.1.2.2 XPEEM Studies on BTO(001) Surfaces

The electronic structure of the as-prepared BTO single crystal surface was determined via XPEEM measurements. The ferroelectricity of BTO single crystal at room temperature is due to reduction of octahedral symmetry (O_h) around the Ti^{4+} ion to a C_4 symmetry [73]. Thus, the inversion symmetry is broken. Through the displacement of Ti and O atoms relative to each other, each unit cell possesses an electrical dipole moment [168]. In Fig. 5. 4, the unit cell of BTO single crystal in the cubic phase was illustrated.

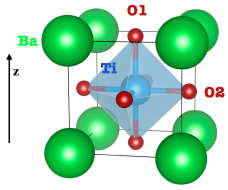

Figure 5.4: BTO unit cell in cubic structure [Reproduced from [168]]

The chemical environment of the oxygen atoms O1 and O2 of BTO in the cubic crystal structure is identical. Upon transition from cubic to the tetragonal phase, the environment of the oxygen atoms changes due to a shift in their position [168]. Furthermore, there is a shift of the Ti atom position along the c-axis. In the tetragonal phase the local electronic structure for O1 and O2 atoms is different. Likewise, the local electronic structure of Ba and Ti atoms changes upon the phase transition. The details of the lattice constants and the atomic displacement in cubic and tetragonal phases were displayed in Tab. 5. 1 [168]. In the tetragonal phase the degeneracy within the t_{2g} and e_g orbitals is lifted. However, this additional energy splitting is small and can only

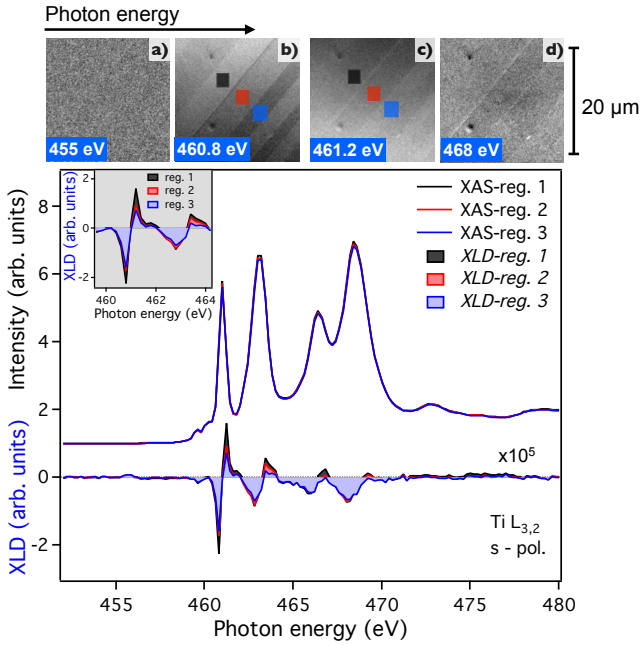

Figure 5.5: X-PEEM images and local XAS spectra of BTO as a function of photon energy in the area marked by the boxes are shown. The four PEEM images from a) to d) were recorded at different photon energies. Local XAS data is taken and plotted versus photon energy for the three domains, black, red and blue boxes in Fig. 5. 5, when the energy is scanned through the Ti $L_{2,3}$ edge with s-polarized x-rays. The spatially resolved XAS spectra are recorded from areas below 2 μm x 2 μm. On the lower panel of the figure, the XLD signal is reproduced.

be resolved by measuring the dichroism between the two different directions of linear polarizations as shown in Chapter 4. The anisotropy of the orbitals leads to different absorption intensities for s- and p-polarized X-rays giving the opportunity to study the charge anisotropy, and thus the ferroelectricity [73].

We performed XPEEM measurements on a clean BTO(001) surface to address the ferroelectricity. We took local spectra as a function of photon energy and X-ray polarization in the areas marked by the boxes in Fig. 5. 5 b) at the Ti 2p ($L_{2,3}$ edges), Ba 3d ($M_{4,5}$ edges) and O 1s (K edge) in the electron yield mode by performing XPEEM experiments at room temperature. In Fig. 5. 5 an example of an XPEEM image and the extracted local absorption spectra at the Ti $L_{2,3}$ edge measured in grazing incidence along the in-plane orientation (s-pol.) of BTO is presented. In Figures from

5. 5 b) to d) single XPEEM images of the BTO surface were shown for different photon energies, 460.8 eV, 461.2 eV and 468 eV, which corresponded to the Ti $L_{2,3}$ edge. An XPEEM image at the 450 eV -pre-Ti edge was also measured (Fig.5. 5 a)). The overall intensity variations were resolved from dark (a), to very bright (d). In the picture three areas marked as black, red and blue, are displayed. From these areas, the local-XAS data is extracted and depicted below.

The Ti $L_{2,3}$ edge spectrum originates from the Ti 2p (occupied or core level) to the 3d (unoccupied state) electronic transitions. As presented in the upper panel of Fig. 5. 5, the measured spectra closely resembled the spectra for a Ti ion in an octahedral coordination [153]. The four well-split peaks represented the characteristic structure of a Ti^{4+} $2p^6 3d^0$ to $2p^5 3d^1$ absorption process.

BTO is treated as a cluster made of Ti and six O atoms. The unoccupied 3d orbital states of Ti were assumed to be split into two states assigned as t_{2g} and e_g in perfect O_h symmetry, and were determined by the strength of the crystal field, *i. e.* the electrostatic potential, U due to oxygen ligands acting on 3d orbitals [154, 155]. In the octahedral O_h site symmetry the e_g orbitals of Ti point toward the oxygen ligands, while the t_{2g} orbitals point in between them, resulting in a lower energy for the latter [154]. None of these states is pure due to the mixing by $2p - 3d$ electrostatic interactions [154]. If there is a distortion of the octahedral symmetry present acting on the Ti site, there will be a non-symmetric broadening of especially the e_g peaks [154]. Lowering to tetragonal symmetry splits the t_{2g} and e_g states, which gives a difference between XA spectra taken with polarization along the z and x, y directions.

The Ti absorption spectra shown in Fig. 5. 5 matches well with the reported experimental and calculated absorption spectra at the Ti-$L_{2,3}$ edge. The features in the spectra

Table 5.1: Lattice constants and atomic positions of BTO in cubic and in tetragonal phase [Data are taken from [168]].

	cubic (x,y,z) [a]	tetragonal ΔZ [c]
Ba	(0.0, 0.0, 0.0)	0.0
Ti	(0.5, 0.5, 0.5)	0.0224
O1	(0.5, 0.0, 0.5)	-0.0105
O2	(0.5, 0.5, 0.0)	-0.0244
a [Å]	4.01	3.991
c [Å]	4.01	4.0352
c/a	1	1.01

were assigned according to the available literature on the Ti absorption process [154]. In the lower panel of Fig. 5. 5 the XLD signal was reproduced. The XLD signal was another indicator of the ferroelectric character of BTO. As shown in the Fig. 5. 5 b), three grey levels demonstrated three different ferroelectric domains, which were also visible as three different magnitudes of XLD. Eventually, these three regions corresponded to c, a1 and a2 domains. Figures 5. 5 b) and c) illustrate the ferroelectric contrast in a single X-PEEM image at the Ti e_g edges, i. e. where the XLD signal has its maximum (both in positive and in negative) indicating several types of domains.
Experiments using polarized light microscopy showed that the surface domain structure of BTO single crystals arranges in regular domains, in which either 90° or 180° domain walls separate neighboring domains [169]. In-plane domains are separated either by 180° or 90° domain walls (a1-a2 type domain variants), while in-plane and out-of-plane domains are separated by 90° domain walls (a-c type domain variants) creating a ferroelastic distortion.
A stripe-like ferroelectric domain pattern of BTO might be explained in terms of the pressure applied to the crystal during cleavage and/or during mounting the sample to the PEEM sample holder, which induced a stress. Annealing at moderate temperatures (below 800°C) did not entirely relax the lattice. Specific ferroelectric domains were stabilized by the lattice deformation [170].
A difference in contrast is seen when the ferroelectric axis is along or orthogonal to the x-ray polarization, because by using linear dichroism as a contrast mechanism for BTO, one is susceptible to the anisotropy axis in BTO [171]. It was not possible to distinguish between adjacent domains separated by 180° domain walls via XLD-PEEM, but we were able to observe the contrast between adjacent domains separated by 90° domain walls. Similarly, x-rays polarized parallel to the sample surface would show a contrast between domains of different in-plane ferroelectric axis orientations [171].
We performed XAS measurements by changing the azimuth angle at the Ti L-edges and at the O K-edge on the same spot of the BTO surface. The multiplet structures measured on the individual domains were changed. According to the angular-dependent XAS results, we concluded that the contrast seen in Fig. 5. 5 was due to the differently-oriented a-type (in-plane) ferroelectric domains.
In the last step, we present the local absorption spectra at the O K-edge in Fig. 5. 6. It originates from the transitions of O 1s core level into the final states with O 2p states. The features of the O K edge in Fig. 5. 6 were labelled as reported in [172]. The associated energies labelled as A, B, C, D, E and F are 533, 535.4, 535.8, 544.8, 548 and 554.4 eV, respectively. The features A and B are fingerprints for the excitation into O 2p orbitals hybridized with Ti 3d orbitals. We determined the energy separation between A and B as 2.4 eV, which corresponds to the crystal field splitting at the Ti $L_{2,3}$ edges. The feature C results from the transitions to O 2p − Ba 5d hybridized states.

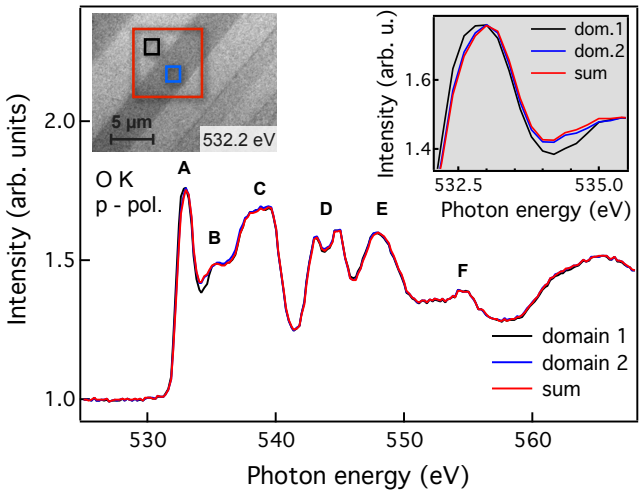

Figure 5.6: X-PEEM image and local absorption spectra of BTO as a function of photon energy in the area marked by the boxes are shown. The PEEM image on the left is recorded at the photon energy of 532.2 eV. Local XAS data is taken and plotted versus photon energy for the three domains marked as black, red and blue boxes in the left panel of Fig. 5. 5, when the energy is scanned through the K edge.

The peaks after C result from the transitions to final states consisting of O 2p, Ti 4s, 4p and Ba 5p levels.

As presented in [21], the presence of domains also had an influence on the BTO lattice. The a-domains provide a maximum anisotropic lattice strain of 1.1 % in the [100] direction in the tetragonal phase of BTO, which could result in an energy shift in the X-ray absorption spectra. On the right hand-side of Fig. 5. 6, the enlarged portion of the local-absorption spectra around $532 - 535$ eV proved this statement. The spectrum of domain 1 (black line) is shifted to lower energy in comparison to the spectrum of domain 2 (blue line). The result suggest that differently-polarized domains have different absorption cross-sections due to the relative alignment of ferroelectric polarization vector-or-the orbital orientation- and the x-ray polarization direction.

5.1.2.3 XPS Studies on BTO(001) Surfaces

Studying ferroelectric properties of materials is usually based on electrical characterizations, e.g. current-voltage *I(V)* characteristics or impedance spectroscopy. However,

macroscopic methods are limited to identify the interface properties due to the interdependence of parameters [173]. In addition, the microscopic properties cannot be directly accessed from such experimental approaches. X-ray photoemission spectroscopy (XPS) is widely used for many years to study semiconductor interface formation and is applied in the present work on the perovskite-structure titanate material BTO.

Photoemission spectroscopy is an important analytical technique to investigate the near surface/interface chemistry of $ATiO_3$ compositions (A: Ba, Sr) in the bulk form or in thin film form [173]. For instance, it is shown that cleaning $ATiO_3$ surfaces by ion bombardment yields a non-stoichiometric surface region introducing new features in the photoemission spectra making the data interpretation problematic [173]. Thus, the surface preparation is an important procedure in order to examine the intrinsic surface properties. Depending on the stability criteria and to the preparation conditions the actual surface termination is generally fixed [174].

The BTO surfaces were Ar^+ ion sputtered for a total of 20 min with 800 V accelerating potential at 10^{-5} mbar Argon pressure. The sample current during the sputter treatment was $I_{sample} = 6\ \mu A$. As described in the previous section, the crystals were annealed *in situ* at T = 600°C in an oxygen atmosphere of 4 mbar in UHV for an hour to obtain a clean surface reconstruction. Subsequently, to remove the residual contamination such as H_2O and CO_2 and to create sufficient oxygen vacancies the BTO single crystals were annealed at T = 700°C with a base pressure of 8 x 10^{-10} mbar for two hours. Firstly, the effect of successive annealing after Ar^+ ion cleaning on the surface morphology of the BTO single crystals was examined by AFM.

The AFM observations revealed a significant difference in the morphology of the BTO single crystals with and without successive annealing. Fig. 5. 7 a) and Fig. 5. 7 c) show the AFM results for only Ar^+ ion sputtered ("S"=BTO82) and Ar^+ ion sputtered and successively UHV annealed BTO ("S+A"=BTO83) single crystal surfaces. The surface roughness (R_{rms}) of these surfaces was 8 nm for BTO82 and 0.2 nm for BTO83. The relatively large surface roughness of BTO82 resulted essentially from Ar^+ ion sputtering. In contrast to BTO82, upon annealing the BTO83 surface developed back with the formation of ferroelastic domains as shown in the piezoresponse measurement performed on the same spot (see Fig. 5. 7 d)). The contrast was due to ferroelastic domain-walls forming between an in-plane and out-of-plane polarized domains, as described earlier in this chapter. Ferroelectric materials are sensitive to point defects. The absence of measurable piezoresponse for BTO82 surface implied that the electrical properties of ferroelectrics were drastically modified by the Ar^+ ion sputtering.

Secondly, XPS measurements were conducted to investigate the changes in the stoichiometry and in the electronic structure of the surface layers upon Ar^+ ion bombardment and successive annealing steps. XPS measurements were performed using a CLAM 4 hemispherical electron analyzer and a Mg K_α (1254 eV) X-ray source. The

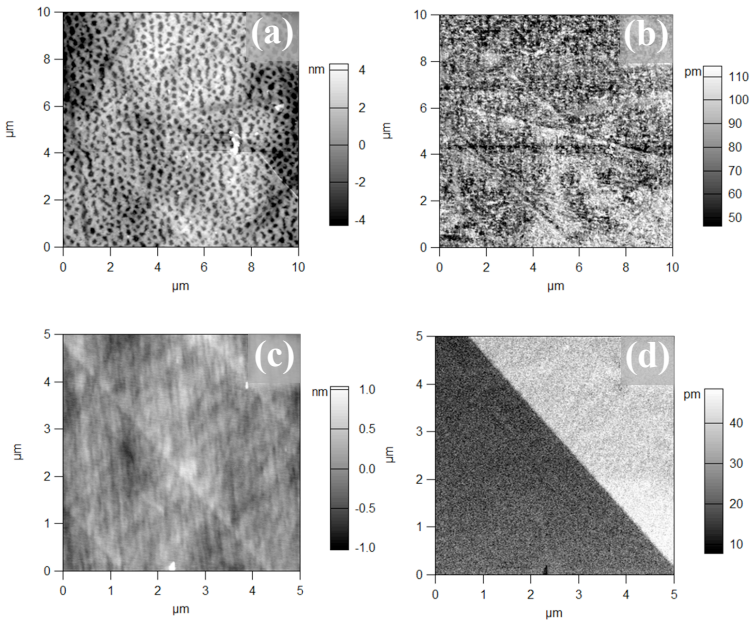

Figure 5.7: The dependence of the atomic force and corresponding piezoresponse micrographs on the surface treatment conditions for BTO single crystals. a) and c) represent the AFM measurement results on only Ar^+ ion sputtered (BTO82) and successively UHV annealed BTO (BTO83) single crystal surfaces, respectively. Similarly b) and d) show the piezoresponse micrographs for BTO82 and BTO83, respectively.

analyzer pass energy was $E_{pass} = 20$ eV. During the XPS measurements a step-size of $\Delta E = 0.05$ eV was used. Measurements were performed under 30° take-off angle. For each spectrum dwell time was of 100 ms. A sum over five scans was named as "quick scan" and the sum over 20 scans was named as "long scan".
The surface phase changes of BTO82 and BTO83 single crystals were verified by XPS measurements. We recorded the core levels at their characteristic binding energies for fine analysis of the chemical state. The Ti 2p core level spectra for BTO82 and BTO83 single crystal surfaces are shown in Fig. 5. 8. In general, the analyzer collects two kinds of electrons from the sample: (i) the primary electrons contributing to the chemical and electronic information and (ii) inelastically scattered electrons contributing to the background intensity (secondary electrons). For the primary electrons, the measured

kinetic energy was directly coupled to their inelastic mean free path, thus the background was subtracted from the signal.

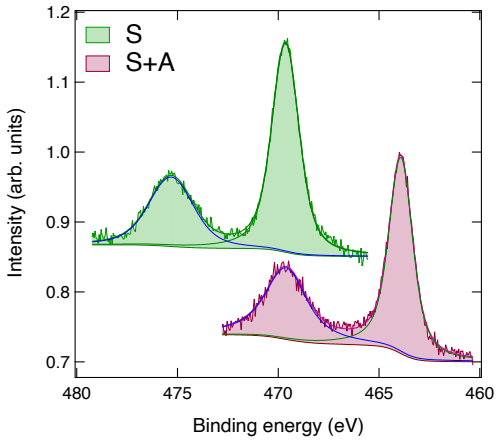

Figure 5.8: Ti 2p core level spectra for only sputtered ("S"=BTO82) and sputtered+annealed ("S+A"=BTO83) BTO single crystal surfaces. Spectra are vertically staggered for clarity.

The Ti 2p spectra shown in Fig. 5. 8 shed light on the preparation dependence and chemical state at the near surface region. Both Ti 2p spectra affirmed the spin-orbit split doublet corresponding to fully oxidized Ti^{4+}. The absence of suboxides, along with the increased electrical resistance (as determined from the conductive-AFM measurements), pointed to a stronger oxidation at the surface of BTO83. As followed from the Fig. 5. 8., the sample BTO83 was charging less than BTO82 - with a clear evidence in Ti 2p spectra and also the decomposition of O1s spectra. The shifting caused by charging was about ≈ 6 eV.
The temporal change of core level emission lines at the O1s edge versus the binding energy is presented in Fig. 5. 9. The evidence of both charging and not charging of O1s species is seen, probably as the sample was undergoing reduction under the beam. After the second measurement, the surface seemed to be reduced enough to start conducting. The samples were altered or damaged during the XPS measurement. The long scan seemed to be a mixture of different states, changing during the scan. The complicated peak composition therefore is not interpreted. We note that *ex-situ* XPS data of an only Ar^+ ion sputtered surface is not suitable for a reliable composition analysis, since the defects created during the cleaning step preclude a correct integration of the Ti XPS lines.

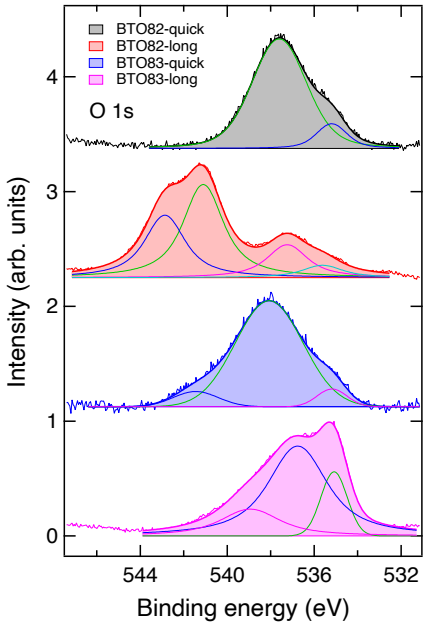

Figure 5.9: Temporal change of O 1s core level spectra for only sputtered (BTO82) and sputtered+annealed (BTO83) BTO single crystal surfaces. The spectra are normalized in intensities and shifted in the same axis to underline the shape change. A sum over five and twenty scans were denoted as "quick" and "long" scans, respectively.

In general, the presence of oxygen vacancies was expected, formed as a result of differential surface ion sputtering, creating an amorphised surface. AFM results confirmed this fact: The sputtered only surface (BTO82) was damaged by the Ar^+ ions. According to this consideration, there would be more Ba and Ti ions present on the surface, which would reduce the charging. However, BTO82 was more charging than BTO83, showing that our consideration was too simple to explain the findings only by differential sputtering.

Considering V''_{Sr} as an A-site cation, our result was compatible with other studies, which showed that heating $SrTiO_3$ in oxidizing atmosphere develops a V''_{Sr} ion concentration at the $SrTiO_3$ surface according to the defect reaction in the cation sub-lattice [175, 173]:

$$Sr^x_{Sr} + 2e^- + 1/2O_2 \longleftrightarrow V''_{Sr} + SrO_{secondary-phase}. \tag{5.1}$$

Sr ions diffuse outwards from the bulk to the surface, where they can react with gaseous oxygen and according to the equation 5. 1, establish SrO-rich surface phases. In our case, the surface would possess a BaO-rich phase. In reducing conditions, oxygen might desorb from the surface [173]:

$$O_O^x \longleftrightarrow V_{\ddot{O}} + 2e^- + 1/2O_2, \tag{5.2}$$

which is associated with an increase of oxygen vacancies ($V_{\ddot{O}}$) at the surface. Thus, the concentration of compensating V''_{Ba} ions correspondingly increases resulting in Ba migration from the surface to the bulk. Consequently, a Ti enrichment (and Ba-deficiency) can be assumed at the surface.
Reducing $SrTiO_3$ surfaces in vacuum above 900°C stimulated the establishment of Ti-rich surface phases, such as TiO and Ti_2O islands [175, 173]. The O 1s core level showed an asymmetric shape for the only sputtered BTO surface (BTO82). This might be an indication of the presence of Ti^{3+} and creation of oxygen vacancies, however, we did not observe any significant Ti^{3+} in the core level spectra of BTO82. Additionally, the oxygen vacancies were removed after oxygen annealing as confirmed by the symmetric O 1s and Ti 2p feature of BTO83.
The green component in the long scan, for both samples, represented the state dominant during the first minutes of the measurements. In contrast to the "pink component" in the case of BTO82 and the "pink and blue components" in the case of BTO83 were those being the only ones present in the quick scans, representing thus the altered (damaged) state. The average roughness obtained from AFM measurements also supported this observation. These "starting state" green peaks were shifted by $\approx +6$ eV in kinetic energy from BTO82 to BTO83, similar to the Ti 2p peak. Since both peaks were equally shifted, we deduced that the sample BTO82 was charged by $\approx +6$ eV over sample BTO83, which might also charge to a smaller extent, but it was better conducting.
Clearly, it was a difficult task to accurately fit the O1s with multiple chemical states and to interpret the data. We claim that the change of the spectra during the measurement is due to a decomposition of the oxide by the x-rays, which was not observed before.

5.2 Fe/BTO(001) Interfaces

Thin magnetic films display altered properties compared to the bulk owing to the reduction in size and consequently dimensionality effects. Especially interesting are the changes in magnetic thin film properties due to the interaction with a ferroelectric substrate, which offer possibilities of future applications. Borek *et al.* [172] presented first-principles calculations of XAS and the related XMCD for ultrathin Fe layers on

a BTO(001) single crystal surface within the framework of density functional theory. They found a weak dependence of the Fe film magnetic properties on the polarization direction of BTO [172].
The interface plays a crucial role in the applications of artificial multiferroic materials. In this regard, the chemical stability of the interface becomes a prominent point to discuss. The first few layers of Fe deposited on oxidic substrates such as MgO and NiO are found to be oxidized due to the interaction with the oxygen from the substrate. Since the Fe/BTO interface is a metal/oxide interface, it can be expected that the Fe layer close to interface is oxidized. With this in mind, we studied the sharpness of the interface, the role of the deposition-temperature, and the effect of grazing incidence deposition-dependent changes in the electronic properties of the Fe/BTO by XPEEM. First, the characterization of the Fe growth on BTO was presented and epitaxial Fe thin film magnetic properties were discussed.

5.2.1 In-situ growth characteristics of Fe on BTO(001)

Fe and BTO have in-plane lattice parameters of 2.866 Å and 3.991 Å, respectively [21]. Fe grows with 45° rotation of its cubic lattice with respect to that of BTO in order to reduce the lattice mismatch [29]. With the rotation of the Fe unit cell by 45°, a small lattice mismatch of 1.5 % is obtained, which assumes that the Fe[110]/$BaTiO_3$[100] epitaxial relation is given by the theoretical calculations [22].

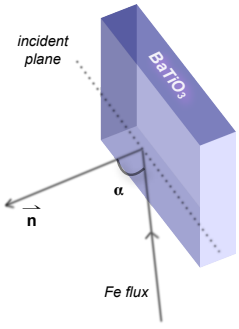

Figure 5.10: Illustration of oblique incidence deposition with α being the incident angle.

In this thesis ultrathin Fe films ($\approx$ 3 nm) were evaporated directly in front of the PEEM objective lens onto ferroelectric BTO single crystals by e-beam evaporation at room temperature. A schematical presentation of the oblique incidence deposition was shown in Fig. 5. 10. In the figure the incident angle is denoted as α.
In the LEED mode of the microscope, the structure and the long-range order of the

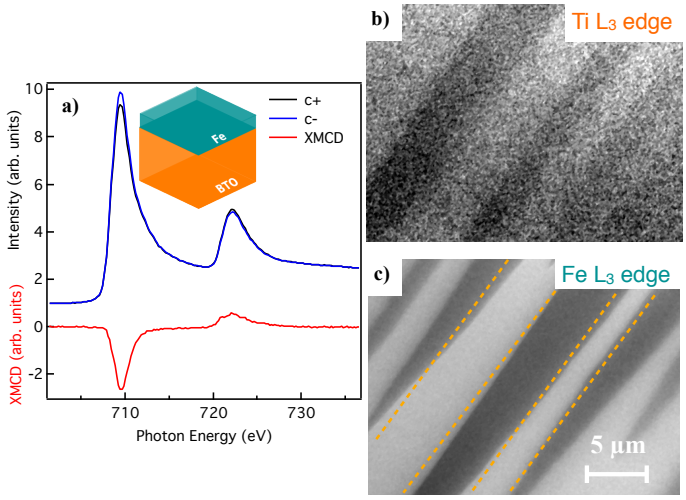

Figure 5.11: (a) Microspectroscopy extracted from darker magnetic domains (XMCD spectrum shown in red). Dichroic spectra from the domain show that the Fe L_3 edge has a shape corresponding to metallic Fe, rather than to an iron oxide. Inset: Sample layout: E-beam deposited Fe film on BTO single crystal. (b) Single image XLD-PEEM contrast (Ti L_3 absorption edge) of the buried BTO. (c) XMCD-PEEM image (Fe L_3 absorption edge) of an in-situ grown Fe layer. The iron film thickness is approximately 3.2 nm. Needle-like Fe magnetic domains are correlated with the ferroelectric domains. Dashed lines are guides to the eye.

Fe films were investigated. Prior to deposition, the BTO single crystal substrates showed sharp LEED patterns. On evaporation of the first few monolayers of Fe, the background intensity increased. However, the substrate spots faded away upon further Fe deposition. We would continue to see the same LEED pattern, if during Fe film growth the lattice constant of the growing film had not been changed. Modification of the lattice constant would have either created a new diffraction pattern or the existing pattern would have been completely lost. Since we did not observe a new diffraction pattern, we assume that the Fe film did not grow layer-by-layer on BTO under these conditions, which was probably hampered by the surface roughness and/or 3D island formation. The competition between the substrate surface energy $\sigma_{substrate}$, film surface energy σ_{film}, and film-substrate interface energy $\sigma_{interface}$ affected the growth mode of the film. There might be two mechanisms occuring:

- Fe atoms depostited on BTO formed clusters and developed into 3D island structure, i. e. the so-called Volmer-Weber mode.
- Fe atoms depostited on BTO initially formed one or two monolayers, which is followed by 3D island formation.

We noted that we cannot assess, whether the film has grown epitaxially or not only by the absence of LEED patterns.
We performed XMCD- and XLD-PEEM measurements in the same area of Fe/BTO at the Fe $L_{2,3}$ edge and at the Ti $L_{2,3}$ edge, respectively. We used spectroscopic imaging by scanning the photon energy while collecting single X-PEEM images. Dichroism images were an average of 50 images. Each image was taken with a 6 s acquisition time. This facilitated extraction of XMCD spectra from individual features. A spectrum collected from a single ferromagnetic domain was reproduced in Fig. 5. 11 a) (XMCD spectrum shown in red). The absorption spectrum of Fe shown in Fig. 5. 11 a) consisted of mainly two features. The peak at 709.6 eV (L_3 edge) resulted from the transition of electrons from the $2p_{3/2}$ to the unoccupied 3d states. The peak at 721.4 eV (L_2 edge) was the result of the excitation of $2p_{1/2}$ electrons to the unoccupied 3d states. An analysis of the Fe XAS line shape yielded information on the chemical state of the system. The lineshape matched those reported for Fe and clearly lacked the distinct peak splitting reported for magnetic iron-oxides. We claim that the magnetic domains are composed of metallic Fe [176].
The standard molar heat (enthalpy) of formation of a compound, $\Delta_f H^\circ$, is comparable to its enthalpy convertion when one mole of compound is formed at 298.15 K and 1 atm in kJ/mol [177]. The heat of formation of chemical substances relevant to our study in crystalline state is given in Table 5. 2. The interface sharpness is set by *i*) the surface free energies of BTO and Fe and *ii*) the affinity of Fe for O [21].

Table 5.2: Heat of formation values of chemical substances in crystalline state [177].

Molecular formula	$\Delta_f H^\circ$ [kJ/mol]
BaO	-548
TiO_2	-944
Fe	0
FeO	-272
Fe_2O_3	-842.2
Fe_3O_4	-1118.4

Owing to the modest heat of formation of Fe metal compared to Ba and Ti, Fe possessed a reduced affinity. As presented by [21], this would result in a very small interaction between the Fe and the substrate, when Fe was deposited on TiO_2 surfaces [21]. In this work, Fe was grown on BaO-terminated surfaces. Considering the absence of Fe oxidation- within the detection limit of XAS measurement- we concluded that in case of a system with a heat of alloy formation lower than the substrate, intermixing would be preferred [21].

In Figures 5. 11 b) and c) single image XLD-PEEM contrast (Ti L_3 absorption edge) of the buried BTO and XMCD-PEEM image of an in-situ grown Fe layer is presented, respectively. The iron film thickness was approximately 3.2 nm. Our first attempts of depositing ferromagnets yielded a needle-like ferromagnetic domain pattern. The vector components of the room-temperature magnetization in the Fe/BTO system were measured by taking advantage of the sensitivity of the XMCD effect to the magnetization component only along the X-ray incidence direction. By rotating the sample in the microscope through different azimuthal angles, we determined the magnetization components as in-plane for Fe magnetic domains with a spatial resolution below 40 nm. We assumed that the ferroelectric domain pattern was imprinted into the magnetic film to a certain extent via interface strain transfer, which induced local uniaxial magnetoelastic anisotropy axes via inverse magnetostriction [178, 25]. However, our assumption turned out to be wrong, which will be explained in Sec. 5. 2. 3.

The origin of the stripe-like pattern in the Fe film shown in Figures 5. 11 c) was further elucidated by examining the BTO ferroelectric domain structure directly. Due to the insulating nature of BTO it was difficult to image the ferroelectric domains with PEEM without a cap layer. For instance, Chopdekar *et al*. [171] deposited a 3.9 nm thick $SrRuO_3$ on BTO as a conductive capping to reduce surface charging. The photoelectron escape depth and thus the PEEM probe depth is on the order of 5 nm, so imaging through the BTO domain structure below the thin $SrRuO_3$ layer was possible. To our knowledge, our study was the first study investigating the buried ferroelectric domain configuration and the related multiplet structure in the Fe/BTO system. By taking local spectra as a function of energy and X-ray polarization in the area marked by the blue box in Fig. 5. 12 b), we observed a difference in the absorption between horizontally (p-pol.) and vertically polarized (s-pol.) X-rays. A typical set of absorption spectra and the corresponding XLD spectrum is shown in Fig. 5. 12 a). Fig. 5. 12 c) presents a close-up of the L_3 and L_2 edges, i. e. the region most often used to measure the magnitude of the linear dichroic effect in BTO-like ferroelectrics. Due to the limited electron escape depth, the linear dichroic effect was not as strong as the non-buried BTO surface.

Owing to the presence of an XLD contrast in Fe-covered BTO we claim that the electronic multiplet structure near the interface within the reach of total electron yield is

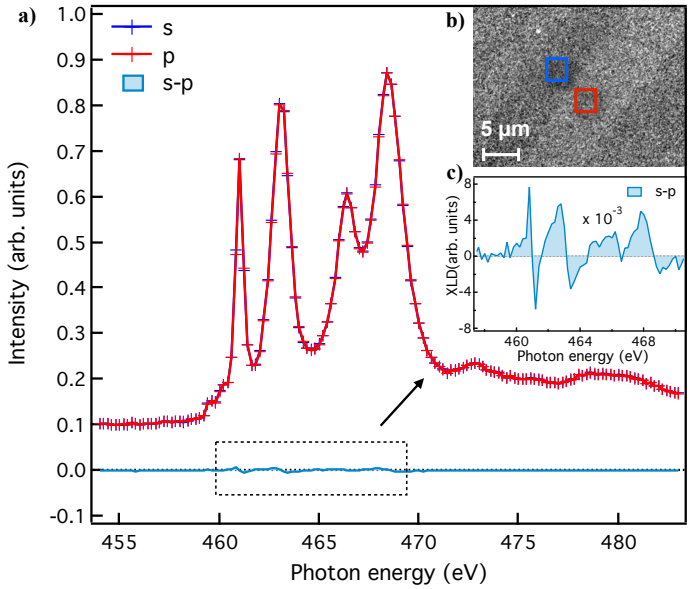

Figure 5.12: (a) X-ray absorption spectra with horizontal and vertical polarization at Ti L absorption edge of the blue boxed area in the inset b). (b) Single XLD-PEEM image at Ti L absorption edge of the buried BTO. (c) Enlarged portion of the difference in spectra showing large dichroism at L_3 and L_2 peaks.

independent of the metallic material deposition, thus the ferroelectric domain contrast did not vanish. However, we are careful about this interpretation. TEY-XAS is not only sensitive to the Fe/BTO interface, but also extends into the BTO at 3.2 nm cap layer so that no conclusions can be drawn about possible electron transfer at the interface, e. g. possible occupation of Ti t_{2g} or e_g states by the extra electron provided by the Fe.

The electronic structure upon a tetragonal distortion can be modelled by two parameters, t_{2g} and e_g. Here t_{2g} is defined as the energy difference between the d_{xy} orbital, and the d_{xz} and d_{yz} orbitals. e_g is defined as the energy difference between the $d_{x^2-y^2}$ and d_{z^2} orbital. The parameters t_{2g} and e_g are related to the parameters D_s and D_t, used in many textbooks, via $t_{2g} = 3D_s - 5D_t$ and $e_g = 4D_s + 5D_t$. In a first approximation, the both t_{2g} and e_g shells are empty. Therefore, the e_g states should not show any anisotropy if the e_g parameter is changed. One might expect no difference in spectrum when the e_g is varied. This, however, is not completely correct. The changes in spec-

tral line-shape were much smaller when e_g peaks vary, but still were clearly visible (see Fig. 5. 12 c)). The reason is that the final-state does change when e_g changes, therefore one finds differences in the spectra line shape for different polarizations.
We calculated the crystal field splitting and FWHM individually for BTO and for Fe/BTO systems. First, a change in the crystal field splitting upon Fe deposition was undetectable. Second, the overall spectrum before and after Fe depostion did not change its shape. Apart from the decrease in intensity, no major changes like peak splitting or shift in energy were seen in the Ti spectrum after Fe evaporation. These results suggested that the Ti^{4+} multiplet structure was conserved within the detection limit of our measurement.
Next, we deposited Fe on different oxide surfaces again in front of the PEEM objective lens to check the reproducibility of our results. We deposited Fe on:

- $SrTiO_3$(001) single crystal surface (Fe/STO),
- on bulk-like $La_{0.7}Sr_{0.3}MnO_3$ thin film surface (Fe/LSMO), and
- on re-prepared (Ar^+ ion-sputtered and oxygen-annealed $BaTiO_3$(001) single crystal surface (Fe/BTO).

Figure 5. 13 a) − c) shows the X-PEEM images taken at Ti L_3 and Mn L_3 absorption edges and Figure 5. 13 d) − f) presents the corresponding XMCD-PEEM images taken at the Fe L_3 absorption edge. The results are quite interesting: The ferromagnetic domain configurations are not related to the corresponding underlying oxide surface structure. We compare the Figure 5. 13 c) and Figure 5. 13 f). There is no correlation between the ferroic domains. We claim that the interface strain transfer in this Fe/BTO system is low or does not influence the ferromagnetic domain stripe direction. Even though the lattice elongation of the ferroelectric domains is not transferred to the Fe film, needle-like magnetic domains are still present. Local uniaxial magnetoelastic anisotropy axes are still in-plane (verified by the rotation experiments). We observed that depending on the roughness of the BTO surface after preparation steps as presented in Figure 5. 13 c), the ferromagnetic needle-like domain size changed (see Figure 5. 13 f). The texture improvement of the BTO surface yielded a wider ferromagnetic domain configuration, suggesting a low magnetocrystalline anisotropy (see Figure 5. 13 d).
We tackled the experimental influences on the needle-like domain formation. One key aspect to the interpretation of our results was that during evaporation in the microscope the Fe atoms entered the BTO surface plane under an oblique angle of approx. 30° with respect to the surface normal. The Fe growth was thus projected onto the BTO surface. In contrast to the work of Lahtinen [178, 25], the growth conditions in our case promoted the incoming vapour flux to make an angle with the film normal.

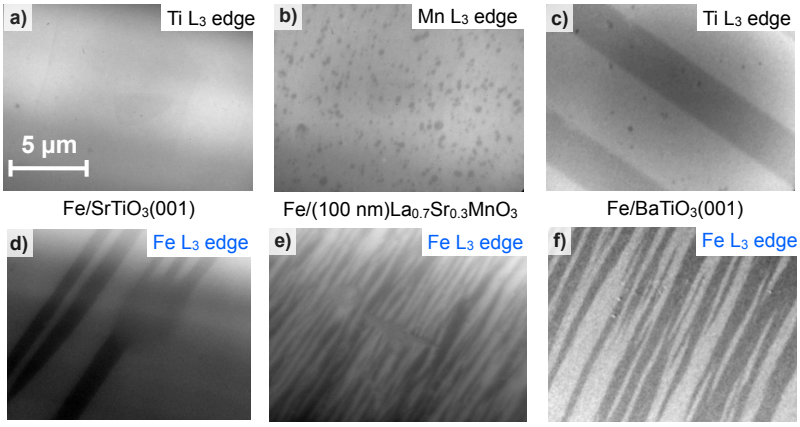

Figure 5.13: (a-c) X-PEEM images taken at Ti L_3 and Mn L_3 absorption edges with corresponding XMCD-PEEM images in panels (d-f) taken at the Fe L_3 absorption edge of an in-situ grown Fe layer. The iron film thickness is approximately 3.2 nm. Magnetization projections along in-plane [001] direction.

A specific feature in such a deposition was that certain parts of the growing film were shadowed for direct impingement [179]. As a result, the oblique-incidence deposition has promoted an anisotropic characteristics in thin Fe films [179]. The oblique deposition side effects were reflected in the nucleation and growth of Fe films. Such deposition configuration induced an anisotropy on the Fe film regardless the substrate that the Fe film was grown onto [179]. The details of this system were examined in detail in Sec. 5. 2. 3. Incorporation with the limited adatom mobility during the growth yields different film packing densities and morphologies to emerge in the directions parallel and perpendicular to the incidence plane [179].

The complete process of thin-film formation can be disentangled into the following phases: nucleation, island growth and coalescence stage, channel-filling stage, and growth of continuous films [179]. During deposition a certain amount of nuclei is formed [179]. A combination of surface roughness and oblique incidence deposition may affect the position of the nucleation centers [179], which may influence the ferromagnetic domain size and shape. Regions with adatoms have merged into larger clusters, called islands. At this stage the film was structurally discontinuous [179]. As the islands grew larger, coalescence occured at the interface between them, which reduced the surface free energy. However, a complete change of shape upon coalescence was less likely to

happen upon increasing size. We assumed that the island size distribution of metal overlayers on insulating substrates was inhomogenous mostly in the small thickness regime. Weak interaction between Fe and BTO would result in a large surface energy, thus a stretched-out, flat film. However, in our case not only the film thickness, but the growth conditions such as room temperature growth and the oblique deposition might be the reason of Fe film roughness. We speculated that OAD created a porous film. Detection of the XLD signal from a buried BTO surface was might become possible due to the porous nature of the Fe film.
To conclude, the importance of BTO as a substrate was outlined by the absence of intermixing with the Fe layers as was seen from the XAS investigations. The confirmation of a sharp interface opened the possibility of the non-oxidic metal film growth or 3D island growth on BTO, which made this system even more interesting for technological applications.

5.2.2 Effect of Fe growth temperature on the electronic structure and crystallinity

Thin-film growth is a kinetic and a thermodynamic phenomenon depending on the deposition conditions like substrate temperature and deposition rate. Our investigations of room temperature deposited Fe on BTO films resulted in a needle-like in-plane ferromagnetic domain configuration. However, the magnetoelastic coupling between Fe and BTO was not observed. Independent of the microstructure of the substrate the resulting magnetic domains were not coupled to the underlying ferroelastic domains.
The two most essential properties for describing the microstructure of the film are the morphology and the texture. The morphology strongly depends on the deposition parameters such as substrate temperature. It is expected that the adatom mobility is larger for [179]:

- smoother crystalline and chemically inert substrates
- increased substrate temperature during deposition
- lower deposition rate
- higher angle of incidence, and
- lower partial pressure of the ambient gases during deposition.

Among all these physical parameters the "*substrate temperature*" is the most straightforward parameter to apply. We assumed that heating the BTO single crystal would affect the microstructure of the Fe film due to the increased mobilty of adatoms. The local stress applied to the Fe atoms changes as a result of the BTO phase transition.

Thus, the substrate temperature was used to tailor the microstructure of the Fe films grown on BTO, which was the subject of this part of the thesis.
We deposited Fe at room temperature and at elevated temperatures (T = 600 K) under the same incidence angle and deposition rates in front of the objective lens of the microscope. A typical X-PEEM image of an as-received BTO single crystal surface prior to Fe deposition, which was recorded at the Ti L_3 absorption edge with x-ray polarization perpendicular to the c-axis (s-polarized light) is presented in Fig. 5. 14 a). Corresponding XMCD-PEEM images after Fe deposition at (T = 300 K) and at (T = 600 K) are shown in Fig. 5. 14 b) and Fig. 5. 14 c), respectively. We observed that the XMCD-PEEM contrasts of both Fe films were not related to the corresponding underlying surface structure. We therefore claimed that the interface strain transfer in these Fe/BTO systems was low or did not influence the ferromagnetic domain configuration.
One of the two contributors to the adatom movement direction is the surface diffusion, which might result in a random movement along the surface depending on the substrate temperature. The second one is the oblique-incidence direction of the incoming atoms [179]. This drives the atoms to have a momentum component parallel to the incident plane. The atoms are trapped in a region where their thermal energy becomes low, e. g. at the edge of a nucleus or due to oxide formation [179]. Thus, the ferromagnetic domains are affected by the growth mechanism as is the case presented in Fig. 5. 14 b). On the contrary to the Fig. 5. 14 b), the Fe film grown at T = 600 K showed a granular magnetic domain contrast. Also, here we evaporated the Fe films directly in front of the objective lens of the PEEM with the same evaporator. In the LEED mode of the microscope, we investigated the structure of the Fe films. After the full Fe film evaporation, we observed LEED spots indicating the presence of long range ordering of Fe atoms.
We explain these seemingly contradictory observations on the basis of surface diffusion. At elevated BTO substrate temperatures surface diffusion governs the formation of the layer [179], whereas the diffusion of Fe into the substrate is not expected at T = 600 K deposition temperature [180]. The effect of shadowing is reduced, when the adatom mobility increases. Due to the greater mobility, the particles are able to diffuse more uniformly over the surface [179]. Besides surface diffusion, one might count also on the migration of crystallite boundaries for the crystal growth at T = 600 K.
Based on the available experimental data of thin-film growth, two major conclusions are drawn from this work: (i) Shadowing effects and surface diffusion greatly influenced the growth of the films. (ii) At elevated temperatures surface diffusion might have partly cancelled the shadowing effect. The shadowing mechanism effectively pointed out that the atoms in the growing film shadowed the unoccupied sites from the direct path of incident atoms. Owing to the limited mobility in case of room temperature growth, most of the unoccupied sites were left empty. The resulting morphology would be columnar

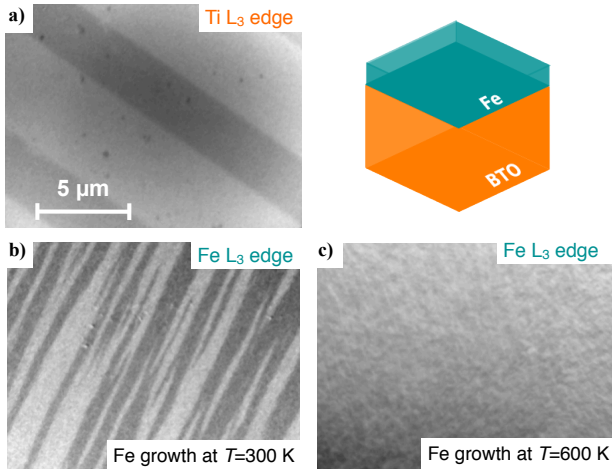

Figure 5.14: a) XPEEM image of BTO surface prior to Fe deposition. The image was recorded at the Ti L_3 absorption edge with x-ray polarization perpendicular to the c-axis (s-polarized light). Next to the X-PEEM image schematical sample layout: E-beam deposited Fe film on BTO single crystal is presented. Corresponding XMCD-PEEM images after Fe deposition, at room temperature and at elevated temperature (T = 600 K) under same incidence angle and deposition rate are shown in b) and c), respectively. In b) the adatom mobility is limited thus a columnar growth is present, where in c) physical processes are dominated by the surface diffusion.

with the columns tilted towards the effective incoming direction, thus we claimed that oblique-incidence deposition provided a tool to tailor the morphology of the Fe films. With the effective incoming direction getting closer to perpendicular incidence, like in the case of references [25, 178] and/or with increasing substrate temperature, the surface morphology changed. Along with that also a new magnetic configuration of the film developed.

We claim that the needle-like domain formation is a feature. First of all, different morphologies emerge in the incidence plane. The morphology is related to the physical parameters, such as electrical resistance, magnetic shape anisotropy and magnetic coercivity, its specific features can be exploited to realize anisotropic behaviour in obliquely deposited thin films. By evaporation conditions (e. g. direction of the incoming atoms) we could pre-define the preferred magnetization direction still with a good epitaxy. The outlook was to prepare the Fe films with preferred domain direction along the ferroelectric domains.

5.2.3 Elimination of deposition side-effects on the Fe-BTO ferroic domains

5.2.3.1 Normal incidence *in − situ* Fe film growth on BTO

Different aspects of oblique growth deposition and its correlation with magnetization in thin Fe films were studied in Fe/BTO systems. Due to symmetry breaking, intermixing or hybridization effects at the Fe/BTO interfaces new physical properties emerged such as magnetic anisotropy. One of the sources of magnetic anisotropy is the oblique-incidence deposition geometry [181]. In the initial stages of the growth the presence of substrate steps due to ferroelectric domains were intrinsically higher than one Fe atomic layer. This prevented Fe island interconnection and thus the large volume magnetic domain formation.

In standard operation conditions, the sample floated at 15 kV and was almost 1 mm away from the objective lens. All lenses starting from the objective lens scale with the sample bias and at 15 kV there is a non-vanishing magnetic field at the sample position due to the magnetic objective lens. According to the simulations [29] using the parameters 1000 windings and a current of 0.7 A for the objective lens, the magnitude of the magnetic field generated at the sample position was calculated as 1 mT, however, depending on the exact geometry of the objective lens this value may change. The magnetic field direction lays mainly along the optical axis of the microscope and the sample normal is also aligned with the optical axis. A magnetic stray field of 1 mT may be neglected for most of the magnetic films except for soft magnetic materials. The coercive field of 26 ML Fe grown on BTO by MBE was estimated to be larger than 5 mT [21].

Figures 5. 15 a1) − c1) and 5. 15 a2) − c2) depict the XLD-PEEM images at the Ti absorption edge and XMCD-PEEM images at the Fe absorption edge of the Fe/BTO systems, respectively. The contrast in Fig. 5. 15 a1) − c1) presents the ferroelectric domain patterns of the BTO single crystal surface. Prior to Fe deposition, BTO single crystals were prepared in UHV as described in the previous chapter. Approx. 3.2 nm thick Fe (26 ML) is deposited by e-beam evaporation on to BTO at T = 300 K with a base pressure $8x10^{-10}$ mbar. In Figs. 5. 15 a2) and b2) films were grown in front of the magnetic objective lens of the microscope in operation, whereas in Fig. 5. 15 c2) the film was grown in the prep-chamber. The bright and dark regions in the XMCD-PEEM images corresponded to the magnetic domains with magnetic vectors parallel and antiparallel to the incident synchrotron radiation, respectively. Likewise, the grey scales in the XLD-PEEM images presented the a-type (in-plane) ferroelectric domains.

The XMCD-PEEM images of the Fe films in Figs. 5. 15 a1) and b1) illustrated the Fe

[29] Simulations were performed by Dr. A. Kaiser from SPECS GmbH, Berlin, Germany

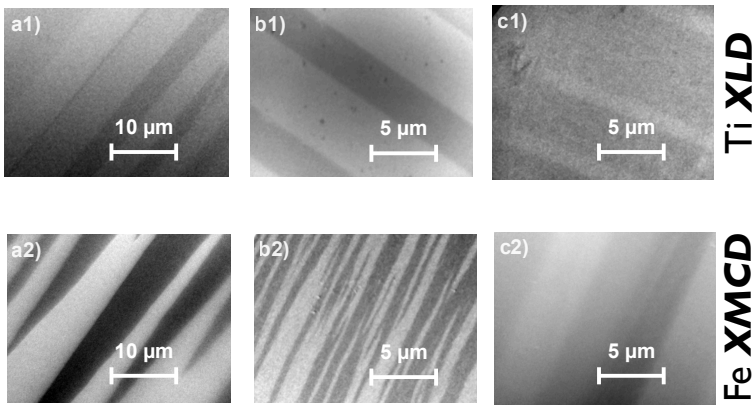

Figure 5.15: (a1-c1) XLD-PEEM images taken at Ti L_3 absorption edge with corresponding XMCD-PEEM images in panels (a2-c2) taken at the Fe L_3 absorption edge of an in-situ grown Fe layer. The iron film thickness is approximately 3.2 nm. Magnetization projections along in-plane [001] direction. First two images (a2-b2) are examples of an in-situ Fe deposition at room temperature with an oblique-angle deposition in front of the objective lens of the microscope with applied voltage. Image c2) presents the Fe film grown at room temperature in the prep-chamber with normal incidence growth.

films grown *in situ* in front of the magnetic objective lens of the microscope at operating high voltage of 10 keV and 15 keV, respectively. Magnetic domain imaging of Fe films were obtained at an azimuth angle of ca. 20° between the incident X-ray beam direction and the [001] direction, respectively.
Due to oblique growth adatom diffusion was limited and thus columnar growth appeared [182]. Both figures showed magnetic domains and presented the shadowing effect granted by the limited surface diffusion. In order to check the reproducibility of our results we prepared eight samples. We observed the same needle-like ferromagnetic domains in all samples. For example, we deposited Fe films not only on as-received BTO single crystals, but also on re-prepared BTO single crystals. The re-preparation sequence included removal of Fe by Ar^+ ion sputtering and successive annealing steps with/without oxygen in UHV. In Fig. 5. 15 b2) ferromagnetic domains were smaller than the ferromagnetic domains shown in Fig. 5. 15 a2). We claimed that due to surface cleaning the BTO surface roughness increased and this amplified the shadowing effect. The texture of the substrate surface influenced the magnetic domain structure. Magnetic field application during Fe film deposition might have induced an easy axis of

magnetization on magnetic film in one direction. To create a magnetic field-free region around the sample, we turned off the objective lens during Fe film deposition. However, we obtained same magnetic domain configuration.
We observed that regardless of *i*) the operating high voltage, *ii*) the surface treatment and *iii*) magnetic field generated by the objective lens the Fe XMCD images looked always similar. Previous studies showed that oblique-angle deposited films have magnetic anisotropies driven by the film morphology [183, 184]. For example, Z. Ali showed that uniaxial anisotropy and coercive field of a permalloy film ($Ni_{81}Fe_{19}$) increased with increasing deposition angle due to anisotropic film texture [185]. Due to OAD the microstructure of the film was extended along the incoming material flux. The surface topography in this case is called as columnar microstructure (see Fig. 5. 16 a)).

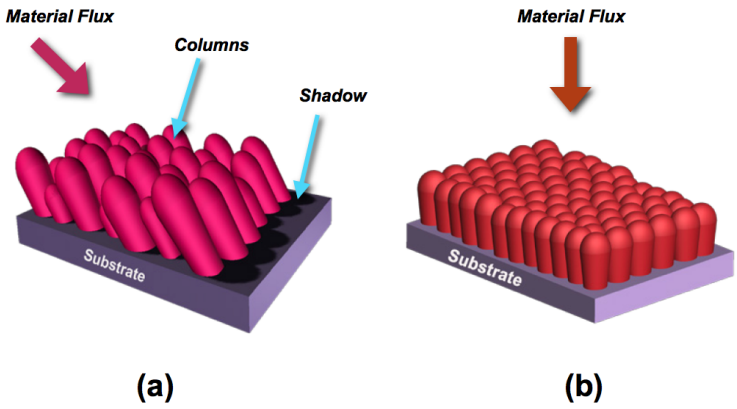

Figure 5.16: Schematic representation of (a) oblique angle incidence and (b) normal incidence Fe growth modes. Figure is adapted from Ref.[185].

We assume that the total anisotropy energy in Fe/BTO system is determined by E_{total}:

$$E_{total} = E_{growth-induced\ anisotropy} + E_{magnetocrystalline\ anisotropy} + E_{magnetoelastic\ anisotropy}. \tag{5.3}$$

In any Fe/BTO(001) system, the magnetoelastic anisotropy competes with intrinsic magnetic properties such as magnetocrystalline anisotropy, exchange and magnetostatic interactions between ferroic domains [186]. However, here the dominant anisotropy energy in the system seemed to be the $E_{growth-induced\ anisotropy}$ due to oblique-angle Fe

film deposition. To eliminate the growth-induced magnetic anisotropy, one can *i*) anneal the film at elevated temperatures, *ii*) rotate the BTO single crystal 360° during Fe film deposition and *iii*) grow Fe films at normal incidence angle.

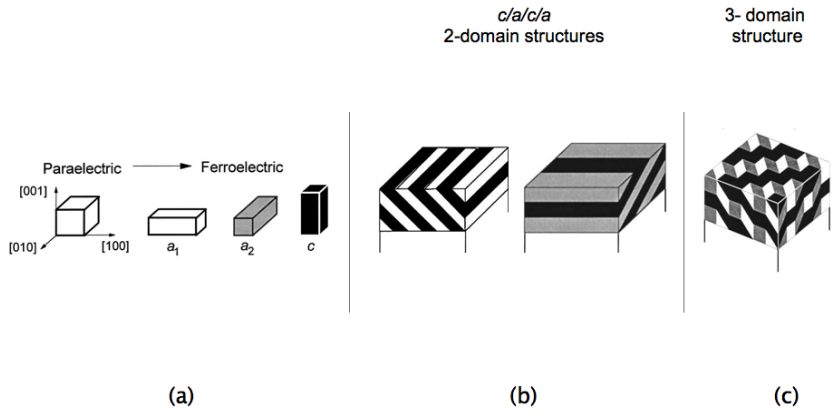

Figure 5.17: Schematic representation of BTO ferroelectric domains. (a) Transition from cubic paraelectric phase to the three tetragonal ferroelectric domains, (b) the simple two-domain c/a/c/a polydomain structures, and (c) second-order polytwin three-domain architecture of a and c domains. Figure is adapted from Ref. [152].

Next, we deposited Fe on BTO in the preparation chamber attached to the microscope to grow Fe films $in-situ$. We study whether the presence of needle-like domains were deposition condition artifacts. The expected side-effects that we eliminated by evaporating Fe in the prep-chamber were: *i*) the influence of magnetic field caused by the objective lens which scales with the high voltage of the sample and *ii*) the influence of the oblique growth which might be the dominant factor affecting the diffusion of Fe atoms on the insulating oxide surface. Fig. 5. 15 c2) is an example for an Fe/BTO(001) system with the Fe film being grown in the prep-chamber at room temperature with normal incidence growth. The magnetic domain size and configuration corresponded to the ferroelectric domains. The absolute orientation of the ferroic domains did not match. We related it to the sample transfer from the prep-chamber to the main chamber, after which most likely the spot on the sample was different, which might have led to the rotated ferromagnetic domains with respect to the ferroelectric domains. Roytburd *et al.* showed that in order to relax the stresses ferroelectric materials form

multi-domain structures [152]. Initially, this phenomenon is attributed to epitaxial ferroelectric $PbZr_{0.2}Ti_{0.8}O_3$ films of 450 nm thickness, which can be treated as a bulk material. The $2-$domain architectures, consisting of a and c domain structures, are shown in Fig. 5. 17 b). The magnetic domain structure observed in Fig. 5. 15 c2) was correlated with the underlying ferroelectric domains. Domain size was on the order of 5 μm which coincided with the ferroelectric domain width. This indicated that the BTO imprinted the ferroelectric domain pattern on to the Fe layer, when Fe was deposited in normal incidence configuration and in a magnetic-field free environment. Our results support the experimental findings presented by Lahtinen *et al.* [186].

5.2.3.2 Normal incidence $ex-situ$ Iron wedge film growth on BTO

We investigated the magnetoelectric coupling in an *ex situ* grown Fe/BTO(001) system. Fe film was grown at room temperature onto BTO(001) in a molecular beam epitaxy (MBE) chamber at PGI-6 by Thomas Jansen. The BTO single crystal was pre-characterized before Fe film deposition. We prepared Fe wedge films of thicknesses between $0-5$ nm. We used a 0.8 nm thick MgO capping layer to prevent the Fe film from $ex-situ$ oxiditation. A simplified representation of the sample geometry is shown in Figure 5. 18 (c).
XMCD-PEEM images taken at E = 709.6 eV (Fe L_3 absorption edge) at thin (< 1.5 nm) and thick (> 1.8 nm) regions of the Fe wedge are shown in Fig. 5. 18(a) and (b), respectively. We estimated the Fe film thickness by measuring the secondary electron yield signal of Fe. We have observed different magnetic domain patterns depending on the thickness of the Fe film. As shown in Fig. 5. 18(a) at a region with a thinner Fe layer the magnetic domain structure mimiced the ferroelectric domain configuration, i. e. the so called "*herringbone pattern*" (See Fig. 5. 18(d) and (e)). Black and white contrast in XMCD images indicated magnetization along the X-ray propagation direction, which was marked on the image by the yellow arrow in individual XMCD-PEEM images. Dark and light gray contrasts indicated that the magnetization was making an angle with the incoming X-rays. The observed magnetic pattern correlated to some extent with the ferroelectric domains [187]. This result confirmed that experimental findings on *in situ* grown Fe films on BTO in the previous chapter are not accidental. The Fe film deposition on BTO in normal incidence produced compact thin films. The energy term defined as $E_{growth-induced\ anisotropy}$ diminished. Hence, the ferromagnetic contrast depends on the competition between the magnetoelastic and the magnetocrystalline anisotropies.
Figure 5. 18(b) presents the XMCD-PEEM image on a thicker region of the Fe film. We have observed that the magnetic contrast was not very strong. Though, the strain transfer due to the a/c ferroelastic domain transition of BTO was established on the

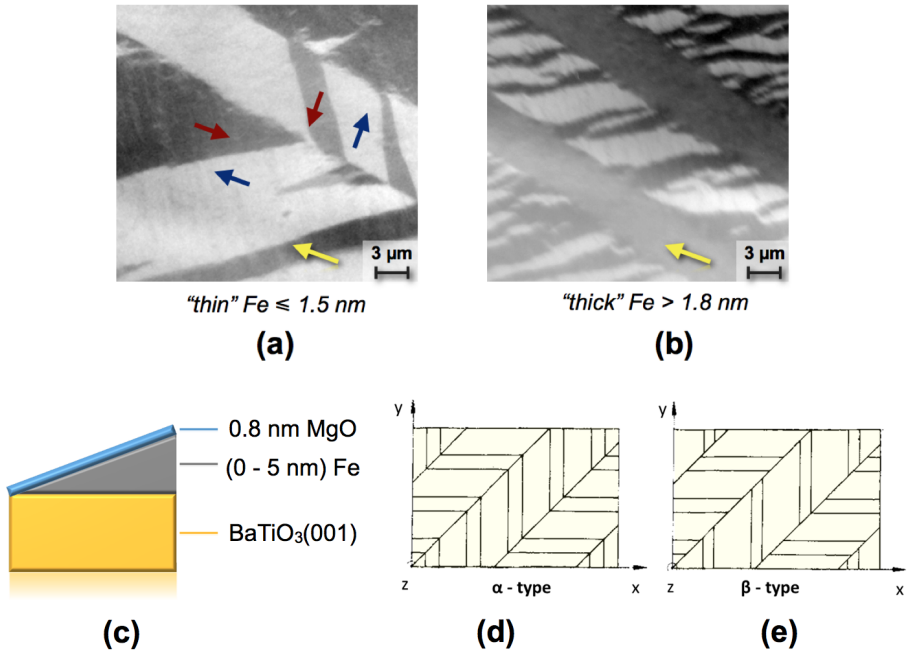

Figure 5.18: XMCD-PEEM image of a thin Fe film (a) and thick Fe film (b) taken at E = 709.6 eV (Fe L_3 absorption edge). X-ray beam direction is symbolized by the yellow arrow in individual XMCD images. (c) Illustration of the Fe/BTO wedge sample geometry. (d) and (e) Two kinds of herringbone patterns. The β-type has no correspondence across the C walls. Herringbone scheme is reproduced from Ref.[187].

ferromagnetic contrast. With increasing Fe film thickness the domain wall width increased. As shown in Fig. 5. 18(b) in order to compensate the stray field energy the magnetic domain size reduced. To support our claim we zoomed in the region on the same spot and took XMCD-PEEM images and performed X-ray absorption spectroscopy at the Fe absorption edge with circulary polarized left and right helicities.
In Fig. 5. 19 (b) a XMCD-PEEM image of 20 μm field of view (FOV) on the same spot of Fig. 5. 19 (a) is presented. To obtain XMCD contrast in Fig. 5. 19 (b) we performed imaging by inserting *i*) the energy filter entrance slit of the microscope and *ii*) the contrast aperture to filter the secondary electrons to achieve a better lateral resolution. With better PEEM resolution we have shown that stripe-like domains were separated by rather complex magnetic configurations (marked with red open circle), which occurs in

films with varying easy-axis direction and/or magnitude of the anisotropy constant. The so-called "*anisotropy dispersion*" of magnetic films is caused by the inhomogeneities in the film structure [75]. As a result, the direction of the local magnetization M varies slightly within a domain, which adds exchange energy to the system. Furthermore, due to the divergence of M free magnetic poles are created within the domain causing stray field and magnetostatic energy contribution [75]. The system minimizes these energies by varying the direction of the M in a wavelike manner, i. e. "*magnetic ripple*" [75]. Fig. 5. 19 (b) revealed that two regions marked as yellow and red open circles in the XMCD-PEEM images did not consist of distinct magnetizations.

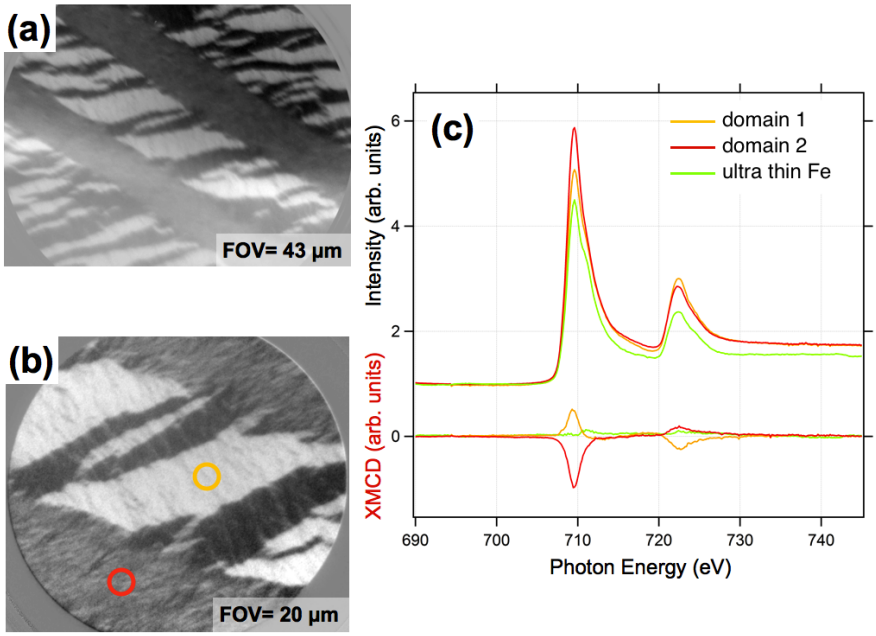

Figure 5.19: XMCD-PEEM images of MgO/Fe/BTO wedge system with Fe thickness larger than 1.8 nm taken at E = 709.6 eV (Fe L_3 absorption edge) with 40 μm field of view (a) and with 20 μm field of view (b). Black and white contrast indicates magnetization along the X-ray propagation direction, which is marked on the image by the yellow arrow in each XMCD-PEEM image. Dark and light gray contrasts indicate oblique magnetization along the incoming X-rays. The XAS spectra extracted from domain 1 (yellow circle), domain 2 (red circle) and ultra thin Fe region of the film (c). In the lower panel XMCD spectra of each region is shown.

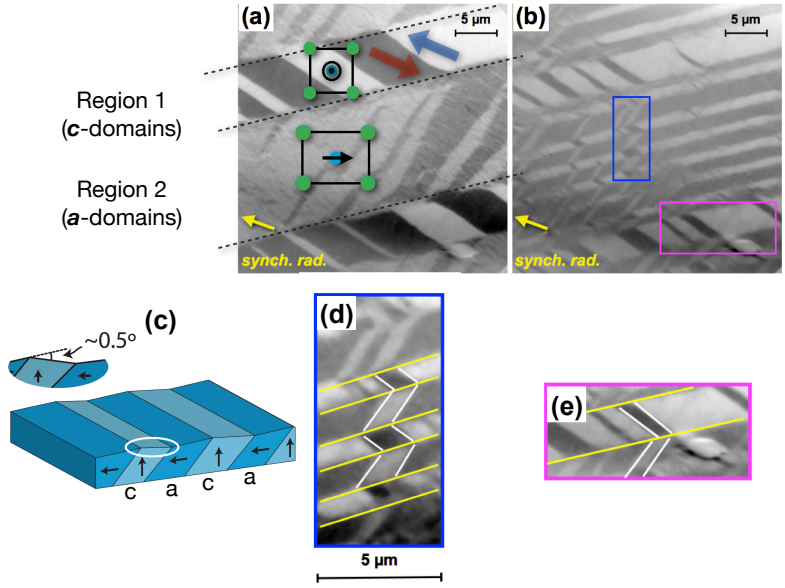

Figure 5.20: XMCD-PEEM images taken at Fe L_3 absorption edge on a relatively thin Fe film grown on BTO(001) single crystal before (a) and after (b) annealing *in situ*. Yellow arrow on the images indicates X-ray propagation direction. (c) A possible domain pattern on BTO(001) surface with an inset showing the angle between $a-c$ domains. Yellow and white stripes in (d) and (e) symbolize 90° and 180° ferroelectric domain walls, respectively.

We suspected that here the magnetocrystalline anisotropy governed the magnetic domain formation, since the magnetic domains were extremely small and there was magnetic ripple. The XAS spectra were extracted from domain 1 (yellow circle) and domain 2 (red circle). From the XAS data we calculated the XMCD spectrum of each domain (see lower panel of Fig. 5. 19 (c)). We found that XMCD spectrum of domain 1 differed from XMCD spectrum of domain 2 in magnitude and in polarity. Fe film oxidation could be neglected for the domain 1 and domain 2 due to lack of recognizable high energy side of Fe L_3 absorption edge. We also performed XAS on the ultrathin Fe film covered region. As presented in Fig. 5. 19 (c) by the green line, the XMCD signal was undetectable. The prominent oxidation peak for the ultrathin Fe film suggested that the formation of an FeO_x layer at the Fe/BTO interface destroyed ferromagnetic ordering.

Finally, we studied the effect of the annealing process on the interface coupling in the Fe/BTO(001) system. At high temperatures BTO is cubic and thus not ferroelectric.

On cooling it becomes tetragonal below the Curie temperature of $T_C = 395$ K. Sahoo *et al.* [24] showed that the Fe film magnetic properties are strongly modified by the BTO lattice distortions during its structural phase transitions via magnetoelastic coupling at the interface. The magnetoelastic energy promotes to uniaxial anisotropy [75]. We prepared a new wedge Fe film on BTO and performed temperature-dependent XMCD-PEEM measurements at Fe L_3 absorption edge. Figure 5. 20 (a) presents XMCD-PEEM image taken at room temperature. The Fe film magnetic contrast reflected the semi-Herringbone ferroelectric domain structure of $BaTiO_3$. Region 1 and region 2 corresponded to the previously observed c- and a-type domains, respectively. Black and white contrast indicated magnetization anti-parallel and parallel to the X-ray propagation direction, respectively. Dark and light gray contrasts indicated that magnetization was making an angle with the incoming X-rays. As shown in the schematical drawing in Figure 5. 20 (c), 0.5° inclination of the surface is caused by the unequal lattice parameters of a and c domains. We assumed that intrinsic shadowing occured at the ferroelastic domain wall boundary, which hindered Fe film compactness, thus establishment of well-grown Fe film.

Figure 5. 20 (b) presents the XMCD image of the same sample annealed at T = 600 K for 30 min *in situ* during PEEM operation. Annealing rearranged the magnetic domain configuration to minimize the ferroelectric domain wall energy. After the annealing process, we observed that the ferroelastic domain pattern including 90° in-plane rotations of the ferroelectric polarization and elongated c axis illustrated in Figure 2. 8 (b) was almost fully reflected in the ferromagnetic domain contrast. Elongation of the unit cell induced uniaxial lattice strain and magnetoelastic anisotropy in Fe film [186] as seen in the Figure 5. 20 (b) by the zigzag shaped ferromagnetic domains.

Owing to the structural transitions occuring upon cooling a new ferroelectric domain pattern was generated. We have observed that the α-type Herringbone ferroelectric domain structure was promoted in BTO as reflected on the ferromagnetic domain contrast. We have sketched yellow and white lines on Figures 5. 20 (d) and (e) to visualize ferroelectric domain walls. Yellow and white stripes symbolized 90° and 180° ferroelectric domain walls, respectively.

We noted that during annealing the XMCD contrast did not vanish completely. This suggested that the long range magnetic order existed in Fe film up to 600 K. Annealing induced interdiffusion at the interface between BTO and Fe film, which caused intermixing of Fe atoms with oxygen. Magnetic domain contrast decreased as the number of electrons of Fe element that contributed to the magnetic domain contrast decreased compared to the pure Fe. Thus, due to the oxidation of Fe film, we detected a reduced XMCD contrast after annealing.

Chapter 6

Summary and Outlook

One of the objectives in the field of spintronics is to combine ferromagnetic materials, i. e. the source of the spin-polarized electrons with ferroelectric materials. This combination is expected to establish a strong magnetoelectric coupling, which would make electric-field control of magnetization possible. The utmost requirement for the combination of ferroic orders is the control at the coupling interfaces.
The basic aim of this thesis was to gain fundamental understanding on the magnetoelectric coupling phenomena in BTO/LSMO/STO and in Fe/BTO model systems. At first, we explored the correlation between the thin film preparation parameters in the BTO/LSMO/STO system, such as substrate preparation, BTO and LSMO film thicknesses, growth temperatures and post-preparation techniques of individual layers, and their combined impact on the magnetoelectric coupling. We found that LSMO films grown on STO(001) substrates possessed an in-plane tensile strain with an in-plane magnetic anisotropy. Successive studies on LSMO films showed that with increasing deposition temperature the grains at the film surface coalesced, upon which the physical properties of LSMO films such as surface roughness and magnetic ordering temperature were recovered.
Later, we prepared BTO/LSMO heterojunctions. PFM measurements on very thin BTO films did not respond to domain writing. Patterning avoidance was due to the poor retention. In order to overcome the retention losses, which were mainly due to leakage currents, we grew bulk-like BTO films. Our studies revealed that thicker BTO films overcame the charge manipulation problem, i. e. ferroelectric domain writing by PFM became possible. Local X-ray absorption data obtained by XPEEM measurements revealed that our film had an electronic structure close to bulk BTO, however Ti-spectra between differently-polarized regions were almost identical. High intensity of X-rays might have caused re-polarization destroying the pattern polarization by photon-generated carriers.
In the last part of Chapter 4 we presented an alternative way to manipulate the orbital

ordering in embedded LSMO films [73]. The XAS data showed that it was possible to influence the electronic and structural properties of LSMO films fabricated under same conditions only by tuning the oxygen pressure during the growth of the overlayer oxide BTO. Our data proved that with increasing oxygen pressure existing stoichiometry variations in LSMO films between the bulk and near interface could be reduced [73]. Increasing the oxygen pressure in BTO growth led to a reduction in the non-uniform strain in the LSMO and kept the film ferromagnetic at room temperature. XLD measurements confirmed that the existing Mn^{3+} ions favored an in-plane e_g orbital ordering [73]. Furthermore, our study established that an increase in the oxygen pressure increased the non-uniform strain in BTO, which was visible both in XRD and in XLD data. However, it did not modify drastically the chemical environment of the Ti-ions [73].

In the second part of this work, we used a combination of LEEM and XPEEM technique to explore with high spatial resolution the strain-induced interaction between the BTO single crystals and the ferromagnetic Fe thin films. First, we investigated the BTO(001) ferroelectric domain local electronic structure, which was considered a model perovskite-type ferroelectric oxide with potential for technological applications. AES and LEED showed that the surface was BaO-terminated with a (2x2) reconstruction. We determined a shift in the MEM-LEEM transition between different ferroelectric domains. The LEEM contrast was related to the electrostatic potential differences on the surface. High reflectivity in LEEM was attributed to a small number of empty states at the respective electron kinetic energy [188]. Equally important, in order to study the charge anisotropy with spatial resolution, XAS measurements were performed. We were able to image the ferroelectric domains with the help of performed and calculated XLD spectrum. We found that ferroelectric domains appeared in stripe-form and extended over some microns. The typical ferroelectric domain width was varying from 2 μm to 10 μm for the in-plane domains. The ferroelectric domains were either separated by 180° domain wall or by 90° domain walls depending on the domain variants, c^+ - c^- or a - c domains, respectively. The observed domain configuration was compatible with the literature.

Second, the deposition temperature, and the effect of grazing incidence deposition dependent changes in the electronic properties of the Fe/BTO were studied by XPEEM. The characterization of the Fe growth on BTO was presented and epitaxial Fe thin film magnetic properties were discussed. Surprisingly, we did not find an induced dichroism in the ferromagnetic Fe films grown on different ferroelectric domains present in BTO, when Fe was deposited in front of the PEEM objective lens. At the room temperature a needle-like domain structure was obtained for grazing incidence growth. Magnetic domains of Fe did not couple to the ferroelectric domain structure of the BTO substrate. We observed that independent of the BTO single crystal orientation and the

substrate preparation, the needle-like magnetic domain configuration developed for all the oxide surfaces, as long as we deposited Fe films at room temperature and in front of the objective lens of the microscope. Our further studies showed that an increase in the substrate temperature during deposition suppressed the oblique columnar structure and led to a granular magnetic domain contrast with a size of roughly 80 nm magnetic domains in the plane of the substrate. While Lahtinen *et al.* [25] were only able to see the FM domain-state via Kerr Microscopy, we were able to do a full characterization of both the ferroelectric state (in-plane P^{in} or out-of-plane P^{+}, P^{-}) by LEEM and XLD and the magnetization by XMCD and azimuthal sample rotation. Hereby we were able to better understand the strain-induced magnetostrictive effects in the FM.

In the final part of this work, we presented the influence of oblique-angle deposition on the ferromagnetic domain configuration of the Fe films. We grew Fe films on BTO in the prep-chamber without breaking the vacuum. We succeeded to obtain ferroelectric domain imprinting on the ferromagnetic film. Our finding suggested that we were able to eliminate the potential side-effect such as the influence of the oblique growth which might be the dominant factor affecting the diffusion of Fe atoms on the insulating oxide surface by evaporating Fe in the prep-chamber with an α (inclination angle) smaller than approx. 20°. Lastly, we prepared normal incidence $ex-situ$ iron wedge films on BTO. Magnetoelectric coupling was verified by the XMCD-PEEM measurements. Furthermore we have demonstrated that different magnetic domain patterns occured depending on the Fe film thickness.

Considering BTO/LSMO/STO heterosystems, defect-free epitaxially grown heterostructures are needed. Future research may focus on improving the growth conditions of the BTO films to be able tackle the time- and space-resolved dynamic ferroelectric switching phenomena. Impedance spectroscopy on BTO films can be utilized to analyse the quality of the ferroelectric films in terms of dielectric properties.

To determine the competing magnetic anisotropies in Fe films grown on BTO, Ferromagnetic resonance (FMR) measurements can be performed. Analysis of Fe/BTO systems as a function of temperature would yield quantitative informations on the phase-transition induced changes in the anisotropy constants.

References

[1] The 4th AOFSRR School. *PEEM and Nanoscience*. Cheiron School, October 2010. 1

[2] C. M. Schneider, M. Patt, V. Feyer, C. Wiemann, I. P. Krug, F. Nickel, D. Gottlob, and S. Cramm. Photoelectron Spectronanoscopy - Opportunities and Challenges. In *ISSRNS 2012: Synchrotron Radiation in Natural Science*, 2012. 1

[3] D. I. Khomskii. Multiferroics: Different ways to combine magnetism and ferroelectricity. *J. Magn. Magn. Mater.*, 306:1–8, 2006. 1

[4] W. Huang, S. Yang, and X. Li. Multiferroic heterostructures and tunneling junctions. *Journal of Materiomics*, 1(4):263–284, December 2015. 1

[5] A. H. Dürr and C. M. Schneider. Ultrafast Magnetodynamics with Lateral Resolution: A View by Photoemission Microscopy Ultrafast Magnetodynamics with Lateral Resolution. In Helmut Kronmuller and Stuart Parkin, editors, *Handbook of Magnetism and Advanced Magnetic Materials*, page 3064. Wiley, 2007. 1

[6] T. Becker, C. Streng, Y. Luo, V. Moshnyaga, B. Damaschke, N. Shannon, and K. Samwer. Intrinsic Inhomogeneities in Manganite Thin Films Investigated with Scanning Tunneling Spectroscopy. *Phys. Rev. Lett.*, 89:237203, Nov 2002. 2, 54

[7] B. Cui, C. Song, G.Y. Wang, H.J. Mao, F. Zeng, and F. Pan. Strain engineering induced interfacial self-assembly and intrinsic exchange bias in a manganite perovskite film. *Scientific Reports*, 3:2542, 2013. 2

[8] A. Tebano, C. Aruta, S. Sanna, P. G. Medaglia, G. Balestrino, A. A. Sidorenko, R. De Renzi, G. Ghiringhelli, L. Braicovich, V. Bisogni, and N. B. Brookes. Evidence of Orbital Reconstruction at Interfaces in Ultrathin $La_{0.67}Sr_{0.33}MnO_3$ Films. *Phys. Rev. Lett.*, 100:137401, Apr 2008. 2, 14, 55

[9] M. B. Lepetit, B. Mercey, and C. Simon. Interface Effects in Perovskite Thin Films. *Phys. Rev. Lett.*, 108:087202, Feb 2012. 2

[10] J.-S. Lee, D. A. Arena, P. Yu, C. S. Nelson, R. Fan, C. J. Kinane, S. Langridge, M. D. Rossell, R. Ramesh, and C.-C. Kao. Hidden Magnetic Configuration in Epitaxial $La_{1-x}Sr_xMnO_3$ Films. *Phys. Rev. Lett.*, 105:257204, Dec 2010. 2

[11] S. Majumdar, H. Huhtinen, H. S. Majumdar, and P. Paturi. Stress and defect induced enhanced low field magnetoresistance and dielectric constant in $La_{0.7}Sr_{0.3}MnO_3$ thin films. *Journal of Alloys and Compounds*, 512:332–339, 2012. 2, 51, 76

[12] G. H. Haertling. Ferroelectric Ceramics: History and Technology. *Journal of the American Ceramic Society*, 82(4):797–818, 1999. 2

[13] S. A. Harrington, J. Zhai, S. Denev, V. Gopalan, H. Wang, Z. Bi, S. A. T. Redfern, S. Baek, C. W. Bark, C. B. Eom, Q. Jia, M. E. Vickers, and J. L. MacManus-Driscoll. Thick lead-free ferroelectric films with high Curie temperatures through nanocomposite-induced strain. *Nature Nanotechnology*, 6:491–495, July 2011. 2

[14] K. J. Choi, M. Biegalski, Y. L. Li, A. Sharan, J. Schubert, R. Uecker, P. Reiche, Y. B. Chen, X. Q. Pan, V. Gopalan, L.-Q. Chen, D. G. Schlom, and C. B. Eom. Enhancement of Ferroelectricity in Strained $BaTiO_3$ Thin Films. *Science*, 306(5698):1005–1009, 2004. 2

[15] O. Trithaveesak, J. Schubert, and Ch. Buchal. Ferroelectric properties of epitaxial $BaTiO_3$ thin films and heterostructures on different substrates. *Journal of Applied Physics*, 98(11):–, 2005. 2, 3

[16] B.-F. Ding and S.-Q. Zhou. The coexistence of ferroelectricity and ferromagnetism in Mn-doped $BaTiO_3$ thin films. *Chin. Phys. B*, 20(127701), 2011. 3

[17] A. Petraru, J. Schubert, M. Schmid, and Ch. Buchal. Ferroelectric $BaTiO_3$ thin-film optical waveguide modulators. *Applied Physics Letters*, 81(8):1375–1377, 2002. 3

[18] Y. S. Kim, D. H. Kim, J. D. Kim, Y. J. Chang, T. W. Noh, J. H. Kong, K. Char, Y. D. Park, S. D. Bu, J.-G. Yoon, and J.-S. Chung. Critical thickness of ultrathin ferroelectric $BaTiO_3$ films. *Applied Physics Letters*, 86(10), 2005. 3

[19] J. D. Burton and E. Y. Tsymbal. Prediction of electrically induced magnetic reconstruction at the manganite/ferroelectric interface. *Phys. Rev. B*, 80(174406), 2009. 3

[20] C. A. F. Vaz, J. Hoffman, Y. Segal, J. W. Reiner, R. D. Grober, Z. Zhang, C. H. Ahn, and F. J. Walker. Origin of the magnetoelectric coupling effect in $PbZr_{0.2}Ti_{0.8}O_3/La_{0.8}Sr_{0.2}MnO_3$ multiferroic heterostructures. *Phys. Rev. Lett.*, 104(127202), 2010. 3

[21] R. K. Govind. *Growth, magnetic properties and interface effects of Fe and Fe-oxide ultrathin films on* $BaTiO_3(001)$ *substrates*. PhD thesis, Martin-Luther-Universität Halle-Wittenberg, Germany, 2013. 3, 4, 36, 80, 81, 88, 94, 96, 97, 104

[22] C.-G. Duan, S. S. Jaswal, and E. Y. Tsymbal. Predicted Magnetoelectric Effect in $Fe/BaTiO_3$ Multilayers: Ferroelectric Control of Magnetism. *Phys. Rev. Lett.*, 97(047201), 2006. 3, 22, 81, 94

[23] G. Radaelli, D. Petti, E. Plekhanov, I. Fina, P. Torelli, B. R. Salles, M. Cantoni, C. Rinaldi, D. Gutiérrez, G. Panaccione, M. Varela, S. Picozzi, J. Fontcuberta, and R. Bertacco. Electric control of magnetism at the $Fe/BaTiO_3$ interface. *Nature Communications*, 5, 3 2014. 3

[24] S. Sahoo, S. Polisetty, C.-G. Duan, S. S. Jaswal, E. Y. Tsymbal, and C. Binek. Ferroelectric control of magnetism in $BaTiO_3/Fe$ heterostructures via interface strain coupling. *Phys. Rev. B*, 76(092108), 2007. 3, 112

[25] T. H. E. Lahtinen, J. A. K. Franke, and S. van Dijken. Domain Wall Motion and Local Magnetization Reversal. *Scientific Reports*, 2(258), February 2012. 3, 97, 99, 103, 115

[26] P. Luches, S. Benedetti, A. di Bona, and S. Valeri. Magnetic couplings and exchange bias in Fe/NiO epitaxial layers. *Phys. Rev. B*, 81:054431, Feb 2010. 4

[27] P. Torelli, S. Benedetti, P. Luches, L. Gragnaniello, J. Fujii, and S. Valeri. Morphology-induced magnetic phase transitions in Fe deposits on MgO films investigated with XMCD and STM. *Phys. Rev. B*, 79:035408, Jan 2009. 4

[28] A. Arranz, V. Pérez-Dieste, and C. Palacio. Growth, electronic properties and thermal stability of the Fe/Al_2O_3 interface. *Surface Science*, 521(1-2):77–83, 2002. 4

[29] S. Brivio, C Rinaldi, D Petti, R. Bertacco, and F. Sanchez. Epitaxial growth of $Fe/BaTiO_3$ heterostructures. *Thin Solid Films*, 519(17):5804–5807, June 2011. 4, 94

[30] A. Hubert and R. Schäfer. *Magnetic Domains: The Analysis of Magnetic Microstructures*. Springer-Verlag Berlin Heidelberg, 1998. 5, 7, 15

[31] S. Blundell. *Magnetism in Condensed Matter*. Oxford University Press, Great Clarendon Street, Oxford OX2 6DP, 2001. 6

[32] E. C. Stoner. Proceedings of the Royal Society of London, 1936. 7

[33] P. Poulopoulos, U. Bovensiepen, M. Farle, and K. Baberschke. AC Susceptibility: a sensitive probe of interlayer coupling. *J. Magn. Magn. Mater.*, 212:17–22, 2000. 7

[34] P. Entel. Magnetic interactions in bulk and nanoalloys. Lecture Notes - COST ISNA, 2012. 7

[35] S. Gliga. *Ultrafast vortex core dynamics investigated by finite-element micromagnetic simulations*. PhD thesis, Universität Duisburg Essen, Germany, 2009. 8

[36] C. Kittel. Reviews of Modern Physics, 1949. 10

[37] T. H. E. Lahtinen. *Ferromagnetic- Ferroelectric Domain Coupling in Multiferroic Heterostructures*. PhD thesis, Aalto University, 2013. 9, 16, 18, 19, 20, 21

[38] S. Konings. Domain walls. `https://iop.fnwi.uva.nl/cmp//qem/research_projects/domainwall.html`, February 2016. 11

[39] L. Martin, Y.-H. Chu, and R. Ramesh. Advances in the growth and characterization of magnetic, ferroelectric and multiferroic oxide thin films. *Materials Science and Engineering R*, 68:89–133, 2010. 10

[40] K. Dörr. Ferromagnetic manganites: spin-polarized conduction versus competing interactions. *J. Phys. D: Appl. Phys.*, 39(7):R125–R150, 2006. 10, 11, 12, 13, 14, 72

[41] E. Dagotto. Complexity in Strongly Correlated Electronic Systems. *Science*, 309(5732):257–262, 2005. 10

[42] H. Y. Hwang, Y. Iwasa, M. Kawasaki, N. Nagaosa, and Y. Tokura. Emergent phenomena at oxide interfaces. *Nature Materials*, 11:103–113, January 2012. 10, 13

[43] C. Aruta, G. Balestrino, G. Ghiringhelli, and N. B. Brookes. Cooperative enhancement of in-plane orbital ordering by oxygen deficiency and in-plane tensile strain in $La_{0.66}Sr_{0.33}MnO_{3-\delta}$ thin films. *EPL*, 80(3):37003, 2007. 12, 55, 56, 60, 68, 69, 74

[44] J. Krempaský. *Angle- and spin-resolved photoemission on* $La_{2/3}Sr_{1/3}MnO_3$. PhD thesis, L'université de Cergy-Pontoise, France, 2008. 12, 13

[45] J. M. D. Coey, M. Viret, and S. von Molnar. Mixed-valence manganites. *Adv. Phys.*, 48:167, 1999. 13

[46] M. Cesaria, A. P. Caricato, G. Maruccioa, and M. Martino. LSMO-growing opportunities by PLD and applications in spintronics. *Journal of Physics: Conference Series*, 292, 2010. 13

[47] I. G. Hallsteinsen. Toward Growth Control of (111)-oriented Perovskite Thin Films: $La_{0.7}Sr_{0.3}MnO_3/SrTiO_3(111)$ a model study. Master's thesis, Norwegian University of Science and Technology, Norway, 2012. 13

[48] I. C. Infante. (001) *and* (110) $La_{2/3}Ca_{1/3}MnO_3$ *epitaxial ferromagnetic electrodes: a comperative study.* PhD thesis, Universitat Autonoma de Barcelona, Spain, 2008. 13

[49] C. Zener. Interaction between the d-Shells in the Transition Metals. II. Ferromagnetic Compounds of Manganese with Perovskite Structure. *Phys. Rev.*, 82(403), May 1951. 13

[50] C. Zener. Interaction Between the d Shells in the Transition Metals. *Phys. Rev. B.*, 81(440), February 1951. 13

[51] P. W. Anderson and H. Hasegawa. Considerations on Double Exchange. *Phys. Rev.*, 100:675, 1955. 14

[52] P. G. de Gennes. Effects of Double Exchange in Magnetic Crystals. *Phys. Rev.*, 118:141, April 1960. 14

[53] E. Dagotto, T. Hotta, and A. Morea. Colossal Magnetoresistant Materials: The Key Role of Phase Separation. *Phys. Rep.*, 344:1, 2001. 14

[54] M. Capone, D. Feinberg, and M. Grilli. Stabilization of A-type layered antiferromagnetic phase in $LaMnO_3$ by cooperative Jahn – Teller deformations. *Eur. Phys. J. B*, 17:103–109, 2000. 14

[55] J. B. Goodenough. Theory of the Role of Covalence in the Perovskite-Type Manganites LaM(II)MnO_3. *Phys. Rev.*, 100:564–573, October 1955. 14

[56] M. Atanasov and S. Angelov. Angular overlap model parametrization of Andersons Superexchange Theory. I. A Quantification of Goodenough-Kanamori Rules. *Chem. Phys.*, 150:383, 1991. 14

[57] C. Aruta, G. Ghiringhelli, A. Tebano, N. G. Boggio, N. B. Brookes, P. G. Medaglia, and G. Balestrino. Strain induced x-ray absorption linear dichroism in $La_{0.7}Sr_{0.3}MnO_3$ thin films. *Phys. Rev. B*, 73:235121, Jun 2006. 14, 55

[58] A. J. Millis, P. B. Littlewood, and B. I. Shraiman. Double Exchange Alone Does Not Explain the Resistivity of $La_{1-x}Sr_xMnO_3$. *Phys. Rev. Lett.*, 74:5144–5147, 1995. 14

[59] J. Zang, A. R. Bishop, and H. Röder. Double degeneracy and Jahn-Teller effects in colossal-magnetoresistance perovskites. *Phys. Rev. B.*, 53(R8840 (R)), April 1996. 14

[60] J. M. D. Coey. Materials for Spin Electronics. In *Lecture Notes in Physics*, chapter 12, pages 277–297. Springer-Verlag, June 2007. 15

[61] C. L. Dennis, R. P. Borges, L. D. Buda, U. Ebels, J. F. Gregg, M. Hehn, E. Jouguelet, K. Ounadjela, I. Petej, I. L. Prejbeanu, and M. J. Thornton. The defining length scales of mesomagnetism: A review. *Journal of Physics: Condensed Matter*, 14(49):1175–1262, December 2002. 16

[62] D. M. Gottlob. *Spin reorientation transition in epitaxial* Ni_xPd_{1-x} *films on* Cu(001)*: a microscopic analysis.* PhD thesis, Universität Duisburg Essen, Germany, 2014. 16, 41

[63] K. C. Kao. *Dielectric Phenomena in Solids with Emphasis on Physical Concepts of Electronic Processes.* ISBN:0-12-396561-6. Elsevier Academic Press, 2004. 16

[64] J. Valasek. Piezo-Electric and Allied Phenomena in Rochelle Salt. *Physical Review*, 17(4):475–481, April 1921. 16

[65] R. E. Cohen. Origin of ferroelectricity in perovskite oxides. *Nature*, 358, July 1992. 16, 17

[66] S. H. Wemple and Jr. M. DiDomenico. Behavior of the Electronic Dielectric Constant in Covalent and Ionic Materials. *Phys. Rev. B*, 3(1338), 1970. 16

[67] L. A. Shebanov. X-Ray Temperature Study of Crystallographic Characteristics of Barium Titanate. *Phys. Status Solidi A*, 65(1):321–325, 1981. 17

[68] A. Höfer. *Laser-angeregte Photoemissions-Elektronenmikroskopie an oxidischen Oberfächen.* PhD thesis, Martin-Luther-Universität Halle-Wittenberg, 2012. 18, 81

[69] J. Guyonnet. *Ferroelectric Domain Walls.* PhD thesis, University of Geneva, Geneva, Switzerland, 2014. 18, 19, 20

[70] F. Rubio-Marcos, A. Del Campo, P. Marchet, and J. F. Fernandez. Ferroelectric domain wall motion induced by polarized light. *Nature Communications*, 6(6594), March 2015. 18

[71] A. Boulle, I. C. Infante, and N Lemee. Diffuse X-ray scattering from 180° ferroelectric stripe domains: polarization-induced strain, period disorder and wall roughness. *J. Appl. Cryst.*, 49:845–855, 2016. 20

[72] N. A. Hill. Why Are There so Few Magnetic Ferroelectrics? *J. Phys. Chem. B.*, 104(29):6694–6709, June 2000. 20

[73] H. Doğanay, I. P. Krug, J. Schubert, S. Cramm, D. M. Gottlob, F. Nickel, and C. M. Schneider. Tuning the orbital ordering in $La_{0.7}Sr_{0.3}MnO_3$ thin films in all-oxide hybrids. *EPL*, 109, 2015. 20, 27, 54, 55, 66, 68, 69, 71, 72, 73, 74, 75, 84, 85, 114

[74] M. Fiebig. Revival of the magnetoelectric effect. *Journal of physics D: Applied physics*, 38:R123–R152, 2005. 20

[75] B. D. Cullity and C.D. Graham. *Introduction to Magnetic Materials*. Wiley, 2009. 20, 110, 112

[76] W. Eerenstein, M. Wiora, J. L. Prieto, J. F. Scott, and N. D. Mathur. Giant sharp and persistent converse magnetoelectric effects in multiferroic epitaxial heterostructures. *Nature Materials*, 6:348–351, April 2007. 21

[77] P. Bechtholdt. X-ray absorption spectroscopy. In K. Urban, C. M. Schneider, and T. Brückel, editors, *38th IFF Spring School 2007, Probing the Nanoworld Microscopies, Scattering and Spectroscopies of the Solid State*, number 34. Forschungszentrum Jülich GmbH, 2007. 23

[78] J. J. Rehr and R. C. Albers. Theoretical approaches to x-ray absorption fine structure. *Reviews of Modern Physics*, 72(3):621–654, July 2000. 24

[79] R. Nakajima, J. Stöhr, and Y. U. Idzerda. Electron-yield saturation effects in *L*-edge x-ray magnetic circular dichroism spectra of Fe, Co, and Ni. *Phys. Rev. B*, 59(6421), 1999. 25

[80] F. Kronast. *Magnetic coupling in (GaMn)As ferromagnetic semiconductors - studied by soft x-ray spectroscopy*. PhD thesis, Technische Universität Berlin, Germany, 2006. 25

[81] M. Räkers. *An x-ray spectroscopic study of novel materials for electronic applications*. PhD thesis, University of Osnabrück, Germany, 2009. 25

[82] J. L. Erskine and E. A. Stern. Calculation of the M_{23} magneto-optical absorption spectrum of ferromagnetic nickel. *Phys. Rev. B*, 12:5016–5024, Dec 1975. 25

[83] G. Schütz, W. Wagner, W. Wilhelm, P. Kienle, R. Zeller, R. Frahm, and G. Materlik. Absorption of circularly polarized x-rays in iron. *Phys. Rev. Lett.*, 58:737–740, Feb 1987. 25

[84] C. T. Chen, Y. U. Idzerda, H.-J. Lin, N. V. Smith, G. Meigs, E. Chaban, G. H. Ho, E. Pellegrin, and F. Sette. Experimental Confirmation of the X-Ray Magnetic Circular Dichroism Sum Rules for Iron and Cobalt. *Phys. Rev. Lett.*, 75:152–155, Jul 1995. 25

[85] P. M. Oppeneer, J. Kunes, M. Hecker, C. M. S. Schneider, S. Zotova, and R. Kaltofen. A novel spectroscopy. In *IFW Dresden, Highlights*, 2002. 25

[86] S. Imada, S. Suga, W. Kuch, and J. Kirschner. Magnetic Microspectroscopy by a Combination of XMCD and PEEM. *Surf. Rev. Lett.*, 9(2):877–881, 2002. 25

[87] P. Carra, B. T. Thole, M. Altarelli, and X. Wang. X-ray circular dichroism and local magnetic fields. *Phys. Rev. Lett.*, 70(694), February 1993. 27

[88] J. Stöhr. *Springer Series in Surface Sciences NEXAFS Spectroscopy*. Springer, Berlin, Heidelberg, June 1996. 27, 42

[89] C. Schmitz-Antoniak, D. Schmitz, P. Borisov, F. M. F. de Groot, S. Stienen, A. Warland, B. Krumme, R. Feyerherm, E. Dudzik, W. Kleemann, and H. Wende. Electric in-plane polarization in multiferroic $CoFe_2O_4/BaTiO_3$ nanocomposite tuned by magnetic fields. *Nature Communications*, 4(2051), June 2013. 27, 28, 66

[90] A. Filippetti and N. A. Hill. Coexistence of Magnetism and Ferroelectricity in Perovkites. *Physical Review B*, 65(19), May 2002. 28

[91] D. Schumacher. *Interplay between magnetic and dielectric phenomena at transition metal oxide interfaces*. PhD thesis, RWTH Aachen University, Germany, 2012. 30, 31, 51, 53

[92] Ch. Buchal, L. Beckers, A. Eckau, J. Schubert, and W. Zander. Epitaxial $BaTiO_3$ thin films on MgO. *Materials Science and Engineering: B*, 56:234–238, 1998. 30, 31, 68

[93] B. D. Josephson. The discovery of tunnelling supercurrents. *Reviews of Modern Physics*, 46(2):251, April 1974. 31

[94] Quantum Design. *SQUID Manual*. 110C, Part Number, 1014. 32

[95] H. Doğanay. Electronic Transport and Magnetic Properties of Spin Filter/Semiconductor Heterostructures: EuS/Si(100). Master's thesis, Universität Duisburg Essen, Germany, 2011. 32, 33, 34, 51, 54

[96] S. Bedanta. *Supermagnetism in magnetic nanoparticle systems*. PhD thesis, Universität Duisburg Essen, Germany, 2006. 33

[97] K. Gramm, L. Lundgren, and O. Beckman. SQUID Magnetometer for Mangetization Measurements. *Physica Scripta*, 13(2):93–95, February 1976. 33

[98] P. Ebert. Scanning Probe Microscopy. In *41st IFF Spring School 2010, Electronic Oxides-Correlation Phenomena, Exotic Phases and Novel Functionalities*, volume 13. Forschungszentrum Jülich GmbH, 2010. 33

[99] Basics of atomic force microscope (afm). `http://www.eng.utah.edu/~lzang/images/Lecture_10_AFM.pdf`. Accessed: 2014-10-31. 33

[100] A. Foster. *Theoretical Modeling of Non-contact Atomic Force Microscopy on Insulators*. PhD thesis, University College London, UK, 2000. 34

[101] *Digital Instruments*. Nanoscope Handbook, 1998. 34, 54

[102] B. D. Cullity and S. R. Stock. *Elements of X-ray Diffraction*. Prentice Hall, New Jersey, 2001. 35

[103] A. I. Petraru. *Optical and electro-optical properties of* $BaTiO_3(001)$ *thin films and Mach-Zehnder waveguide modulators*. PhD thesis, Universität zu Köln, Germany, 2003. 35, 36

[104] H. Lüth. *Solid Surfaces, Interfaces and Thin Films*. ISBN 978-3-642-13591-0. Springer, Heidelberg Dordrecht London New York, 5. edition, 2010. 36, 80

[105] M. Müller. *Electronic Structure of Ferromagnet-Insulator Interfaces: Fe/MgO and Co/MgO*. PhD thesis, Universität Duisburg Essen, Germany, 2007. 36

[106] J. Larmor. On the theory of the magnetic influence on spectra; and on the radiation from moving ions. *Phil. Mag.*, 44(271):503–512, 1897. 37

[107] R. V. Langmuir F. R. Elder, A. M. Gurewitsch and H. C. Pollock. Radiation from Electrons in a Synchrotron. *Phys. Rev.*, 71:829–830, June 1947. 37

[108] E. Beaurepaire, H. Bulou, L. Joly, and F. Scheurer, editors. *Synchrotron radiation, polarization, devices and new sources*, Mittelwihr (France), 2012. Proceedings of the 6th International School "Synchrotron Radiation and Magnetism", Springer. 37, 38

[109] W. Eberhardt and W. Schilling. *Synchrotronstrahlung zur Erforschung kondensierter Materie*, volume 23. IFF-Ferienkurs, Vorlesungsmanuskripte. FZ Jülich, 1992. 37

[110] A. Zimina. *Novel Nanomaterials Studied by the Method of Soft X-ray Fluorescence Spectroscopy*. PhD thesis, Technische Universität Berlin, Germany, 2006. 37

[111] D. Attwood. *Soft X-Rays and Extreme Ultraviolet Radiation: Principles and Applications*. Cambridge: Cambridge University Press, 1999. 38

[112] B. Van Waeyenberge, A. Puzic, H. Stoll, K. W. Chou, T. Tyliszczak, R. Hertel, M. Fahnle, H. Bruckl, K. Rott, G. Reiss, I. Neudecker, D. Weiss, C. H. Back, and G. Schutz. Magnetic vortex core reversal by excitation with short bursts of an alternating field. *Nature*, 444(7118):461–464, 11 2006. 38

[113] F. Nickel, D. M. Gottlob, I. P. Krug, H. Doganay, S. Cramm, A. M. Kaiser, G. Lin, D. Makarov, O. G. Schmidt, and C. M. Schneider. Time-Resolved Magnetic Imaging in an Aberration-Corrected, Energy-Filtered Photoemission Electron Microscope. *Ultramicroscopy*, 123:234–234, 2013. 38

[114] A. Balerna and S. Mobilio. *Synchrotron Radiation Basics, Methods and Applications*, chapter 1, pages 3–28. Springer-Verlag, Berlin, Heidelberg, 2015. 39

[115] C. M. Schneider. Photons for Magnetism-Lecture Notes. Universität Duisburg-Essen, 2014. 40

[116] Insertion devices lecture 3 undulator radiation in detail jim clarke astec daresbury laboratory. http://www.cockcroft.ac.uk/education/PG_courses_2009-10/Spring_2010/CLarkeμ~%20Lectureμ~%203.pdf. Accessed: 2014-11-12. 39

[117] S. Cramm. Synchrotron radiation sources and beamlines: Overview. In K. Urban, C. M. Schneider, and T. Brückel, editors, *38th IFF Spring School 2007, Probing the Nanoworld Microscopies, Scattering and Spectroscopies of the Solid State*, volume 34. Forschungszentrum Jülich GmbH, 2007. 39, 41

[118] Advanced Light Source, University of California Berkeley, CA. *ALS Beamline Design Guide*, revision 2 edition, March 1998. 40

[119] O. Seifert. Evaluation of electronic and geometric properties of nanoparticles using XPEEM. In A. Mendez-Vilas and J. Diaz, editors, *Modern Research and Educational Topics in Microscopy*, volume 2 of *Formatex microscopy series*. Badajoz, Spain: Formatex, 2007. 42

[120] R. M. Tromp, J. B. Hannon, W. Wan, A. Berghaus, and O. Schaff. A New Aberration-Corrected, Energy-Filtered LEEM/PEEM Instrument II. Operation and Results. *Ultramicroscopy*, 127:25–39, April 2013. 44, 46

[121] S. Cherifi. LEEM and Spin-Polarized LEEM. In K. Urban, C. M. Schneider, and T. Brückel, editors, *38th IFF Spring School 2007, Probing the Nanoworld Microscopies, Scattering and Spectroscopies of the Solid State*, volume 34. Forschungszentrum Juelich GmbH, 2007. 45, 46

[122] N. Barrett, J. E. Rault, J. L. Wang, C. Mathieu, A. Locatelli, T. O. Mentes, M. A. Nino, S. Fusil, M. Bibes, A. Barthelemy, D. Sando, W. Ren, S. Prosandeev, L. Bellaiche, B. Vilquin, A. Petraru, I. P. Krug, and C. M. Schneider. Full field electron spectromicroscopy applied to ferroelectric materials. *J. Appl. Phys.*, 113(187217), 2013. 46, 47, 66, 81

[123] J. Dionot. *Topology of ferroelectric polarization at the* $BaTiO_3(001)$ *surface from ab initio calculations and electron microscopy-spectroscopy*. PhD thesis, Université Paris-Süd, December 2015. 46

[124] W. Kuch. Magnetic Imaging. In *IVth International School on Magnetism and Synchrotron Radiation in Mittelwihr (France)*, volume 697, pages 275–320. Springer, Berlin, Heidelberg, 2006. 47, 48

[125] M. Kawasaki, K. Takahashi, T. Maeda, R. Tsuchiya, M. Shinohara, O. Ishiyama, T. Yonezawa, M. Yoshimoto, and H. Koinuma. Atomic Control of the $SrTiO_3$ Crystal Surface. *Science*, 266(1540), 1994. 49

[126] G. Koster, G. Rijnders, D. H. A. Blank, and H. Rogalla. Surface morphology determined by (001) single-crystal $SrTiO_3$ termination. *Physica C: Superconductivity*, 339(215), 2000. 49

[127] H. F. Li, Y. Su, J. Persson, P. Meuels, J. M. Walter, R. Skowronek, and T.. Brückel. Neutron-diffraction study of structural transition and magnetic order in orthorhombic and rhombohedral $La_{7/8}Sr_{1/8}Mn_{1\gamma}O_{3+\delta}$. *J. Phys: Condens. Mat.*, 19(17), 2007. 51

[128] H. L. Ju and H. Sohn. Magnetic inhomogeneity and colossal magnetoresistance in manganese oxides. *J. Magn. Magn. Mater.*, 167(3):200–208, 1997. 51, 52, 61

[129] Z. Fu-Chang, C. Wei-Ran, G. Wei-Zhi, X. Bo, Q. Xiang-Gang, and Z. Bai-Ru. Spin-glass-like behaviour and positive magnetoresistance in oxygen deficient $La_{2/3}Ca_{1/3}MnO_3$ thin films. *Chinese Phys.*, 13(5):783–788, 2004. 51, 52

[130] J. Y. Yang, J. H. Kim, J. S. Lee, S. J. Woo, J. S. Kwak, J. P. Hong, and M. H. Jung. Inverted hysteresis loops observed in a randomly distributed cobalt nanoparticle system. *Phys. Rev. B*, 78(5):094415, September 2008. 53

[131] M. Ziese, I. Vrejoiu, and D. Hesse. Inverted hysteresis and giant exchange bias in $La_{0.7}Sr_{0.3}MnO_3/SrRuO_3$ superlattices. *Appl. Phys. Lett.*, 97(052504), 2010. 53

[132] H. Schraknepper, C. Bäumer, R. Dittmann, and R. A. De Souza. Complex behaviour of vacancy point-defects in $SrRuO_3$ thin films. *Phys.Chem.Chem.Phys.*, 17:1060, 2015. 53

[133] D. Pesquera, G. Herranz, A. Barla, E. Pellegrin, F. Bondino, E. Magnano, F. Sánchez, and J. Fontcuberta. Surface symmetry-breaking and strain effects on orbital occupancy in transition metal perovskite epitaxial films. *Nature Communications*, 3(1189), November 2012. 55

[134] D. J. Huang, W. B. Wu, G. Y. Guo, H.-J. Lin, T. Y. Hou, C. F. Chang, C. T. Chen, A. Fujimori, T. Kimura, H. B. Huang, A. Tanaka, and T. Jo. Orbital Ordering in $La_{0.5}Sr_{1.5}MnO_4$ Studied by Soft X-Ray Linear Dichroism. *Phys. Rev. Lett.*, 92(087202), February 2004. 55

[135] H. Wu, C. F. Chang, O. Schumann, Z. Hu, J. C. Cezar, T. Burnus, N. Hollmann, N. B. Brookes, A. Tanaka, M. Braden, L. H. Tjeng, and D. I. Khomskii. Orbital order in $La_{0.5}Sr_{1.5}MnO_4$: Beyond a common local Jahn-Teller picture. *Phys. Rev. B*, 84(155126), October 2011. 55

[136] A. K. Pradhan, D. Hunter, T. Williams, B. Lasley-Hunter, R. Bah, H. Mustafa, R. Rakhimov, J. Zhang, D. J. Sellmyer, E. E. Carpenter, D. R. Sahu, and J.-L. Huang. Magnetic properties of $La_{0.6}Sr_{0.4}MnO_3$ thin films on $SrTiO_3$ and buffered Si substrates with varying thickness. *J. Appl. Phys.*, 103(023914), November 2008. 56, 58, 60

[137] H. Guo, D. Sun, W. Wang, Z. Gai, I. Kravchenko, J. Shao, L. Jiang, T. Z. Ward, P. C. Snijders, L. Yin, J. Shen, and X. Xu. Growth diagram of $La_{0.7}Sr_{0.3}MnO_3$ thin films using pulsed laser deposition. *J. Appl. Phys.*, 113(234301), May 2013. 56, 57, 59

[138] D. B. Chrishey and G. K. Hubler. *Pulse Laser Depostion of Thin Films*. Wiley-Interscience, 1994. 57

[139] M. N. R. Ashfold, F. Claeyssens, G. M. Fuge, and S. J. Henley. Pulsed laser ablation and deposition of thin films. *Chem. Soc. Rev.*, 33(1):23–31, 2004. 57

[140] S. K. Sinha, R. Bhattacharya, S. K. Ray, and I. Manna. Influence of deposition temperature on structure and morphology of nanostructured SnO_2 films synthesized by pulsed laser deposition. *Materials Letters*, 65(2):146–149, 2011. 57

[141] P. M. Leufke, A. K. Mishra, A. Beck, D. Wang, C. Kübel, R. Kruk, and H. Hahn. Large-distance rf- and dc-sputtering of epitaxial $La_{1-x}Sr_xMnO_3$ thin films. *Thin Solid Films*, 520(17):5521–5527, 2012. 57

[142] M. Kareev, S. Prosandeev, B. Gray, J. Liu, P. Ryan, A. Kareev, E. Ju Moon, and J. Chakhalian. Sub-monolayer nucleation and growth of complex oxides at high supersaturation and rapid flux modulation. *J. Appl. Phys.*, 109(114303), 2011. 59

[143] Y. K. V. Reddy. *Synthesis and characterization of* $BaTiO_3$ *and* $SrTiO_3$ *thin film capacitors with* RuO_2 *electrodes*. PhD thesis, Universität Duisburg Essen, May 2006. 60, 76

[144] M. Huijben, L. W. Martin, Y.-H. Chu, M. B. Holcomb, P. Yu, G. Rijnders, D. H. A. Blank, and R. Ramesh. Critical thickness and orbital ordering in ultrathin $La_{0.7}Sr_{0.3}MnO_3$ films. *Phys. Rev. B*, 78(7):094413, September 2008. 60, 76

[145] H. L. Ju, J. Gopalakrishnan, J. L. Peng, Qi Li, G. C. Xiong, T. Venkatesan, and R. L. Greene. Dependence of giant magnetoresistance on oxygen stoichiometry and magnetization in polycrystalline $La_{0.67}Ba_{0.33}MnO_z$. *Phys. Rev. B*, 51(9):6143–6146, March 1995. 60

[146] D. C. Worledge, G. J. Snyder, M. R. Beasley, T. H. Geballe, R. Hiskes, and S. DiCarolis. Anneal-tunable Curie temperature and transport of $La_{0.67}Ca_{0.33}MnO_3$. *J. Appl. Phys.*, 80(9):5158–5161, 1996. 60

[147] Y. S. Du, B. Wang, T. Li, D. B. Yu, and H. Yan. Effects of annealing procedures on the structural and magnetic properties of epitaxial $La_{0.7}Sr_{0.3}MnO_3$ films. *J. Magn. Magn. Mater.*, 297:88–92, 2006. 60

[148] A. M. De Léon-Guevara, P. Berthet, J. Berthon, F. Millot, A. Revcolevschi, A. Anane, C. Dupas, K. Le Dang, J. P. Renard, and P. Veillet. Influence of controlled oxygen vacancies on the magnetotransport and magnetostructural phenomena in $La_{0.85}Sr_{0.15}MnO_{3-\delta}$ single crystals. *Phys. Rev. B*, 56(6031), September 1997. 61

[149] S. Nemsak, May 2016. priv. communication. 61

[150] Y.P. Liu, Y.S. Du, M. Zhang, H. Yan, and Y.Y. Wang. Effect of internal strain on magnetic properties of $La_{0.7}Sr_{0.3}MnO_3$ films. *Vacuum*, 81(7):826–829, 2007. 62

[151] A. Morelli, S. Venkatesan, G. Palasantzas, B. J. Kooi, and J. Th. M. De Hosson. Polarization retention loss in $PbTiO_3$ ferroelectric films due to leakage currents. *J. Appl. Phys.*, 102(084103), 2007. 62, 66, 68, 76

[152] A. L. Roytburd, S. P. Alpay, L. A. Bendersky, V. Nagarajan, and R. Ramesh. Three-domain architecture of stress-free epitaxial ferroelectric films. *J. Appl. Phys.*, 89(1), 2001. 66, 107, 108

[153] F. M. F. de Groot, J. C. Fuggle, B. T. Thole, and G. A. Sawatzky. $2p$ x-ray absorption of $3d$ transition-metal compounds: An atomic multiplet description including the crystal field. *Phys. Rev. B*, 42(5459), September 1990. 67, 72, 86

[154] E. Arenholz, G. van der Laan, A. Fraile-Rodríguez, P. Yu, Q. He, and R. Ramesh. Probing ferroelectricity in $PbZr_{0.2}Ti_{0.8}O_3$ with polarized soft x rays. *Phys. Rev. B*, 82(140103), October 2010. 67, 86, 87

[155] F. M. F. de Groot. Multiplet effects in X-ray spectroscopy. *Coordination Chemistry Reviews*, 249:31–63, 2005. 67, 86

[156] H. Salehi, N. Shahtahmasebi, and S. M. Hosseini. Band structure of tetragonal $BaTiO_3$. *Eur. Phys. J. B.*, 32:177–180, 2003. 69

[157] I. P. Krug, June 2016. priv. communication. 70

[158] S. H. Park, I. H. Oh, S. Park, Y. Park, J. H. H. Kim, and Y. D. Huh. Canted antiferromagnetism and spin reorientation transition in layered inorganic-organic perovskite $(C_6H_5CH_2CH_2NH_3)2MnCl_4$. *Dalton Trans.*, 41:1237–1242, 2012. 72

[159] K. Chahara, T. Ohno, M. Kasai, and Y. Kozono. Magnetoresistance in magnetic manganese oxide with intrinsic antiferromagnetic spin structure. *Appl. Phys. Lett.*, 63(1990), 1993. 72

[160] G. F. Dionne, editor. *Magnetic Oxides*. New York, Dordrecht, Heidelberg, London, 2009. 74

[161] M. Fechner, I. V. Maznichenko, S. Ostanin, A. Ernst, J. Henk, and I. Bruno, P. Mertig. Magnetic phase transition in two-phase multiferroics predicted from first principles. *Phys. Rev. B*, 78(212406), 2008. 81

[162] J. Wang. *Modifications of the chemical and electronic ferroelectric surface structure under water adsorption.* PhD thesis, L' Universite Pierre et Marie Curie, France, 2013. 81, 82

[163] A. Gruverman, B. J. Rodriguez, R. J. Nemanich, and A. I. Kingon. Nanoscale observation of photoinduced domain pinning and investigation of imprint behavior in ferroelectric thin films. *J. Appl. Phys.*, 92(2734), 2002. 81

[164] S. V. Kalinin and D. A. Bonnell. Local potential and polarization screening on ferroelectric surfaces. *Phys. Rev. B*, 63(125411), March 2001. 81

[165] R. Shao, M. P. Nikiforov, and D. A. Bonnell. Photoinduced charge dynamics on $BaTiO_3$(001) surface characterized by scanning probe microscopy. *Appl. Phys. Lett.*, 89(112904), 2006. 81, 83, 84

[166] J. L. Wang, B. Vilquin, and N. Barrett. Screening of ferroelectric domains on $BaTiO_3$(001) surface by ultraviolet photo-induced charge and dissociative water adsorption. *Appl. Phys. Lett.*, 101(092902), 2012. 82, 84

[167] D. Y. He, L. J. Qiao, Alex A. Volinsky, Y. Bai, and L. Q. Guo. Electric field and surface charge effects on ferroelectric domain dynamics in $BaTiO_3$ single crystal. *Phys. Rev. B*, 84(024101), 2011. 82

[168] St. Borek. *Magnetooptische und magnetische Eigenschaften zweikomponentiger Multiferroika.* PhD thesis, Martin-Luther-Universität Halle-Wittenberg, 2013. 84, 86

[169] P. W. Forsbergh. Domain Structures and Phase Tansitions in Barium Titanate. *Phys. Rev.*, 76(1187), October 1949. 87

[170] H. Ohldag. *Exchange Coupling of Co and Fe on Antiferromagnetic NiO Investigated By Dichroism X-Ray Absorption Spectromicroscopy.* PhD thesis, Heinrich-Heine Universität Düsseldorf, 2003. 87

[171] R. V. Chopdekar, V. K. Malik, A. Fraile-Rodriguez, L. Le Guyader, A. Takamura, Y.and Scholl, D. Stender, C. W. Schneider, C. Bernhard, F. Nolting, and L. J. Heyderman. Spatially resolved strain-imprinted magnetic states in an artificial multiferroic. *Physics*, 86(1)(014408), 2012. 87, 97

[172] St. Borek, I. V. Maznichenko, G. Fischer, W. Hergert, I. Mertig, A. Ernst, S. Ostanin, and A. Chassé. First-principles calculation of x-ray absorption spectra and x-ray magnetic circular dichroism of ultrathin Fe films on $BaTiO_3$(001). *Phys. Rev. B*, 85(134432), April 2012. 87, 93, 94

[173] E. Arveux. *Surface and Interface Properties of* $BaTiO_3$ *Ferroelectric Thin Films Studied by In-situ Photoemission Spectroscopy.* PhD thesis, L'université de Bordeaux, 2010. 89, 92, 93

[174] J. Wang. *Low Energy Electron Diffraction Studies of Transition Metal Oxide Surfaces and Films.* PhD thesis, Martin-Luther-Universität Halle-Wittenberg, February 2005. 89

[175] K. Szot, W. Speier, U. Breuer, R. Meyer, J. Szade, and R. Waser. Formation of Micro-crystals on the (100) surface of $SrTiO_3$ at elevated temperatures. *Surf. Sci.*, 460:112–128, July 2000. 92, 93

[176] A. Quesada, M. Monti, I. P. Krug, N. Rougemaille, F. Nickel, D. M. Gottlob, H. Doganay, A. T. N'Diaye, G. Chen, A. Serrano, K. F. McCarty, J. F. Fernandez, C. M. Schneider, A. K. Schmid, and J. de la Figuera. Reversible temperature-driven domain transition in bistable Fe magnetic nanostrips grown on Ru(0001). *Phys. Rev. B*, 92(024416), 2015. 96

[177] D. R. Lide, editor. *Handbook of Chemistry and Physics.* CRC Press, 84th edition, October 2003. 96

[178] T. H. E. Lahtinen, J. O. Tuomi, and S. van Dijken. Pattern Transfer and Electric-Field Induced Magnetic Domain Formation in Multiferroic Heterostructures. *Advanced Materials*, 23:3187–3191, September 2011. 97, 99, 103

[179] H. van Kranenburg and C. Lodder. Tailoring growth and local composition by oblique-incidence deposition: a review and new experimental data. *Materials Science and Engineering: R: Reports*, 11(7):295–354, 1994. 100, 101, 102

[180] S. R. Spurgeon. *Correlating Interfacial Structure and Magnetism in Thin-Film Oxide Heterostructures Using Transmission Electron Microscopy and Polarized Neutron Reflectometry.* PhD thesis, Drexel University, October 2014. 102

[181] C. Martinez Boubeta, J. L. Costa-Kraemer, and A. Ceballada. Epitaxy, magnetic and tunnel properties of transition metal/MgO(001) heterostructures. *J. Phys: Condens. Mat.*, 15:R1123–R1167, 2003. 104

[182] A. Barranco, A. Borras, A. R. Ganzalez-Elipe, and A. Palmero. Perspectives on oblique angle deposition of thin films: From fundamentals to devices. *Progress in Materials Science*, 76:59–153, 2016. 105

[183] T. G. Knorr and R. W. Hoffman. Dependence of geometric magnetic anisotropy in thin Fe films. *Physical Review*, 116(6), February 1959. 106

[184] D. O Smith, M. S. Cohen, and G. P. Weiss. Oblique-incidence anisotropy in evaporated permalloy films. *J. Appl. Phys.*, 31:1755–1762, 1960. 106

[185] Z. Ali. Growth, Transport, and Magnetic Properties of Oblique-Angle-Deposited Permalloy Thin Films. Master's thesis, Miami University, August 2018. 106

[186] T. H. E. Lahtinen, Y Shirahata, L Yao, Kevin J. A. Franke, G Venkataiah, T Taniyama, and S van Dijken. Alternating domains with uniaxial and biaxial magnetic anisotropy in epitaxial Fe films on $BaTiO_3$. *Appl. Phys. Lett.*, 101(262405), December 2012. 106, 108, 112

[187] G. Arlt and P. Sasko. Domain Configuration and Equilibrium Size of Domains in $BaTiO_3$ Ceramics. *J. Appl. Phys.*, 51:4956–4960, 1980. 108, 109

[188] J. Schaab, I. P. Krug, H. Doğanay, J. Hackl, D. M. Gottlob, M. I. Khan, S. Nemsak, L. Maurel, E. Langenberg, P. A. Algarabel, J. A. Pardo, C. M. Schneider, and D. Meier. Contact-free mapping of electronic transport phenomena of polar domains in $SrMnO_3$ films. *Phys. Rev. Applied*, 5:054009, May 2016. 114

Chapter 7

Appendix

7.1 Curriculum Vitae

Personal Data

Name: Hatice Gökdemir
Date of birth: 3. September 1985
Place of birth: Istanbul, Turkey
Nationality: Turkish
E-mail address: haticedoganay1054@gmail.com

Education

2011 – 2015 Ph.D. in Physics Peter Grünberg Institute-6, Forschungszentrum Jülich, Jülich, Germany
2009 – 2011 M.Sc. in Physics Universität Duisburg-Essen, Duisburg, Germany
2007 – 2008 Erasmus Program Exchange student at the Universität Duisburg-Essen, Duisburg, Germany
2003 – 2008 B.Sc. in Physics Sakarya University, Sakarya, Turkey

Work Experience

2020 – Akcoat Advanced Chemicals and Coating Materials/ R&D Section Manager
2015 – 2020 Mutlu Batteries / R&D Executive
2010 – 2015 Forschungszentrum Jülich GmbH / Peter Grünberg Institute-6 / Researcher

Hatice Gökdemir

7.2 Publications

- F. Nickel, D. M. Gottlob, I. P. Krug, **H. Doganay**, S. Cramm, A.M. Kaiser, G. Lin, D. Makarov, O.G. Schmidt, and C.M. Schneider, "Time-resolved magnetic imaging in an aberration corrected, energy-filtered photoemission electron microscope", Ultramicroscopy 03/2013; doi:10.1016/j.ultramic.2013.03.005

- J. Schaab, I. P. Krug, F. Nickel, D. M. Gottlob, **H. Doğanay**, A. Cano, M. Hentschel, Z. Yan, E. Bourret, C. M. Schneider, R. Ramesh, and D. Meier, "Imaging and characterization of conducting ferroelectric domain walls photoemission electron microscopy", Applied Physics Letters 104, 232904 (2014)

- **H. Doğanay**, I. Krug, J. Schubert, S. Cramm, D. Gottlob, F. Nickel, and C. M. Schneider "Tuning the orbital ordering in $La_{0.7}Sr_{0.3}MnO_3$ thin films in all-oxide hybrids", EPL 109, 67007 (2015)

- D. Gottlob, **H. Doğanay**, F. Nickel, I. Krug, S. Cramm, and C. M. Schneider, "Microscopic analysis of the composition driven spin-reorientation transition in $Ni_xPd_{1-x}/Cu(001)$", Ultramicroscopy 06/2015; doi:10.1016/j.ultramic.2015.05.22

- A. Quesada, M. Monti, I.P. Krug, N. Rougemaille, F. Nickel, D.M. Gottlob, **H. Doganay**, A.T. NDiaye, G. Chen, A. Serrano, K.F. McCarty, J.F. Fernndez, C.M. Schneider, A.KSchmid and J. de la Figuera Reversible temperature-driven domain transition in bistable nanomagnet, Physical Review B 92, 024416 (2015)

- J. Schaab, I. P. Krug, **H. Doğanay**, J. Hackl, D. M. Gottlob, M. I. Khan, S. Nemk, L. Maurel, E. Langenberg, P. A. Algarabel, J. A. Pardo, C. M. Schneider, and D. Meier, Contact-Free Mapping of Electronic Transport Phenomena of Polar Domains in $SrMnO_3$ Films Physical Review Applied 5, 054009 (2016)

- I. P. Krug, **H. Doganay**, F. Nickel, D. M. Gottlob, C. M. Schneider, A. Morelli, D. Preziosi, I. Lindfors-Vrejoiu, R. Laskowski, and N. Barrett Interface-mediated ferroelectric patterning and Mn valency in nano-structured $PbTiO_3/La_{0.7}Sr_{0.3}MnO_3$ Journal of Applied Physics 120, 095304 (2016); doi:10.1063/1.4962007

- J. A. Mundy, J. Schaab , Y. Kumagai, A. Cano, M. Stengel, I. P. Krug, D. M. Gottlob, **H. Doğanay**, M. E. Holtz, R. Held, Z. Yan, E. Bourret, C. M. Schneider, D. G. Schlom, D. A. Muller, R. Ramesh, N. A. Spaldin and D. Meier, Functional electronic inversion layers at ferroelectric domain walls, Nature Materials DOI: 10.1038/NMAT4878 (2017)

- N. Zingsem, F. Ahrend, S. Vock, D. Gottlob, I. Krug, **H. Doganay**, D. Holzinger, V. Neu, A. Ehresmann, "Magnetic Charge Distribution and Stray Field Landscape of Asymmetric Neel Walls in a magnetically patterned Exchange Bias Layer System", J. Phys. D: Appl. Phys. (50) 495006 (2017)

- A. Gaul, D. Emmrich, T. Ueltzhöffer, H. Huckfeldt, **H. Doğanay**, J. Hackl, M. I. Khan, D. M. Gottlob, G. Hartmann, A. Beyer, D. Holzinger, S. Nemsak, C. M. Schneider, A. Gölzhäuser, G. Reiss and A. Ehresmann," Size limits of magnetic-domain engineering in continuous in-plane exchange-bias prototype films", J. Nanotechnol. 2018, 9, 2968 − 2979. doi:10.3762/bjnano.9.276

- M. I. Khan, S. Cramm, D. Bürgler, U. Parlak, S. Nemsak, D. M. Gottlob, J. Hackl, **H. Doğanay**, C. M. Schneider, "Current-induced domain wall oscillations in a nanowire imaged by time-resolved photoemission electron microscopy", Journal of Magnetism and Magnetic Materials, Volume 476, doi:10.1016/j.jmmm.2019.01.003. (2019)

7.3 Conference Contributions

- **H. Doganay**, I.P. Krug, J. Schubert, D. Gottlob, F. Nickel S. Cramm, and C.M. Schneider, Characterizations of Artificial Multiferroics: $SrTiO_3/LaSrMnO_3/BaTiO_3$, 505. WE-Heraeus- Seminar New Routes to Single-Phase Multiferroics, Bad-Honnef, Bonn, Germany, 23.-25. April 2012 **(poster)**

- **H. Doganay**, I.P. Krug, J. Schubert, D. Gottlob, F. Nickel S. Cramm, and C.M. Schneider, XAS Studies on All-Oxide Ferromagnetic/Ferroelectric Heterosystems: $SrTiO_3/La_{0.7}Sr_{0.3}MnO_3/BaTiO_3$, VIth Mittelwihr International School on Magnetism and Synchrotron Radiation, Mittelwihr, France, 14.-19. October 2012 **(poster)**

- I.P. Krug, I. Vrejoiu, A. Morelli, F. Nickel, D. Gottlob, **H. Doganay**, N. Barrett, J. Wang, and C.M. Schneider, Ferroeletrically induced valency change in multiferroic $PbTiO_3/La_{0.7}Sr_{0.3}MnO_3/BaTiO_3$ nanotructure arrays, LEEM-PEEM 8, Hong-Kong, 11.-15. November 2012 **(talk)**

- D.M. Gottlob, I.P. Krug, F. Nickel, **H. Doganay**, S. Cramm, and C.M. Schneider, On the micromagnetic origin of the spin-reorientation transition in Ni_xPd_{1-x} alloys, BESSY User Meeting, Berlin, Deutschland, 12.-14. December 2012 **(poster)**

- F. Nickel, I.P. Krug, D.M. Gottlob, A.M. Kaiser, D. Makarov, G. Lin, S. Cramm, **H. Doganay**, O.G. Schmidt, and C.M. Schneider, Time-resolved Magnetic Imaging in an Energy-Filtered, Aberration-corrected Photoemision Electron Microscope, BESSY User Meeting, Berlin, Deutschland, 12.-14. December 2012 **(poster)**

- **H. Doganay**, I.P. Krug, J. Schubert, D. Gottlob, F. Nickel S. Cramm, and C.M. Schneider, XAS Studies on All-Oxide Ferromagnetic/Ferroelectric Heterosystems: $SrTiO_3/La_{0.7}Sr_{0.3}MnO_3/BaTiO_3$, BESSY User Meeting, Berlin, Deutschland, 12.-14. December 2012 **(poster)**

- D.M. Gottlob, I.P. Krug, F. Nickel, **H. Doganay**, S. Cramm, and C.M. Schneider, On the micromagnetic origin of the spin-reorientation transition in Ni_xPd_{1-x} alloys, Frhjahrstagung der DPG, Regensburg, Deutschland, 10.-15. March 2013 **(poster)**

- I.P. Krug, I. Vrejoiu, A. Morelli, F. Nickel, D.M. Gottlob, **H. Doganay**, R. Laskowski, N. Barrett, J. Wang, and C.M. Schneider, Tunable ferroelectric imprint and Mn valency in PbTiO3 /La0.7Sr0.3MnO3 nanostructures, Frhjahrstagung der DPG, Regensburg, Deutschland, 10.-15. March 2013 **(poster)**

- F. Nickel, I.P. Krug, D.M. Gottlob, A.M. Kaiser, D. Makarov, G. Lin, S. Cramm, **H. Doganay**, O.G. Schmidt, and C.M. Schneider, Time-resolved Magnetic Imaging in an Energy-Filtered, Aberration-corrected Photoemision Electron Microscope, Frhjahrstagung der DPG, Regensburg, Deutschland, 10.-15. March 2013 **(poster)**

- **H. Doganay**, I.P. Krug, J. Schubert, D. Gottlob, F. Nickel S. Cramm, and C.M. Schneider, XAS Studies on All-Oxide Ferromagnetic/Ferroelectric Heterosystems: SrTiO3/La0.7Sr0.3MnO3/BaTiO3, Frhjahrstagung der DPG, Regensburg, Deutschland, 10.-15. March 2013 **(talk)**

- **H. Doganay**, I.P. Krug, J. Schubert, D. Gottlob, F. Nickel S. Cramm, and C.M. Schneider, Manipulation of Orbital Ordering of La0.7Sr0.3MnO3/BaTiO3 Thin Films in All-Oxide Hybrids, 3rd International TAC LSUM, Ankara, Turkey, October 5.-7. 2013 **(poster)**

- **H. Doganay**, I.P. Krug, D. Gottlob, S. Cramm, and C.M. Schneider, A combined LEEM/PEEM study on ferroelectric domains in perovskite crystals, Frhjahrstagung der DPG, Dresden, Deutschland, 30.March- 4.April 2014 **(talk)**

- D.M. Gottlob, **H. Doganay**, F. Nickel, S. Cramm, I.P. Krug, and C.M. Schneider, Domain orientation in the vicinity of the spin-reorientation transition in

Ni_xPd_{1-x}/Cu(001), LEEMPEEM Conference 9, Berlin, Germany, 14.-18. September 2014 **(poster)**

- **H. Doganay**, I.P. Krug, D. Gottlob, S. Cramm, and C.M. Schneider,, Berlin, Germany, Interplay between ferroelectricity and magnetostrictive behavior in artificial $BaTiO_3$(001)/Fe multiferroics, LEEM-PEEM Conference 9, Berlin, Germany, 14.-18. September 2014 **(poster)**
- D. Gottlob, **H. Doganay**, I.P. Krug, F. Nickel, S. Cramm, and C.M. Schneider Microscopy studies on magnetization (dynamics) and ferroelectricity at the FZ Jülich LEEM/PEEM endstation at BESSY-II, SNI 2014, Bonn, Germany September 21.-23. 2014, **(poster)**
- **H. Doganay**, I. Krug, D. Gottlob, S. Cramm, J. Hackl, M. I. Khan, S. Nemsak, C. M. Schneider, A combined LEEM/PEEM study on ferroelectric/ferromagnetic hybrids: $BaTiO_3$(001)/Fe, BESSY User Meeting, Berlin, Deutschland, 4. December 2014 **(poster)**
- **H. Doganay**, Ferroelectrics, on the way to be seen by low energy electrons, BESSY User Meeting, Berlin, Deutschland, 5. December 2014 **(invited talk)**
- **H. Doganay**, Magnetoelectric Coupling Phenomena on Ferromagnetic/Ferroelectric Hybrids, Physics Seminar, Sakarya University Physics Department, Sakarya, Turkey, 19. December 2014 **(invited talk)**
- D.M. Gottlob, **H. Doganay**, F. Nickel, S. Cramm, I.P. Krug, and C.M. Schneider, Domain orientation in the vicinity of the spin-reorientation transition in Ni_xPd_{1-x}/Cu(001), Frhjahrstagung der DPG, Berlin, Deutschland, 15. - 20. March 2015 **(talk)**
- A. A. Ünal, A. Parabas, Y. Aleksandrov, **H. Doganay**, F. Kronast, and F. Yildiz, Microscopic investigation of laser-induced ferromagnetic domain formation in FeRh thin films and microstructures, Frhjahrstagung der DPG, Berlin, Deutschland, 15. - 20. March 2015 **(poster)**
- Alexander Gaul, Daniel Emmrich, Andr Beyer, Johanna Hackl, **H. Doganay**, Timo Kuschel, Andreas Hütten, Günter Reiss, Slavo Nemsak, Armin Gölzhäuser, and Arno Ehresmann, Light-ion bombardment induced magnetic patterning (IBMP) of exchange bias layer systems by He-ion microscope, Frhjahrstagung der DPG, Berlin, Deutschland, 15. - 20. March 2015 **(poster)**
- **H. Doganay**, I. Krug, J. Schubert, S. Cramm, D. Gottlob, F. Nickel, and C. M. Schneider, Tuning the orbital ordering in $La_{0.7}Sr_{0.3}MnO_3$ thin films in all-oxide hybrids, 1st Benim-Yolum Network Workshop 24.- 26 June 2015 **(poster)**

Band / Volume 244
Molecular Layer Functionalized Neuroelectronic Interfaces:
From Sub-Nanometer Molecular Surface Functionalization to
Improved Mechanical and Electronic Cell-Chip Coupling
N. R. Wolf (2021), IV, 101, xx pp
ISBN: 978-3-95806-570-3

Band / Volume 245
Surface Acoustic Waves in Strain-Engineered Thin (K,Na)NbO_3 Films:
From Basic Research to Application in Molecular Sensing
S. Liang (2021), VI, 125 pp
ISBN: 978-3-95806-571-0

Band / Volume 246
Tailoring neuroelectronic interfaces via combinations of oxides and molecular layers
X. Yuan (2021), 113 pp
ISBN: 978-3-95806-572-7

Band / Volume 247
Stoichiometric control and magnetoelectric coupling in artificial multiferroic heterostructures
P. Schöffmann (2021), vii, 176 pp
ISBN: 978-3-95806-575-8

Band / Volume 248
A Unified Framework for Functional Renormalisation Group Calculations and its Application to Three Dimensional Hubbard Models
J. Ehrlich (2021), xvi, 213 pp
ISBN: 978-3-95806-582-6

Band / Volume 249
Photoemission electron microscopy of magneto-ionic effects in $La_{0.7}Sr_{0.3}MnO_3$
M. Wilhelm (2021), 134 pp
ISBN: 978-3-95806-592-5

Band / Volume 250
Development of a Multiplexer System and Measurement of the Neutron Yield for a Low-Energy Accelerator-Driven Neutron Source
M. Rimmler (2021), v, 200 pp
ISBN: 978-3-95806-600-7

Band / Volume 251
Resolving interface effects in voltage controlled magnetic heterostructures using advanced neutron scattering and electron microscopy methods
T. Bhatnagar-Schöffmann (2021), ix, 171 pp
ISBN: 978-3-95806-604-5

Band / Volume 252
Strain development of *Gluconobacter oxydans* and *Pseudomonas putida* for production of the sweetener 5-ketofructose
K. Wohlers (2022), VI, 118 pp
ISBN: 978-3-95806-612-0

Band / Volume 253
Topological magnonic properties of two-dimensional magnetic materials
L. Zhang (2022), xx, 154 pp
ISBN: 978-3-95806-621-2

Band / Volume 254
Role of secondary metabolites in antiphage defense in *Streptomyces*
Aël Hardy (2022), IV, 193 pp
ISBN: 978-3-95806-633-5

Band / Volume 255
Neutron Scattering
Lectures of the JCNS Laboratory Course held at Forschungszentrum Jülich and at the Heinz-Maier-Leibnitz Zentrum Garching
edited by T. Brückel, S. Förster, M. Kruteva, M. Zobel, and R. Zorn (2022), ca. 300 pp
ISBN: 978-3-95806-634-2

Band / Volume 256
Magnetoelectric Interactions in Multiferroic Thin-film Heterosystems and Nanostructures
H. Gökdemir (2022), x, 140 pp
ISBN: 978-3-95806-635-9

Weitere ***Schriften des Verlags im Forschungszentrum Jülich*** unter
http://wwwzb1.fz-juelich.de/verlagextern1/index.asp

Schlüsseltechnologien / Key Technologies
Band / Volume 256
ISBN 978-3-95806-635-9

Mitglied der Helmholtz-Gemeinschaft

JÜLICH
Forschungszentrum